

T-4618

**MODELING FIBER FORMATION BY
THE SPINNING PROCESS**

by

Yifang Cai

ProQuest Number: 10796625

All rights reserved

INFORMATION TO ALL USERS

The quality of this reproduction is dependent upon the quality of the copy submitted.

In the unlikely event that the author did not send a complete manuscript and there are missing pages, these will be noted. Also, if material had to be removed, a note will indicate the deletion.



ProQuest 10796625

Published by ProQuest LLC (2019). Copyright of the Dissertation is held by the Author.

All rights reserved.

This work is protected against unauthorized copying under Title 17, United States Code
Microform Edition © ProQuest LLC.

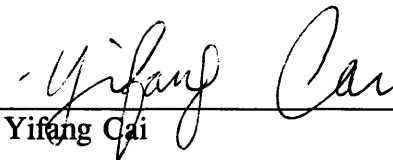
ProQuest LLC.
789 East Eisenhower Parkway
P.O. Box 1346
Ann Arbor, MI 48106 – 1346

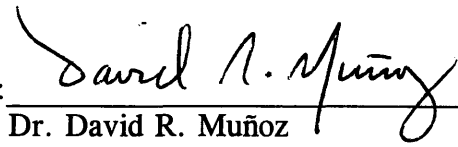
T-4618

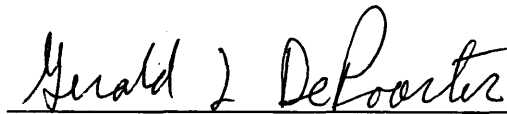
A thesis submitted to the Faculty and Board of Trustees of the Colorado School of Mines in partial fulfillment of the requirements for the degree of Doctor of Philosophy (Materials Science).

Golden, Colorado

Date 7/14/94

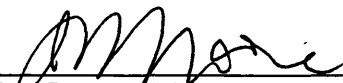
Signed: 
Yifang Cai

Approved: 
Dr. David R. Muñoz
Thesis Advisor


Dr. Gerald L. DePoorter
Thesis Co-advisor

Golden, Colorado

Date 7/12/94


Dr. John J. Moore
Director
Materials Science Program

ABSTRACT

An experimental device has been designed and built for simulating the refractory fiber spinning process. Refractory fibers are used to thermally insulate the walls of high temperature (1500 °C) industrial furnaces. The fiber spinning process is currently the least expensive method of manufacturing these fibers. Glycerine was selected as a substitute liquid for experimentally modeling the process based on liquid spinnability (the ratio of the fluid dynamic viscosity to its surface tension) and dynamic similarity analysis. Liquid threads formed by the Rayleigh-Taylor instability were observed with the aid of a stroboscope and large format camera and a high-speed video system. Theoretical analysis has been performed for three stages of fiber formation. Numerical modeling for this process has also been attempted using the finite element analysis computer code FIDAP, but results were limited by the code capability.

It was found that thread parameters (including thread diameter, length and instability wavelength) are a function of the product of the Reynolds and Weber numbers. Therefore, relationships between the liquid thread parameters and the controllable parameters and liquid transport properties (including disk diameter and rotation speed, liquid viscosity and surface tension) have been quantitatively established. This information should be useful to designers of new fibrous materials and industrial process control engineers involved with the spinning process.

TABLE OF CONTENTS

	<u>Page</u>
ABSTRACT	iii
LIST OF FIGURES	vii
LIST OF TABLES	x
ACKNOWLEDGMENTS	xi
PRINCIPAL NOTATION	xii
SUBSCRIPT	xiv
CHAPTER 1 INTRODUCTION	1
CHAPTER 2 BACKGROUND	4
2.1 Description of Fiber Formation Process	4
2.2 Literature Survey	5
2.2.1 Fiberization models	5
2.2.2 Rayleigh-Taylor Instability	8
2.2.3 Free Surface Flow	10
2.3 Three Stages of Fiber Formation	12
CHAPTER 3 EXPERIMENTAL SET UP	15
3.1 Dynamic Similarity Analysis	15
3.2 Spinning Machine Design	25

3.3 Recording Devices	28
3.3.1 Stroboscope-Camera System	28
3.3.2 35 mm Camera and Quartz-Halogen Light System	28
3.3.3 Motion Analyzer	29
3.4 Experimental Procedures	30
CHAPTER 4 RESULTS AND DISCUSSION	32
4.1 Observed Phenomena from the Experimental Models	32
4.2 The Effects of the Controllable Parameters on Thread Parameters	38
4.2.1 The Effect of Disk Rotation Speed on Thread Parameters	38
4.2.2 The Effect of liquid Viscosity on Thread Parameters	43
4.2.3 The Effect of Disk Diameter on Thread Parameters	46
4.3 Measurement and Calculation of Thread Parameters	49
4.3.1 Measurement of Thread Diameter, Length and Instability Wavelength	50
4.3.2 Uncertainty Analysis on Measurements	53
4.3.3 Calculation of the Thread Growth Velocity	59
4.4 Quantitative Relationships between the Thread and the Controllable Parameters	65
4.5 Physical Meaning of Mathematical Models	75
4.6 Estimation of the Effective Mass Flow Rate	78

CHAPTER 5 THEORETICAL ANALYSIS AND COMPUTER MODELING	82
5.1 Governing Equations of Three Stages of Fiber Formation	82
5.1.1 Governing Equations for the Perturbation forming due to Rayleigh Taylor Instability	82
5.1.2 Governing Equations for the Free Surface Flow	87
5.1.3 Break-up Mechanism of a Fiber by Air Drag	91
5.2 Numerical Modeling by the Finite Element Methods	92
5.2.1 Numerical Model Set up	93
5.2.2 Numerical Modeling Results	97
5.2.3 Reasons for Unexpected Results	109
CHAPTER 6 CONCLUSIONS AND SUGGESTIONS FOR FURTHER WORK	112
6.1 Conclusions	112
6.2 Suggestions for Further Work	113
REFERENCES CITED	115
APPENDIX A CALIBRATED RELATIONSHIPS USED IN THE EXPERIMENTS	119
APPENDIX B SAMPLE INPUT FILE FOR THE RT INSTABILITY MODEL	122
APPENDIX C SAMPLE INPUT FILE FOR THE FREE SURFACE FLOW MODEL	127

LIST OF FIGURES

<u>Figure</u>	<u>Page</u>
2.1 Manufacturing process of fiber blankets (Westerlund and Hoikka, 1989) . . .	4
2.2 Three stages of fiber formation process	12
2.3 Definition of Rayleigh-Taylor instability (Kull, 1991)	13
3.1 Viscosity versus wt% of Al ₂ O ₃ for the aluminosilicate system at T=2003 °C	17
3.2 Viscosity versus temperature for the Al ₂ O ₃ (63 wt%) and SiO ₂ system . . .	18
3.3 Viscosity versus wt% of glycerine at T=25 °C (Vargaftik, 1983)	22
3.4 Viscosity versus temperature for the 95 wt% of glycerine and 5 wt% water system (Vargaftik, 1983)	23
3.5 Sketch of experimental device for simulating the spinning process	26
4.1 Photograph taken using 35 mm camera with quartz halogen lights at n=260 rpm, D=0.381 m, T=25 °C, Q=0.2 GPM, and M=0.15	33
4.2 Photograph taken using large format camera and laser light system at n=260 rpm, D=0.381 m, T=25 °C, Q=0.2 GPM, and M=1.5	34
4.3 Photographs taken by large format camera and stroboscope system (a) n=90 rpm, D=0.381 m, T=41 °C, M=2.2, ΔH=6 mm. (b) n=400 rpm, D=0.381 m, T=25 °C, M=4.39, ΔH=4.4 mm	37
4.4 Photographs taken using the large format camera and stroboscope system for different rotation speeds n at D=0.381 m, T=25 °C, M=4.39: ΔH=4.3 mm, (a) n=260 rpm, (b) n=400 rpm	39
ΔH=6.7 mm, (c) n=670 rpm, (d) n=920 rpm	40
ΔH=6.7 mm, (e) n=1200 rpm, (f) n=1560 rpm	41

4.5 Photographs taken using the large format camera and laser system for different rotation speeds n at $D=0.381$ m, $T=25$ °C, $Q=0.2$ GPM, and $M=1.76$:
 (a) $n=90$ rpm, (b) $n=260$ rpm 42

4.6 Photographs taken using the camera-stroboscope system for varied viscosities at $n=260$ rpm, $D=0.381$ m, $M=1.9$, $\Delta H=6$ mm:
 (a) $\mu=0.336$ N-s/m², $T=20$ °C, (b) $\mu=0.24$ N-s/m², $T=30$ °C 44
 (c) $\mu=0.108$ N-s/m², $T=40$ °C, (d) $\mu=0.051$ N-s/m², $T=50$ °C 45

4.7 Photographs taken using the large format camera and stroboscope system for different disk diameter at $n=260$ rpm, $T=25$ °C, $M=4.39$,
 (a) $D=0.381$ m, $\Delta H=4.3$ mm, (b) $D=0.457$ m, $\Delta H=6.7$ mm. 47

4.8 Photographs taken using the large format camera and stroboscope system for different disk diameter at $n=670$ rpm, $T=25$ °C, $M=4.39$,
 (a) $D=0.381$ m, $\Delta H=4.3$ mm, (b) $D=0.457$ m, $\Delta H=6.7$ mm. 48

4.9 Thread growth length versus time (data obtained by the recording tape using the motion analyzer) 61

4.10a Thread growth velocity versus time (data obtained by the recording tape using the Motion Analyzer) 62

4.10b Thread growth velocity versus relative disk tangent velocity 64

4.11 Dimensionless thread diameter versus Reynolds number only 66

4.12 Dimensionless thread diameter versus Weber number only 67

4.13 Dimensionless thread diameter versus ratio of Weber number to Reynolds number 68

4.14 Dimensionless thread diameter versus the product of Reynolds and Weber numbers 69

4.15 Dimensionless thread length versus the product of Reynolds and Weber numbers 71

4.16 Dimensionless instability wavelength versus the product of Reynolds and Weber numbers 72

4.17 Relationship between thread diameter and instability wavelength	77
4.18 Fraction of effective fiber flow rate to the incident flow rate versus disk rotation speeds	81
5.1 Temperature distribution along fiber length (Westerlund and Hoikka, 1989)	90
5.2 Geometry of the RT instability Model	95
5.3 Geometry of the free surface flow model	96
5.4 Geometry mesh of the RT instability Model	98
5.5 Free surface profile of the instability model at running time equaled 5.6×10^{-4} seconds	99
5.6 Mesh histories of the RT instability Model	
(a) Mesh at time = 4.5×10^{-4} seconds	100
(b) Mesh at time = 5.35×10^{-4} seconds	101
(c) Mesh at time = 5.65×10^{-4} seconds	102
5.7 Geometry mesh of the free surface Model	104
5.8 Free surface profile of the free surface model at running time equaled 1.15×10^{-3} seconds	105
5.9 Mesh histories of the free surface Model	
(a) Mesh at time = 9.0×10^{-4} seconds	106
(b) Mesh at time = 1.05×10^{-3} seconds	107
(c) Mesh at time = 1.11×10^{-3} seconds	108
A1 Disk rotation speed versus voltage	120
A2 Glycerine flow rate versus voltage	121

LIST OF TABLES

<u>Table</u>	<u>Page</u>
3.1 Spinnability of Aluminosilicate Materials	19
3.2 Spinnability of Candidates Liquids	20
3.3 Model Disk Diameter for Glycerine Liquid Based on Dynamic Similarity Analysis	25
4.1 Thread Diameter for 95% Glycerine and 5 wt% Water System	51
4.2 Thread Length for 95% Glycerine and 5 wt% Water System	52
4.3 Instability Wavelength for 95% Glycerine and 5 wt% Water System	53
4.4 Input Data of Dependent Variables at Three Points for Uncertainty Analysis	57
4.5 Uncertainties of the Experimentally Determined Functions for Three Points	58
4.6 Calculation of Thread Growth rates	60
4.7 Disk Rotation Speed Comparison for Different Composition Fibers with Same Fiber Diameter and $Re \cdot We$ Value	75
4.8 Calculation of Fraction of Effective Flow Rate to the Incident Flow Rate	80
5.1 Calculation of Instability Growth Rates	86

ACKNOWLEDGMENTS

The author wishes to express her appreciation to the following:

Dr. David R. Muñoz for his constant availability, careful guidance, and unending encouragement during this research.

Dr. Gerald L. DePoorter for his efforts in providing academic guidance and financial support during this research.

Dr. Chester Van Tyne for serving as a chairman of the thesis committee.

The committee members Drs. Graham G. W. Mustoe and Phillip C. Martin for their academic guidance and considerate help on this work.

Dr. David Reuss of General Motors Research Laboratory for loaning the large format camera used to obtain the high resolution photographs.

Mr. John Jezek for his help in building the experimental apparatus.

Ms. Josephine Curtis for her suggestions while serving on the research team.

Mr. Weiguang Zhang for his help on experimental testing.

The United States Department of Energy for funding this research under Cooperative Agreement Number DE-FC07-89ID12880.

PRINCIPAL NOTATIONS

a	--	acceleration
A, B	--	constants
C	--	specific heat of materials, air drag coefficient
d	--	diameter of threads or fibers
D	--	disk diameter, air drag per unit length
E	--	energy
h	--	air natural convection heat transfer coefficient
K	--	wave number
L	--	length of threads or fibers
M	--	magnification
n	--	rotation speed of disk
P	--	pressure
Q	--	flow rate of liquid melts
R	--	disk radius, gas constant
t	--	disk wall thickness
U, V	--	velocity component in x and y direction
W	--	uncertainty
x,y	--	cartesian coordinates
Z	--	number of fibers

Γ	--	surface domain
δ	--	growth rate of RT instability
Λ	--	thermal conductivity
λ	--	wavelength of RT instability
ϵ	--	surface emissivity
η	--	displacements of free surface
θ	--	experimentally determined function
μ	--	dynamic viscosity
ν	--	kinematic viscosity
ρ	--	bulk density
σ_0	--	Stefan-Boltzmann constant
σ	--	surface tension between liquid and air
τ	--	time
ϕ	--	dependable variables
ω	--	angular velocity
ζ	--	stress

SUBSCRIPTS

1	--	dense fluid
2	--	less dense fluid
f	--	fiber
m	--	liquid model, measured variables
a	--	air
I	--	input
p	--	constant pressure
r	--	realistic variables
v	--	constant volume
o	--	initial state, output
T	--	total

CHAPTER 1

INTRODUCTION

Commercial refractory insulating fibers with high viscosity are cost effectively produced by a spinning fiberization process. Fiberization occurs when a ceramic melt is poured onto rapidly rotating disks.

Although previous work on this process began as early as the 1940s, there is not a theoretically sound basis for this unit operation (Westerlund and Hoikka, 1989). The reason for this is that measuring and observing of the fibers during the formation is very difficult in the high operating temperatures (1500-2000 °C) and harsh manufacturing conditions. Other difficulties relate to small fiber size (1-10 μm in diameter) and rapidly occurring phenomena. Up to now, studies in this field have been of general technological nature (Subochev and Pitak, 1989), but the way in which a single fiber forms is not entirely understood. Careful experiments have been needed to provide a better understanding of the mechanism of fiber formation, thereby resulting in improved process control. Therefore, an experimental device was built and a mathematical model for the fiberization process was developed.

The purpose of this work was to study the phenomena occurring in the fiber spinning process in order to understand the mechanisms of glassy fiber formation, growth and break-up. Furthermore, a mathematical model was developed to establish

the relationships between the fiber parameters which include fiber diameter (d), fiber length (L) and instability wavelength (λ) and the controllable parameters which include disk rotation speed (n) and diameter (D), dynamic viscosity (μ) and flow rate (Q) of the liquid melts, and the surface tension (σ) between liquid and air. Also, the possibility of making low viscosity fibers using the melt spinning method was assessed based on the mathematical and experimental models. Low viscosity fibers, which have not been melt spun, such as mullite ($3\text{Al}_2\text{O}_3 \cdot 2\text{SiO}_2$), exhibit low shrinkage at high operating temperatures. Other high performance fibers currently available on the market are usually manufactured as polycrystalline materials using a sol gel process which is significantly more expensive than the melt spinning process (Olds, 1992).

Both experimental and theoretical work has been performed in order to achieve the above objectives. In the experimental work, results were obtained which illustrate in detail the fiber formation process. In the theoretical part of this thesis, governing equations were derived for this process. Numerical analyses using the computer code FIDAP were attempted. The usefulness of the results was limited by the code capability.

In Chapter 2 of this thesis, the background necessary for a good understanding of this research work is presented, including a review of previous work on the spinning process. First, the spinning process is described. Next, a review of previous theoretical and experimental work performed to study melt spinning process,

Rayleigh-Taylor instability and free surface flow is given. Finally, the Rayleigh-Taylor instability theory is introduced, and the three stages of fiber formation are discussed.

In Chapter 3, the experimental device for observing the instability and fiber development at ambient temperatures is described. The device consists of an experimental spinning machine for simulating the fiber formation process, a large format camera and a stroboscope for recording fiber generation and formation, and a high speed video camera for analyzing the speed of fiber growth.

In Chapter 4, the results obtained by experimental simulation are presented and discussed. First, the observed phenomena are presented. Next, the relationships found between the fiber parameters and the controllable parameters are discussed, both qualitatively and quantitatively. Finally, an estimate of controllable parameters for making low viscosity fibers are predicted.

In Chapter 5, the theoretical analysis and numerical modeling are presented. Governing equations for fiber formation are introduced. The growth rate of Rayleigh-Taylor instability is calculated according to linear stability theory. Numerical modeling for fiber generation and growth by computer code FIDAP is demonstrated.

In Chapter 6, conclusions for the present work are summarized, and recommendations for the further studies on this subject are provided.

CHAPTER 2

BACKGROUND

2.1 Description of Fiber Formation Process

The spinning process is shown in Figure 2.1. A refractory melt stream exits from a nozzle and falls onto rotating disks. Melt threads are thrown into a wool chamber from the disks as they solidify into fibers. Then, fibers are transported away from the spinning machine by blow-in air, and collected on a screen conveyor. Finally, the fiber mass is formed into mats (blankets) by a needling machine.

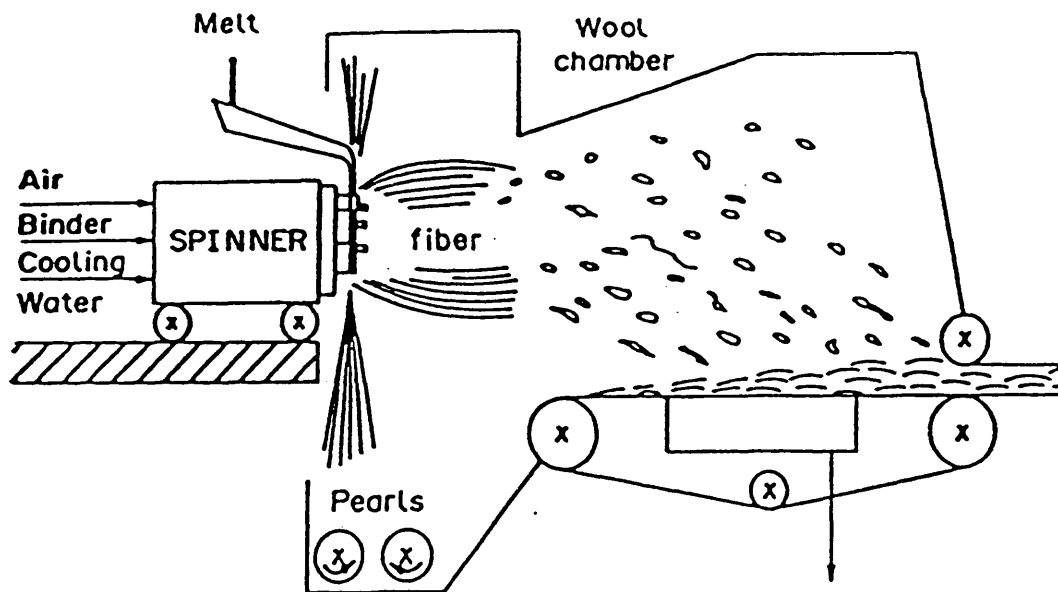


Figure 2.1. Manufacturing process of fiber blankets (Westerlund and Hoikka, 1989)

2.2 Literature Survey

In this section, a review of previous work on the spinning process is presented. Since this process is very closely related to the Rayleigh-Taylor instability and free surface flow, work performed for these two subjects is also examined.

2.2.1 Fiberizing Process Models

There are few published results of insulating fiber formation models by spinning processes. Westerlund and Hoikka (1989) first introduced a model for the investigation of the breaking mechanism in the formation of mineral fibers with a spinning machine under steady-state conditions, and a model for the study of the transient fiber cooling process based on an energy balance. They also calculated the temperature, position and internal tension of a single fiber during the formation process according to the effects of the inertial and aerodynamic forces. They assumed the length, diameter and growth rate of fibers were constant when the calculations were implemented. Eisenklam (1964) analyzed ligament formation from spinning disks and cups and gave an expression for the growth rate factor of the Rayleigh-Taylor instability in the direction of centrifugal force at the interface of inviscid fluid and air. Expressions were presented and experimentally confirmed for the conditions of drop formation from spinning cups (Fraser et al., 1963). Photographs were shown for three mechanisms of drop formation from rotating cups: (a) direct drop formation at low flow rate, (b) break-down of threads at medium flow rate, (c) sheet

disintegration at high flow rate. The mechanism (b) is similar to the fiber spinning process, in which threads form long jets, and the jets are stretched and finally break down into strings of drops as they extend into the atmosphere. Unfortunately, they did not discuss this mechanism in detail. Mainly, they described the thin film formation process.

Hinze and Milborn (1950) derived a semi-empirical relationship between the number of ligaments and dimensionless groups for the state of ligament formation from stability considerations of a liquid torus that forms on the outer periphery of the spinning cup. The number of ligaments (Z) was given by

$$Z = 0.215 \left(\frac{\rho \omega^2 D^3}{\sigma} \right)^{\frac{5}{12}} \left(\frac{\rho \sigma D}{\mu^2} \right)^{\frac{1}{6}} = 0.215 \left(\frac{\rho^7 \omega^{10} D^{17}}{\sigma^3 \mu^4} \right)^{\frac{1}{12}} \quad (2.1)$$

which will be compared with the results obtained from this study in Chapter 4.

Eisenklam (1964) points out that this equation was verified experimentally for small disks ($D=25$ mm, but not as large as 100 mm) and liquids whose viscosity varied widely but whose surface tension and density were practically invariant with respect to temperature. Through experiments performed by Hinze and Milborn (1950), the number of ligaments was shown to be independent of the flow rate (Q). Hinze and Milborn further analyzed various stages of the development of a single ligament and predicted that the shape of the ligaments was roughly an involute.

Walz and Mayer (1966) studied the process of producing fibers from glass and rock melts in blast nozzles by means of high-speed cinematography. Motion pictures provided the detailed information on the fiber and bead formation. The formation of beads is a undesirable phenomenon in the fiberization process. These beads impair the quality of the fibers by increasing the bulk thermal conductivity and surface roughness of fibers. The motion pictures also revealed that beads are formed by various mechanisms. The coefficients of friction, the heat transmission coefficients and the cooling times of thin filaments were calculated by means of a boundary layer theory.

Ziabicki (1976) explained the nature and physical mechanisms accompanying a continuous polymer fiber formation process. These fibers are formed by the extrusion of the molten fluid through a spinneret (a rounded orifice in a melt container). He also provided critical conditions of fiber formation such as the spinnability number and goes into a general discussion of the hydrodynamic instability of fluids. The spinnability of a fluid depends on the ratio of viscosity and surface tension (μ/σ). The lower the ratio, μ/σ , the more probable the fiber will be broken into drops, and the shorter the critical fiber length will be. the critical fiber length is the maximum length for which liquid can be stretched by the spinning process. Typical values of the ratio for some materials using various spinning procedures are given in Ziabicki's book. For example, the ratio of μ and σ for inorganic glasses in the melt-spinning process is in the range of 0.1 to 1 s/m. No recommended values are available for the

refractory insulating materials.

Subochev et al. (1989) analyzed the refractory fiber formation process through disintegrated jets. They also concluded that the ratio of the viscosity of the melt and the surface tension was found to be an extremely important parameter in fiber formation process.

2.2.2 Rayleigh-Taylor Instability

The Rayleigh-Taylor instability appears to be the critical mechanism during the early stage of the fiberizing process. Therefore, it is important to review the application of Rayleigh-Taylor (RT) instability theory on a thin liquid layer.

Kull (1991) reviewed the theory of the RT instability and its application to various flow models such as viscous flow, incompressible flow and ideal fluid model with different boundaries such as planar, spherical and free surface boundaries.

Fermigier et al. (1992) reported experimental observations of the two-dimensional patterns in the RT instability of a thin layer of viscous fluid due to gravitational force, and derived the nonlinear equations for the evolution of patterns having different symmetries.

The nonlinear RT instability of a liquid layer on a horizontal plane below a second liquid of higher density was studied by Newhouse and Pozrikidis (1990). Under the assumption of creeping flow, the motion was studied as a function of surface tension and the ratio of the viscosities of the two fluids. The flow induced by

the deformation of the layer was represented by an interfacial distribution of Green's function. A Fredholm integral equation was solved by successive iteration using a computer program. The results showed that the flow perpendicular to the interfacial layer could be characterized by three stages of development. In a short time period, the initial disturbance grew at an exponential rate, and the layer retained a sinusoidal shape. In the second stage, a leading drop was formed on top of a narrow, short stem. In the final stage, the stem was elongated and thinned.

Two-dimensional hydrodynamic codes were used to simulate the growth of perturbations at an interface between two fluids of different density due to RT instability by Youngs (1984). Bellman and Pennington (1954) studied the effects of surface tension and viscosity on RT instability. Their numerical results showed that the surface tension and the viscosity opposed the RT instability but did not eliminate it, as long as the body force was large enough to overcome the associated resisting force.

The available experiments are adequate to confirm semi-quantitatively, or perhaps even quantitatively, several predictions of the linear analysis for the initial growth of the instability (Sharp, 1984). The experiments also provide pictures of the development of bubbles and spikes. Dalziel (1992) presents a qualitative view of the development of the instability using remarkable visualization techniques. Quantitative measurements are obtained through digital image analysis. But the available experiments are still inadequate for modeling the late stage of RT instability. More

and better experiments are still needed (Sharp, 1984) to allow a complete understanding of the RT instability.

2.2.3 Free Surface Flow

Sharp (1984) also pointed out that there is no detailed description about how RT spikes break up into droplets. He suggested that the heavy falling spike can be analogous to the free surface flow of a liquid jet. Since special studies on the theory of the fiber formation process are absent in the published literature, the well-known studies concerning the disintegration of jets, droplets, and liquid films have been adapted when investigating the mechanism of fiber formation.

Numerous patterns of drop sizes and velocities are observed to occur in the atomization regime of jet disintegration (Reitz and Bracco, 1982). Factors affecting the character of these patterns include surface tension, viscosity and the nature of "aerodynamic" forces.

In fact, the late stage of RT instability is similar to the free surface flow of liquid jet in the acceleration direction. Mekias and Vanden-Broeck (1989) studied a two-dimensional free-surface flow produced by a submerged source in a fluid of finite depth. The fluid was treated as inviscid and incompressible. It was assumed that there was a stagnation point on the free surface just above the source. The shape of the free surface and the flow velocities were determined numerically.

In general, solutions to free-surface flow problems are best found by numerical

techniques. Experience has shown that it is important to resolve the free surface with a high degree of precision. Boundary integral techniques are a natural choice since they are adaptive, in that information only at the free surface is used to predict its motion (Baker and Meiron, 1984). Axisymmetric and three-dimensional Rayleigh-Taylor instability problems have been solved by boundary integral methods. SOLA-VOF is a simple but powerful computer program using finite difference methods for the solution of two-dimensional transient fluid flow with free boundaries (Wilson and Nichols, 1980). It is based on the concept of a fractional volume of fluid and provides a wide range of applications. Its basic modes of operation are for single fluid calculations having multiple free surfaces and for calculations involving two fluids separated by a sharp interface. The FIDAP fluid dynamics analysis code (FDI, 1993) is a general purpose computer program that uses the finite element method to solve the conservation of momentum and energy equations and simulate many classes of fluid flows. It has the capability of simulating fluid flow problems which involve free or moving boundaries. In FIDAP, the basic approach to free surface problems involves a deforming spatial mesh where nodes located on a free boundary are allowed to move such that they remain on the free boundary. An additional degree of freedom is associated with the nodes on the free boundary which directly determines their location in space.

2.3. Three Stages of Fiber Formation

Summarizing the previous work on the fiberization process, the key features of this process can be broken into three stages as illustrated in Figure 2.2.

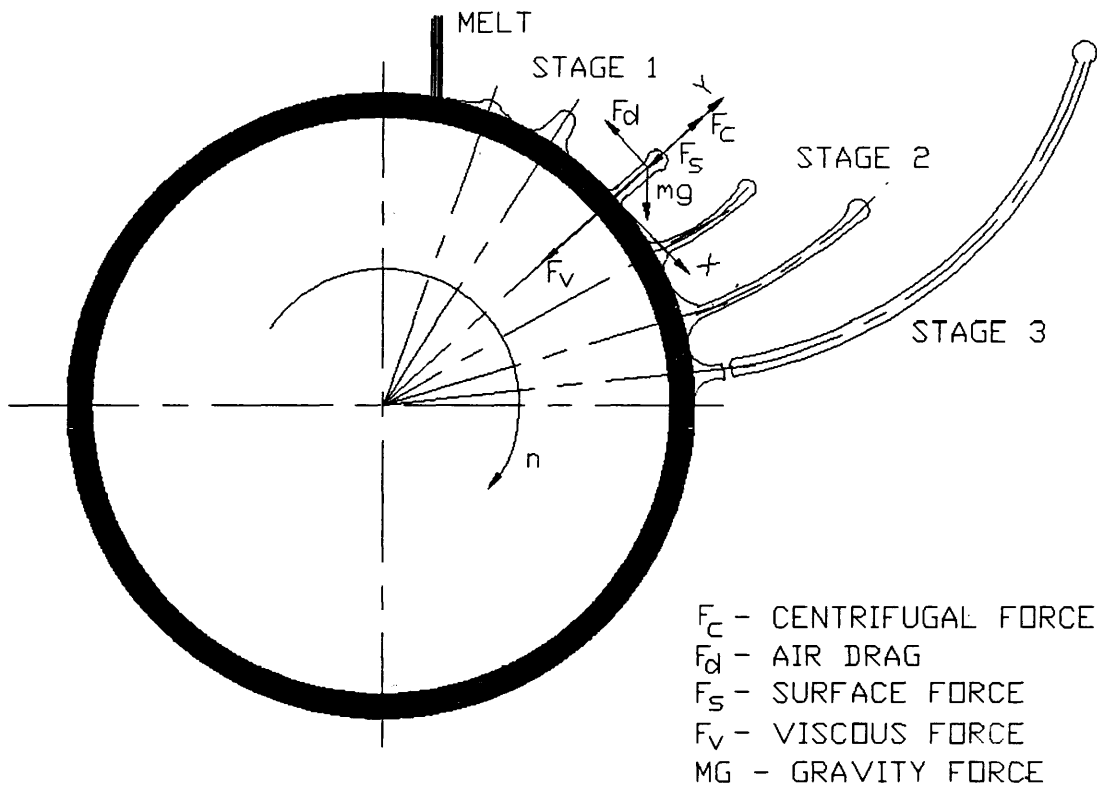


Figure 2.2 Three stages of fiber formation process.

the direction toward the denser fluid for a system with different densities ($\rho_2 > \rho_1$) as shown in Figure 2.3.

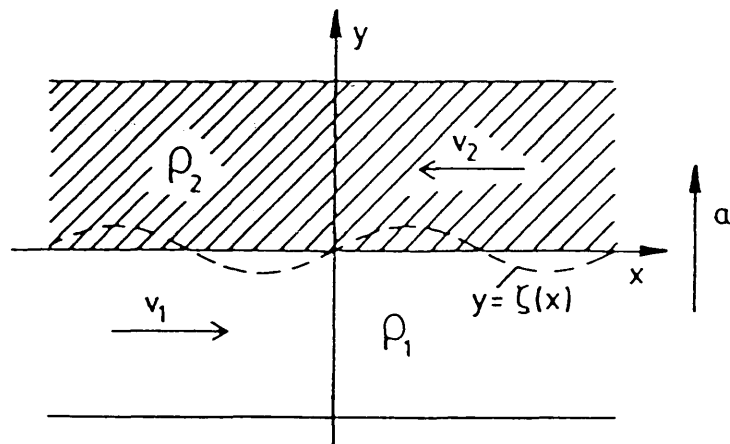


Figure 2.3. Definition of Rayleigh-Taylor instability (Kull, 1991).

For the fiberization spinning process, the molten refractory exits the melt furnace as a stream from an orifice and falls onto a rotating disk. A thin film of liquid forms on the surface of the disk. Since the density of the liquid is greater than that of the surrounding air and the centripetal acceleration is directed toward the dense fluid and disk axis of rotation, a Rayleigh-Taylor (RT) instability between the air and liquid should occur. The RT instability for this process is driven by the centrifugal

fluid and disk axis of rotation, a Rayleigh-Taylor (RT) instability between the air and liquid should occur. The RT instability for this process is driven by the centrifugal force in the radial direction of the disk. The liquid, having a higher density than the air, is driven from the disk surface and is replaced by air. Small wavelike perturbations form and grow on the disk surface due to this RT instability. The perturbation takes the form of a short cylinder and moves in the outward radial direction. Since there is a large interface between liquid and air, the surface tension force is the major resistance to the fiber growth at this stage.

Stage 2. Fiber is elongated due to the resulting free surface flow and rapidly cooled by convection and radiation heat transfer to the surroundings.

Under the continued action of the centrifugal force, the fiber increases in length and decreases in diameter in the rapid free surface flow. As the fiber grows, the temperature decreases rapidly because of the large surface area and effective heat transfer to the surroundings. Westerlund and Hoikka (1989) have modeled the temperature distribution along fiber length and showed a significant temperature gradient. Since the viscosity of melted refractory oxides is a strong function of temperature, the viscosity of the liquid increases rapidly.

Stage 3. Fiber is broken at its base

As the fiber grows, it eventually breaks free from the liquid on the disk because the tensile force, due to air drag and the centrifugal force acting on the fiber, exceeds the liquid viscous and surface tension forces at the fiber base.

CHAPTER 3

EXPERIMENT SET UP

Most previous experiments described in the literature were set up to observe the RT instability occurring due to the gravitational force. No experiments similar to the fiber spinning process have been developed for understanding the mechanism of RT instability due to the centrifugal force. Therefore, it was necessary to develop an experiment to study the RT instability of the fiber spinning process.

This chapter first presents a dynamic similarity analysis for the experimental design and describes the experimental device for simulating the fiber formation process. This apparatus includes a spinning machine, a stroboscope-camera system and a high speed video (motion analyzer).

3.1 Dynamic Similarity Analysis

In the production of the high temperature fiber spinning operation, the fiber formation process is too fast to be traced with all but the most expensive motion photographic techniques, the operating temperature is very high, and the fiber thread is too small to be readily observed. In order to observe and quantify the fiber formation process, it is necessary to select a proper substitute liquid to simulate the refractory fiber liquid melts. As previously discussed, the spinnability of liquids,

which is defined as the ratio of the liquid dynamic viscosity and surface tension, has previously been found to be an important criteria for predicting the maximum length to which a liquid filament can be stretched in the spinning process. Therefore, the liquid chosen for further simulation experiments should have the same spinnability as that of the liquid refractory melts.

To determine the spinnability of liquid refractory melts at different compositions, the properties of refractory materials based on Al_2O_3 and SiO_2 (data given by Bansal and Doremus, 1986) were studied. The density and surface tension of molten material (from which refractory fibers are derived) are not strong functions of temperature, but are strong functions of composition. However, the viscosity is a very strong function of both material composition and temperature. The relationship between viscosity and weight percent alumina in aluminosilicate materials at 2003 °C is plotted in Figure 3.1 in semi-natural logarithmic form. Liquid viscosity decreases as the alumina content increases. Figure 3.2 shows the melt viscosity as a function of the melt temperature for a given composition. The liquid viscosity decreases as the temperature increases. Dashed curves in these two figures represent the least squares curve fit function of the given data (same meaning holds for Figures 3.3 and 3.4).

A typical spinnability for a refractory melt fiberized by the spinning process is $\mu/\sigma = 15/300 = 0.05$ poises-cm/dyne = 5 s/m (Olds, 1992). The spinnabilities of refractory materials with different compositions at the liquidus temperature of each composition are listed in Table 3.1.

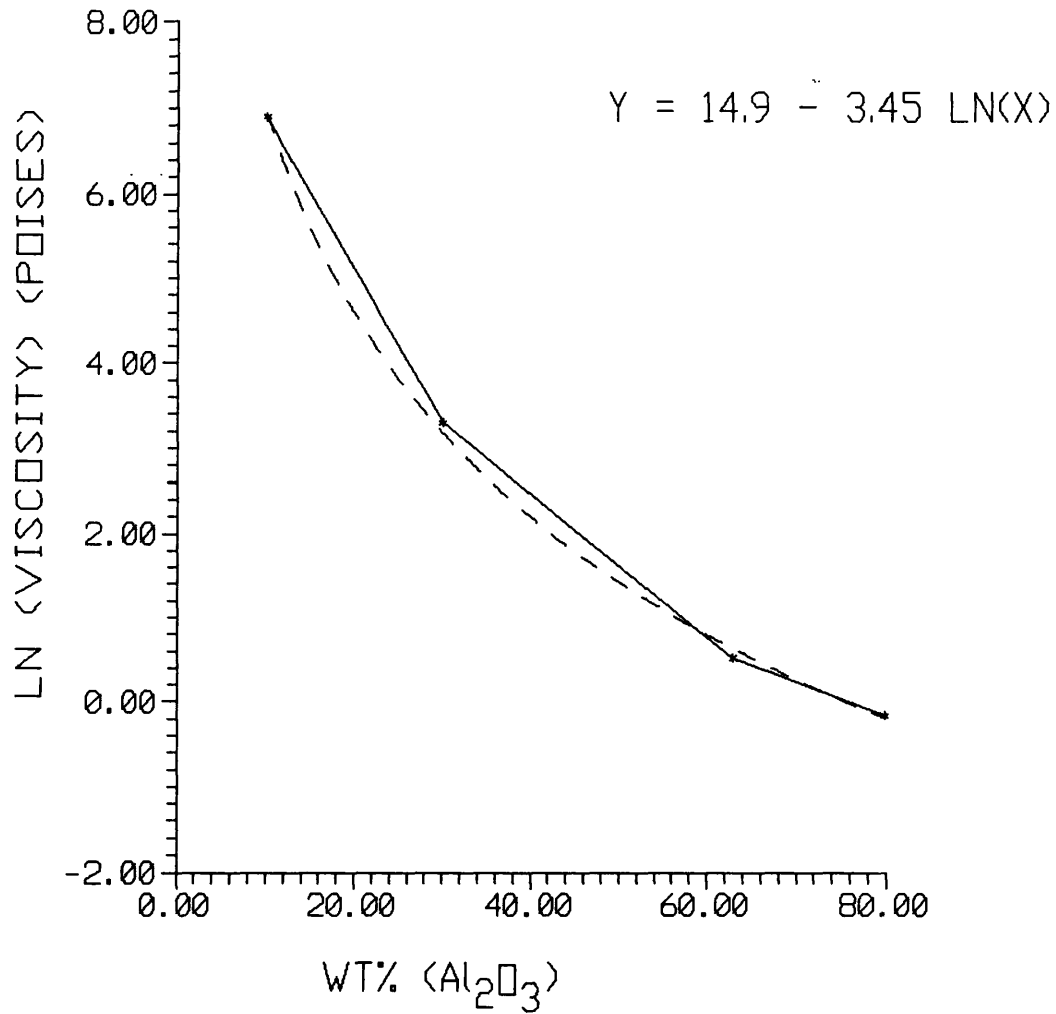


Figure 3.1. Viscosity versus wt% of Al₂O₃, for the aluminosilicate system at T=2003 °C.

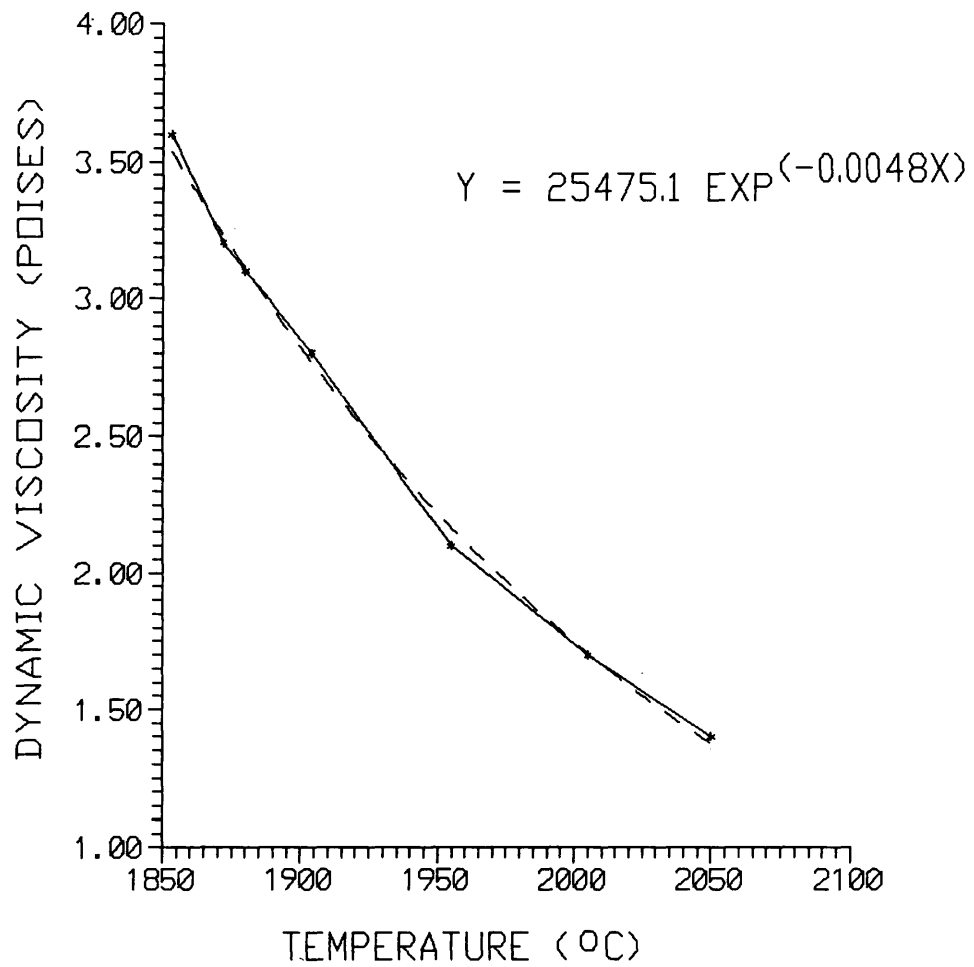


Figure 3.2. Viscosity versus temperature for the Al₂O₃ (63 wt%) and SiO₂ system.

Table 3.1 Spinnability of Aluminosilicate Materials

Al ₂ O ₃ (wt%)	SiO ₂ (wt%)	Viscosity μ (N-s/m ²)	Surface tension σ (N/m)	Spinnability μ/σ (s/m)
10.1	89.9	539.9	0.405	1333
30.1	69.9	8.4	0.406	20.7
48.0	52.0	2.37	0.411	5.771
62.9	37.1	0.36	0.414	0.87
71.8	28.2	0.18	0.415	0.43
79.8	20.2	0.15	0.442	0.34

The spinnability value of 5.8 s/m for aluminosilicate materials (Al₂O₃, 48 wt%, SiO₂ 52 wt%) is close to the typical value. This is a typical composition for fibers formed by spinning process (Olds, 1992). To match this value, several substitute liquids were considered for the experiment. Table 3.2 lists the dynamic viscosity, surface tension and spinnability of the candidate liquids.

Table 3.2 Spinnability of the Candidate Liquids

Liquid	T °C	μ N-s/m ²	σ N/m	μ/σ s/m
Carnauba wax	95.0	0.029	0.032	0.906
SAE 30 oil	15.6	0.38	0.036	10.6
Ethyl alcohol	20.0	0.001	0.023	0.043
Glycerine	20.0	1.41	0.064	22.03
	25.0	0.95	0.063	15.08
	30.0	0.63	0.063	10
	40.0	0.28	0.062	4.6
	60.0	0.08	0.061	1.3
	80.0	0.03	0.059	0.51
machine oil (heavy)	20.0	0.45	0.037	12.2
	40.0	0.11	0.037	2.97
	60.0	0.04	0.035	1.14
	80.0	0.02	0.034	0.588

Among the candidate liquids considered, the ratio (4.6 s/m) of the viscosity to the surface tension of glycerine at 40 °C is close to that (5.8 s/m) of refractory fiber melts. Therefore, the glycerine was further investigated as the substitute liquid for the experiment.

The liquid properties of glycerine are similar to those of the refractory fiber melts according to previously published data (Liley et al., 1988). The density and surface tension of glycerine remains nearly constant with changes in temperature (Weast, 1976). The viscosity of glycerine is a function of both composition and temperature. The relationship between viscosity and composition of glycerine-water mixtures at 25 °C is plotted in Figure 3.3 in natural logarithmic form. The liquid viscosity increases as the concentration of glycerine in an aqueous solution increases, which means glycerine properties are similar in the aqueous system to those of silica in the aluminosilicate system. Figure 3.4 shows the liquid viscosity as a function of liquid temperature for given compositions of the glycerine-water system. This figure is similar to Figure 3.2. The liquid viscosity decreases as temperature increases.

A dynamic similarity analysis was performed to determine the design criteria for the experiment. The dimensional analysis based on the Buckingham Pi theorem (Kundu, 1990) using the variables involved in the melt spinning process showed that this process was related to the Reynolds and Weber numbers. Therefore, the selection of design parameters for the experimental model was based on the above dimensionless numbers.

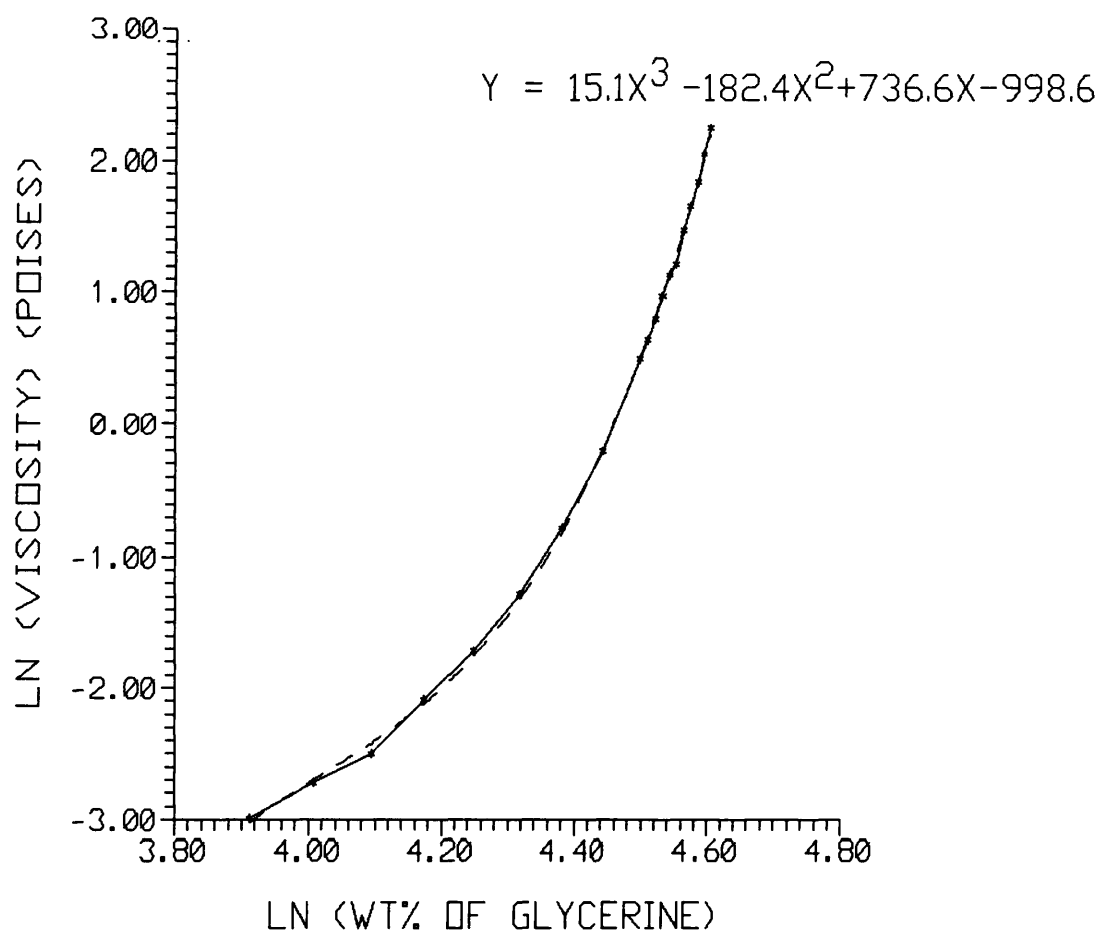


Figure 3.3. Viscosity versus wt% of glycerine at T=25 °C (Vargaftik, 1983).

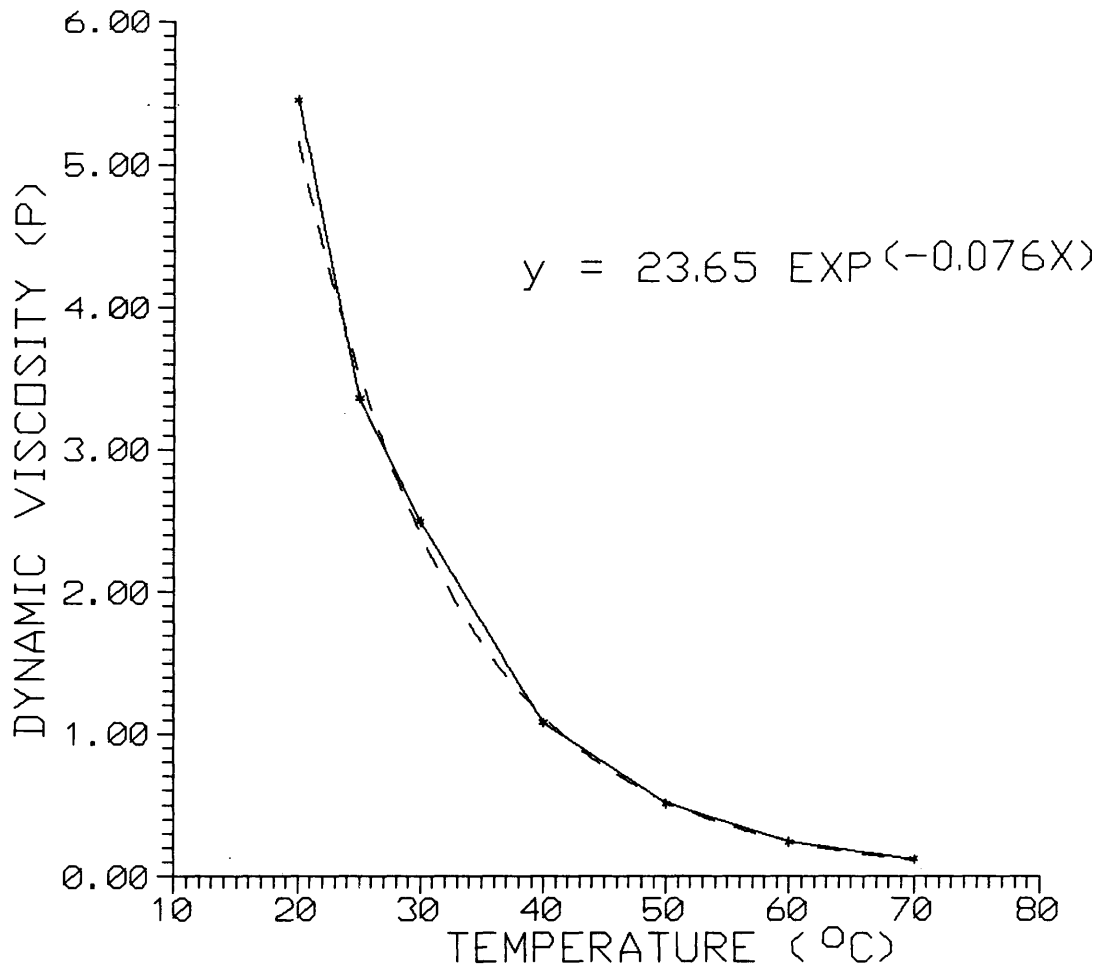


Figure 3.4. Viscosity versus temperature for the 95 wt% glycerine and 5 wt% water system (Vargaftik, 1983).

The experimental model disk diameter at different rotation speeds are calculated for glycerine-water solutions at different temperatures by matching the Reynolds and Weber numbers with those of the industrial high temperature refractory fiberization process. The model disk diameter, based on matching the Reynolds number, is

$$D_m = D_f \sqrt{\frac{\omega_f \rho_f \mu_m}{\omega_m \rho_m \mu_f}} \quad (3.1)$$

Based on matching the Weber number, the model disk diameter is

$$D_m = D_f \cdot \sqrt[3]{\left(\frac{\omega_f}{\omega_m}\right)^2 \left(\frac{\rho_f \sigma_m}{\rho_m \sigma_f}\right)} \quad (3.2)$$

The model disk diameters (D_m) are calculated from the above formula and physical parameters for spinning conditions of refractory fibers ($\text{Al}_2\text{O}_3\text{-SiO}_2$ system) actually produced at the Schuller Corporation. These physical parameters in the industrial process are $\rho_f=2900 \text{ kg/m}^3$, $\mu_f=2.37 \text{ N-s/m}^2$, $\sigma_f=0.416 \text{ N/m}$, $n_f=12700 \text{ rpm}$, $D_f=0.203 \text{ m}$, and the spinnability $\mu/\sigma=5.7 \text{ s/m}$. Table 3.3 lists the calculated model disk diameters at different disk rotation speeds and glycerine temperatures

Corresponding to the above actual fiberization parameters, the maximum diameter for each given temperature was 0.418 m - 0.536 m at $n_m = 2500 \text{ rpm}$ from Table 3.3. Therefore, the maximum diameter and maximum rotation speed of model disk were selected as $D_m=0.5 \text{ m}$ and $n_m=2500 \text{ rpm}$, respectively. These were used to find the model characteristics through the dynamic similarity analysis.

**Table 3.3 Model Disk Diameter for Glycerine Liquid
Based on Dynamic Similarity Analysis**

T (°C)	Model disk diameter (m)					
	$n_m = 1000$ rpm		$n_m = 1560$ rpm		$n_m = 2500$ rpm	
	$Re_m = Re_f$	$We_m = We_f$	$Re_m = Re_f$	$We_m = We_f$	$Re_m = Re_f$	$We_m = We_f$
20	0.761	0.665	0.678	0.580	0.536	0.423
25	0.618	0.663	0.558	0.578	0.440	0.422
30	0.502	0.662	0.453	0.577	0.358	0.421
40	0.339	0.662	0.306	0.577	0.241	0.422
60	0.182	0.659	0.164	0.575	0.130	0.420
80	0.115	0.656	0.103	0.472	0.082	0.418

3.2 Spinning Machine Design

The experimental device, shown in Figure 3.5, was designed and constructed based on the critical parameters determined by similarity analysis. A disk (6) is driven by a D. C. motor (4) with 3/4 horse power so that the speed of disk can be adjusted continuously from 0 to 2500 revolutions per minute (rpm).

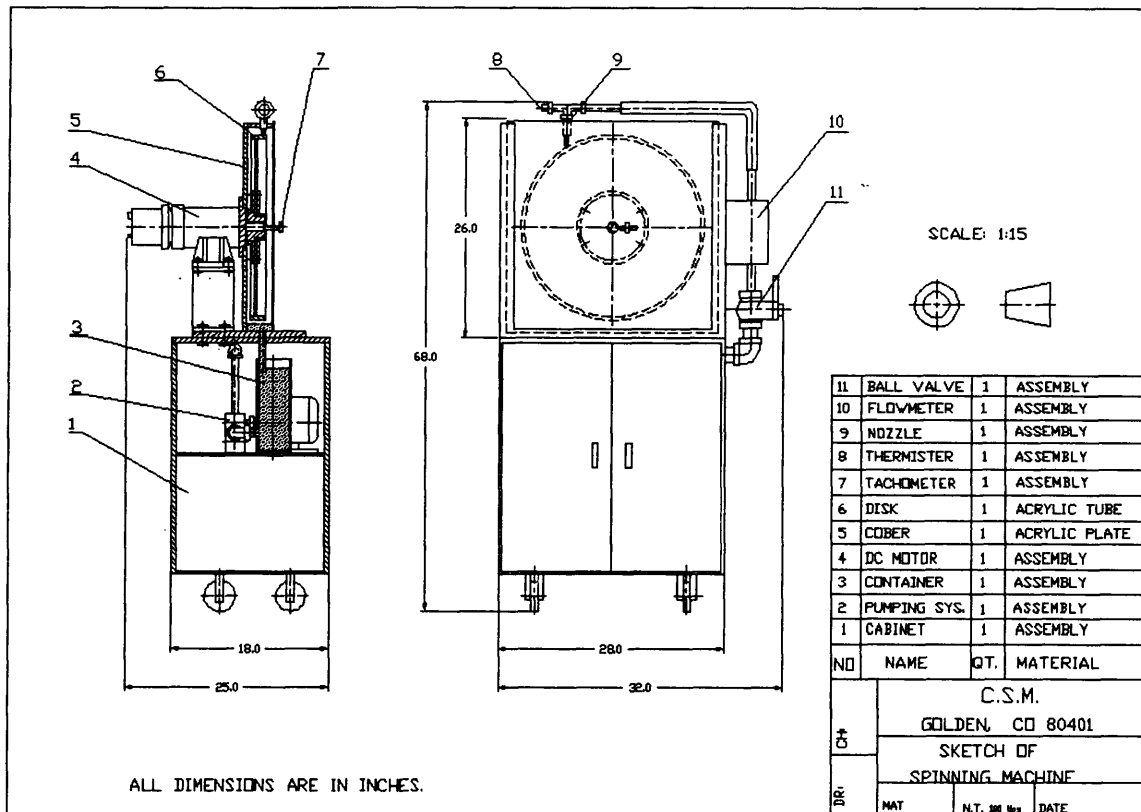


Figure 3.5. Sketch of experimental device for simulating the spinning process.

The rotation speed of the disk is measured by tachometer (7), and output in a unit of DC voltage. In the tachometer, a square wave generated by the interaction between a magnetic pickup and a steel 30 toothed gear is transformed into DC voltage. The calibrated relationship between the disk rotation speed and the DC output voltage of the tachometer is linear as shown in Figure A1 in Appendix A.

Three different disks were fabricated for testing. The disks are made of acrylic tube with wall thickness $t=6.83$ mm and diameters 0.254 m, 0.381 m, and 0.457 m. The outer surface of the biggest disk ($D=0.457$ m) was machined for disk concentricity. The wall thickness for this disk is 5.96 mm. The outer circumference of each disk is covered with an adhesive backed, rough grit sandpaper (sold at skateboard shops). The sandpaper provides a roughened surface allowing better wetting between the liquid and the disk.

Glycerine flows onto the disk circumference through a spray nozzle (9). The liquid is delivered to the nozzle through a pumping system (2) which includes an AC motor, a positive displacement gear pump, and tubing. The liquid, after contacting the spinning disk, returns to a container (3) which is temperature controlled. The temperature of the liquid is measured and controlled by a thermistor (8) and a relay control system. The flow rate of liquid is measured by flowmeter (10) and adjusted manually by a ball valve (11). The liquid flow rate is output as a DC voltage. The calibrated relationship between the liquid flow rate and the DC output voltage of the flowmeter is linear as shown in Figure A2 in Appendix A. A cover (5), made of acrylic plate, is provided to contain the liquid spray and to prevent the liquid threads spraying on other devices such as camera.

3.3 Recording Devices

Three recording devices were used for recording thread images generated by the spinning machine. They are a stroboscope-camera system, a 35 mm camera with a quartz-halogen light system and a high speed video system (motion analyzer)

3.3.1 Stroboscope-Camera System

A TOYO-VIEW 45C (102x127 mm) large format camera was used to record the fiberization process. The lens installed on this camera was a Nikkor-AM ED with the focal length of 210 mm and the maximum aperture of f/5.6. The magnification of the camera can be changed from 2 to 5 by adjusting bellows. Two light sources were used. One is a Pioneer DT-311 digital stroboscope with flashing range 100-30,000 flashes per minute (FPM). The other was a 4mW Argon-Ion laser light. The diameters and lengths of the threads of liquids and the wavelength of the instability were recorded in photographs which were later measured with the graduated scale of an optical magnifier (7X).

3.3.2 35 mm Camera and Quartz-Halogen Light System

This system was used to record the fiber motion relative to the inertial reference frame. It consists of a 35 mm single lens reflective camera and a 300 W quartz-halogen lamp. Photographs were taken using high-speed films (ISO 1000) at high shutter speeds (1/2000 to 1/8000 of a second) at low disk speed.

3.3.3 Motion Analyzer

A KODAK EKTAPRO 1000 motion analyzer was used to record the entire process of fiber formation. It was used to observe the instability initiation and growth, and measure fiber growth velocity. The motion analyzer consists of a video imager, a keypad, a processor, a monitor and the specialized tapes. The analog video signal, which represents the image captured by the lens, is collected, amplified and processed in the imager. The processor is required for control of the video system and further process the video signal. The keypad is used to set operation parameters and configure the system for the desired mode of operation. The system operates in either live, record or play modes. When operating in the live mode, the processor monitor displays the picture that will be recorded. The picture composition, exposure and focus are all exactly as they appear when a recording is played back. In the record mode, the image appearing on the monitor is recorded on the tape exactly as in the live mode, however, the tape transport command is used to move tape at the selected speed. The tape speed varies according to the desired frame rate. The higher the frame rate, the faster the tape moves. A recorded event can be reviewed in slow motion while in the play mode. In the play mode, the tape is first rewound to the beginning of the recording and then moved forward at 7.5 inches per second. Also, a jog mode is provided to play a tape at selected rate and direction.

The experimental thread formation process was recorded on a tape at low disk rotation speeds of 90 and 150 rpm at different recording rates. The images showed

clearly how a thread grows. The video tape recording these images is attached with this thesis. This technique was limited to low disk rotation speeds because of the low spatial resolution (192x239 pixels) and frame rate of the Motion Analyzer.

3.4 Experimental Procedures

The experimental testing was performed based on the following steps:

1. Select a liquid, and fill the liquid into the container. In this study, 2.5 kilograms of liquid mixture with composition of 95 wt% glycerine and 5 wt% water was selected, and poured into the container.
2. Install a disk with a selected diameter. Two disks with diameters of 0.381 m and 0.457 m were used in this study.
3. Start the spinning machine and select the disk rotation speed by adjusting the DC motor rotation speed based on the correlation between the disk rotation speed and the output voltage of the tachometer as shown in Figure A1 in Appendix A. The rotation speed range of 90-1560 rpm was selected for all of the experimental testing.
4. Start the pumping system, and select the liquid flow rate by adjusting the ball valve based on the correlation between the flow rate and output voltage of the flow meter shown in Figure A2 in Appendix A. The flow rate range used in the experiments was 1.262×10^{-5} - 3.785×10^{-5} m³/s (0.2-0.6 GPM).
5. Select the liquid temperature by adjusting the relay control system. The temperature range for the glycerine testing was 20-65 °C.

6. Record images using the recording device. The images on the center plane perpendicular to the disk axis were focused by the cameras, and recorded using the proper lights, shutter speeds, aperture settings, and recording rates.

About 50 high shutter speed (1/2000 to 1/8000 of a second) photographs were taken using the 35 mm camera and quartz-halogen lamp system. About 10 middle shutter speed (1/125 to 1/400 of a second) photographs were taken using the large format camera and laser light system. Although the resulting images from these two optical systems provide insight into the nature of fiber motion relative to the inertial reference frame, neither of these optical systems had sufficient resolution to allow measurement of fiber diameters in the range of 30-100 μm .

The large format camera and strobe light using ISO 800, 400 and 320 Polaroid films was found to have greater spatial resolution and proved to be an effective tool for acquiring quantitative measurements of fiber diameter, length and instability wavelength. About 180 pictures were taken using this optical system. Photographs were taken at different disk rotation speeds, disk diameters, camera magnifications (M) and liquid viscosities to study how these controllable parameters affect the formed fiber parameters independently.

7. Measure and calculate fiber parameters from the recording images. The detail measurements from images recorded by the three recording devices are discussed in Chapter 4.

CHAPTER 4

RESULTS AND DISCUSSION

This chapter presents experimental modeling results and discussion. First, the phenomena observed from experimental testing are described. Second, the effects of the controllable parameters on the thread parameters are qualitatively analyzed. Third, the measured thread parameters from recorded pictures and associated uncertainty analyses are presented. Fourth, the relationships between the thread parameters and the controllable parameters are quantitatively introduced, and their physical meaning is explained. Finally, the effective mass flow rate is estimated and the possibility of making fibers from lower viscosity melts by the spinning process is proposed.

4.1 Observed Phenomena from the Experimental Model

Figures 4.1 and 4.2 indicate the typical phenomena observed from photographs taken using both the 35 mm camera and quartz-halogen light system and the large format camera and laser light system. Qualitatively, there are large numbers of thread ligaments leaving the disk outer surface at a small angle with respect to the disk tangent direction. The solid lines from both figures represent the ligament extension line while the dashed lines represent the disk tangent direction at the intersection point of the ligament extension line and the disk outer diameter.

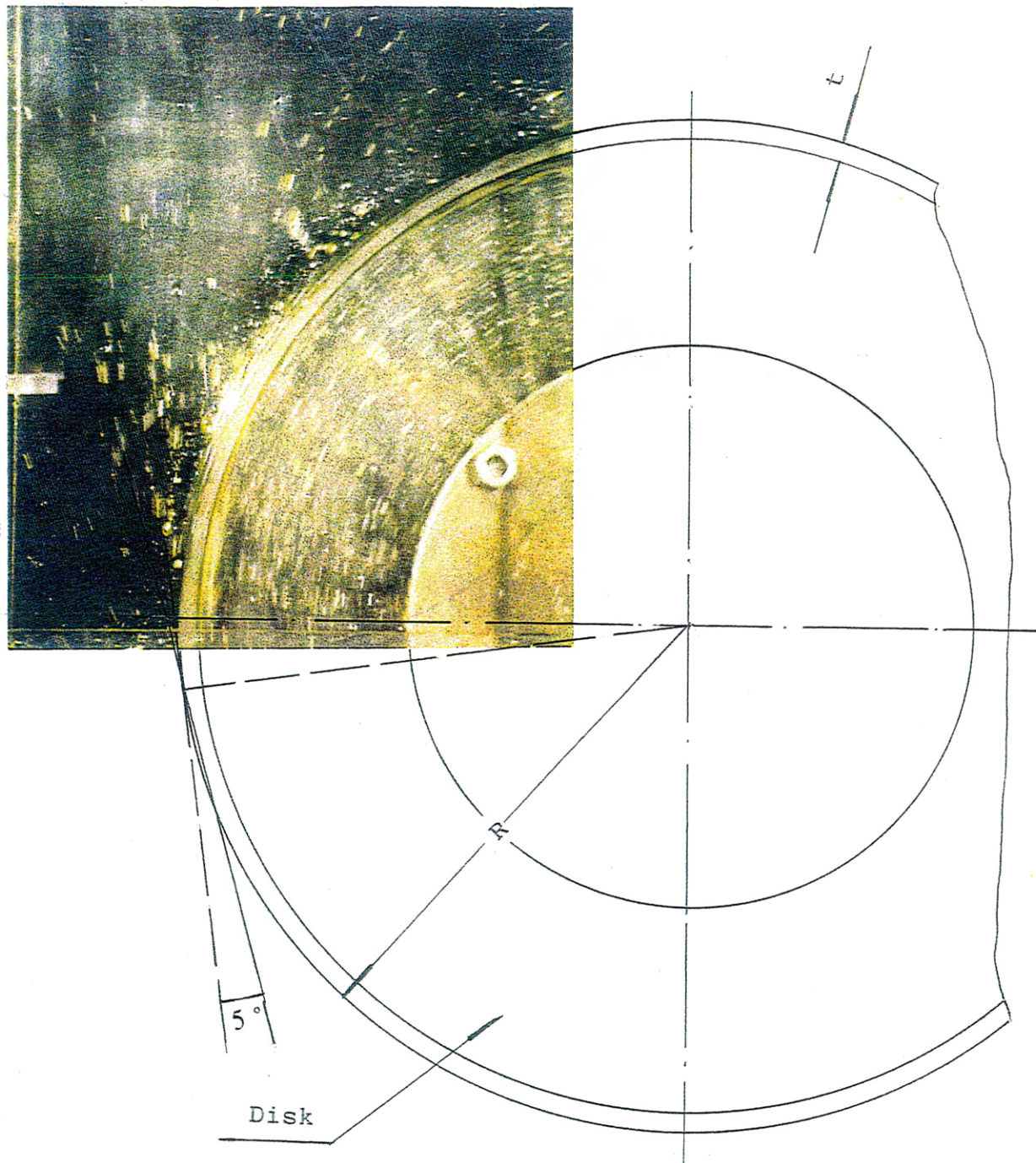


Figure 4.1. Photograph taken using 35 mm camera with quartz halogen lights at $n=260$ rpm, $D=0.381$ m, $T=25$ °C, $Q=0.2$ GPM and $M=0.15$.

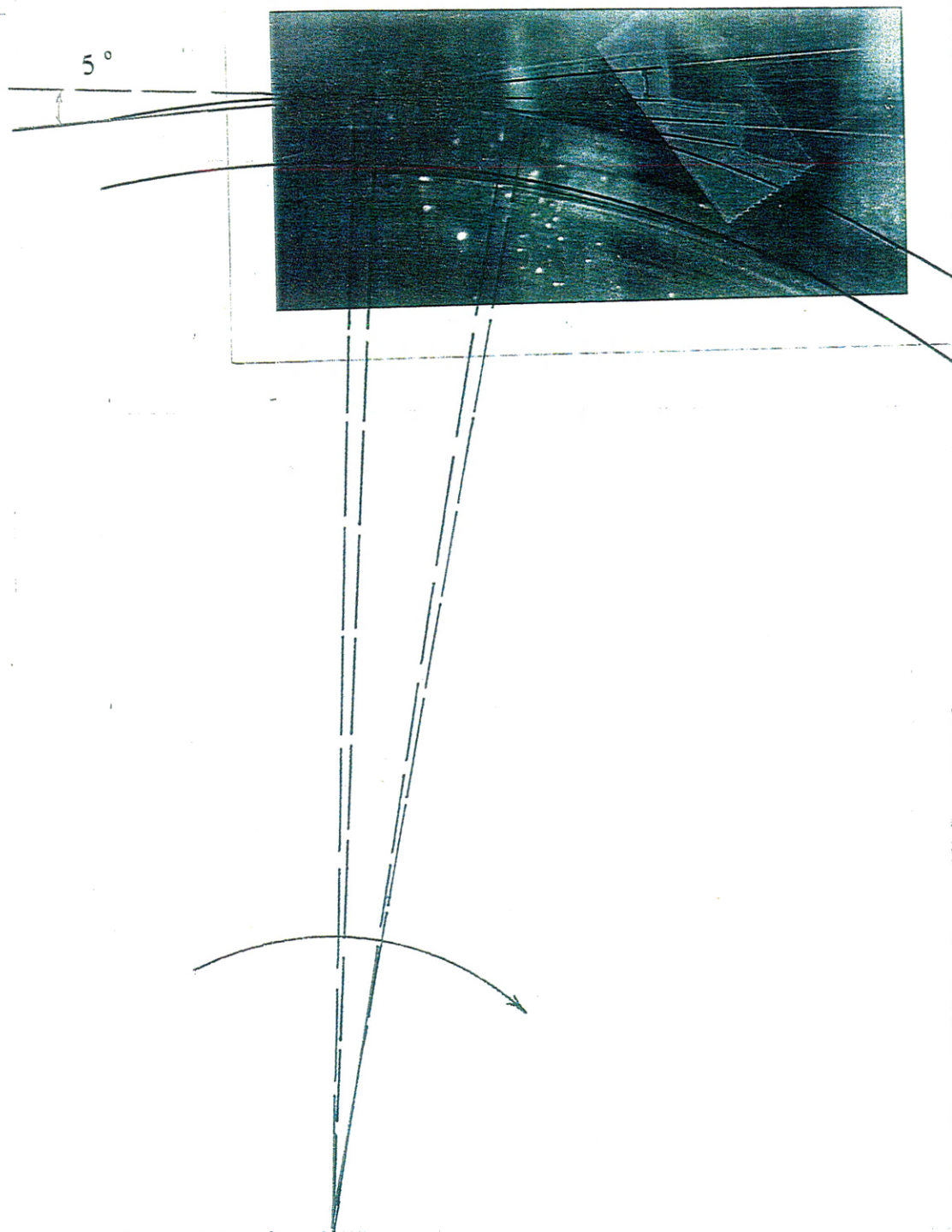


Figure 4.2. Photograph taken using large format camera and laser light system at $n=260$ rpm, $D=0.381$ m, $T=25$ °C, $Q=0.2$ GPM and $M=1.5$.

The center of the disk in each figure is found based on the arc of the disk in the picture. The tangent lines are precisely drawn at the intersection points after the location of the disk center is determined.

The angle between the ligament extension line and disk tangent line is between 5 and 10 degrees for runs at a disk speed of 260 rpm and disk diameter of 0.381 m as shown in the two figures. This implies that there is a component of fiber velocity in the disk radial direction. The radial velocity component is due to Rayleigh-Taylor instability. Since the disk rotation motion is the dominant motion relative to the inertial reference frame, the radial motion due to thread formation is very difficult to observe with these two optical systems.

Since a stroboscope can freeze the oscillatory motion, the radial motion occurring during thread formation can be observed under the reference frame of the rotating disk. The radial motion is much slower than the disk rotation motion. Photographs taken by a large format (102 mm X 127 mm) TOYO-VIEW 45C camera and a stroboscope system captured the fiber formation process and allowed the quantitative measurement of thread diameters, lengths, and the instability wavelength. Figure 4.3 shows typical photographs taken using this system. It was observed that the thread direction is not really in the radial direction relative to the disk, but is angled slightly backward from the disk rotation direction. This is due to a resisting force from air drag. Photographs were taken at different disk rotation speeds, disk diameters, camera magnifications (M) and liquid viscosities to study the effects of

various factors on thread parameters independently. Section 4.2 will qualitatively describe how the controllable parameters affect the thread parameters based on these photographs. Also, the depth of field, ΔH , the distance from the nearest to the farthest subjects which appear sharply focused (Henney and Dudley, 1939), was calculated for these photographs taken by the large format camera and stroboscope system. The calculation was based on the following data of this system: focal length of the camera lens is 210 mm, the f-stop number of aperture is $f/8$ or $f/11$, the wavelength of lights is $0.5 \mu\text{m}$ for blue lights and the object distance to which the camera is focused was 1100 mm. The calculated depth of field for each photograph is indicated by ΔH in the figure title.

The dynamic motion of thread growth was recorded by the high speed motion analyzer on a video tape for disk rotation speeds of 90 and 150 rpm (see attached tape). Thread length was measured by using the video frame rate as the clock, the growth velocity of the thread was calculated.

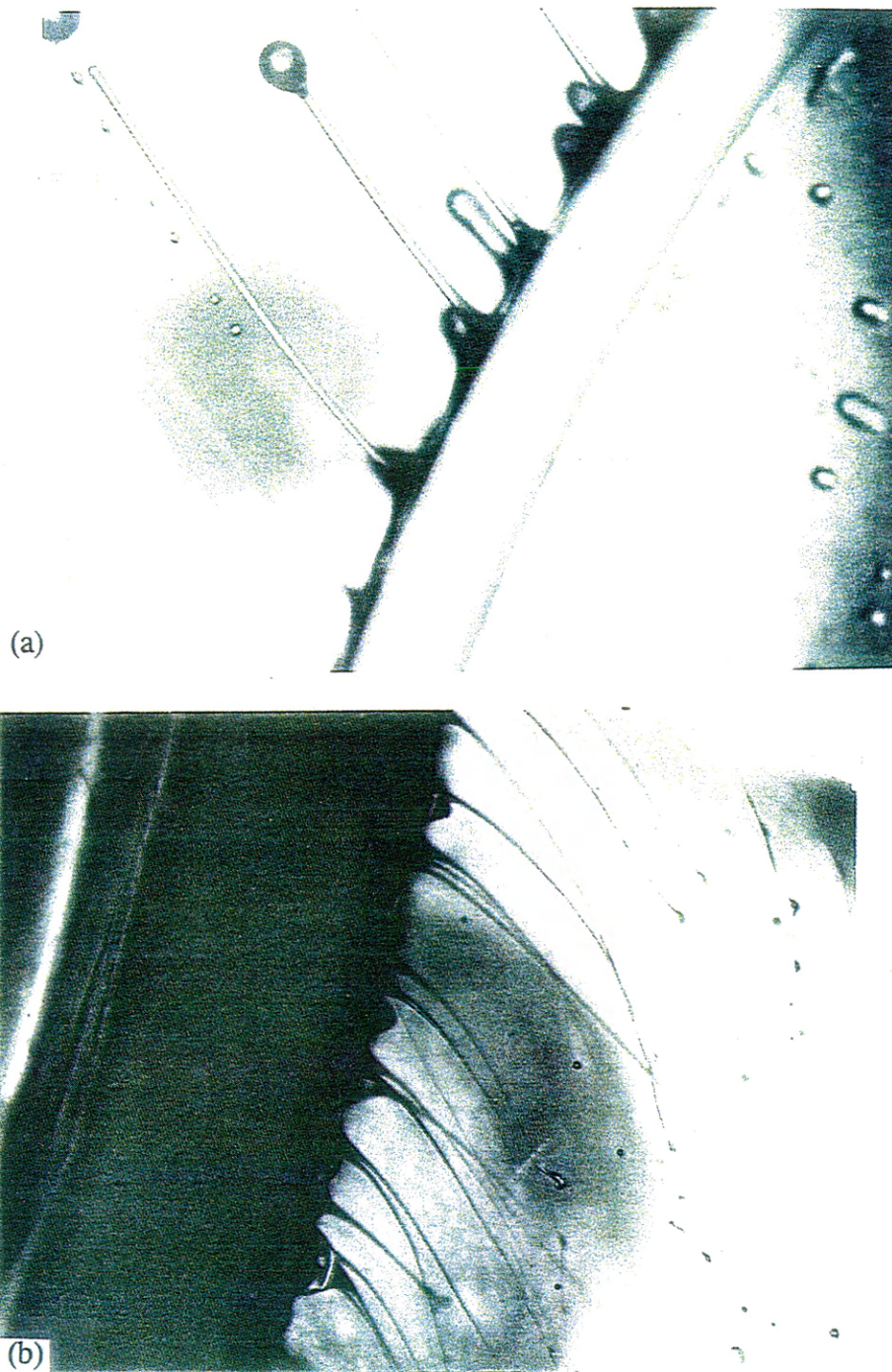


Figure 4.3. Photographs taken by large format camera and stroboscope system:
(a) $n=90$ rpm, $D=0.381$ m, $T=41$ °C, $M=2.2$, $\Delta H=6$ mm.
(b) $n=400$ rpm, $D=0.381$ m, $T=25$ °C, $M=4.39$, $\Delta H=4.4$ mm.

4.2 The Effects of the Controllable Parameters on Thread Parameters

The effect of each controllable parameter including disk rotation speed and diameter and liquid viscosity on the thread parameters is discussed in this section individually. The results are based on measurements taken from the photographs using the large format camera and stroboscope system and high speed video tape.

4.2.1 The Effect of Disk Rotation Speed on Thread Parameters

The effect of disk rotation speed on thread parameters is shown on Figure 4.4a-f. Disk rotation speeds were changed from 260 to 1560 rpm, at constant disk diameter ($D=0.381$ m) and the glycerine viscosity ($\mu=0.336$ N-s/m² at temperature $T=25$ °C for the 95 wt% glycerine, 5 wt% water composition).

These six photographs show that thread diameter, length and instability wavelength decrease as the disk rotation speed increases while other controllable variables remain constant. Photographs taken using the large format camera and laser system also illustrate this tendency on thread diameter as shown in Figure 4.5a-b.

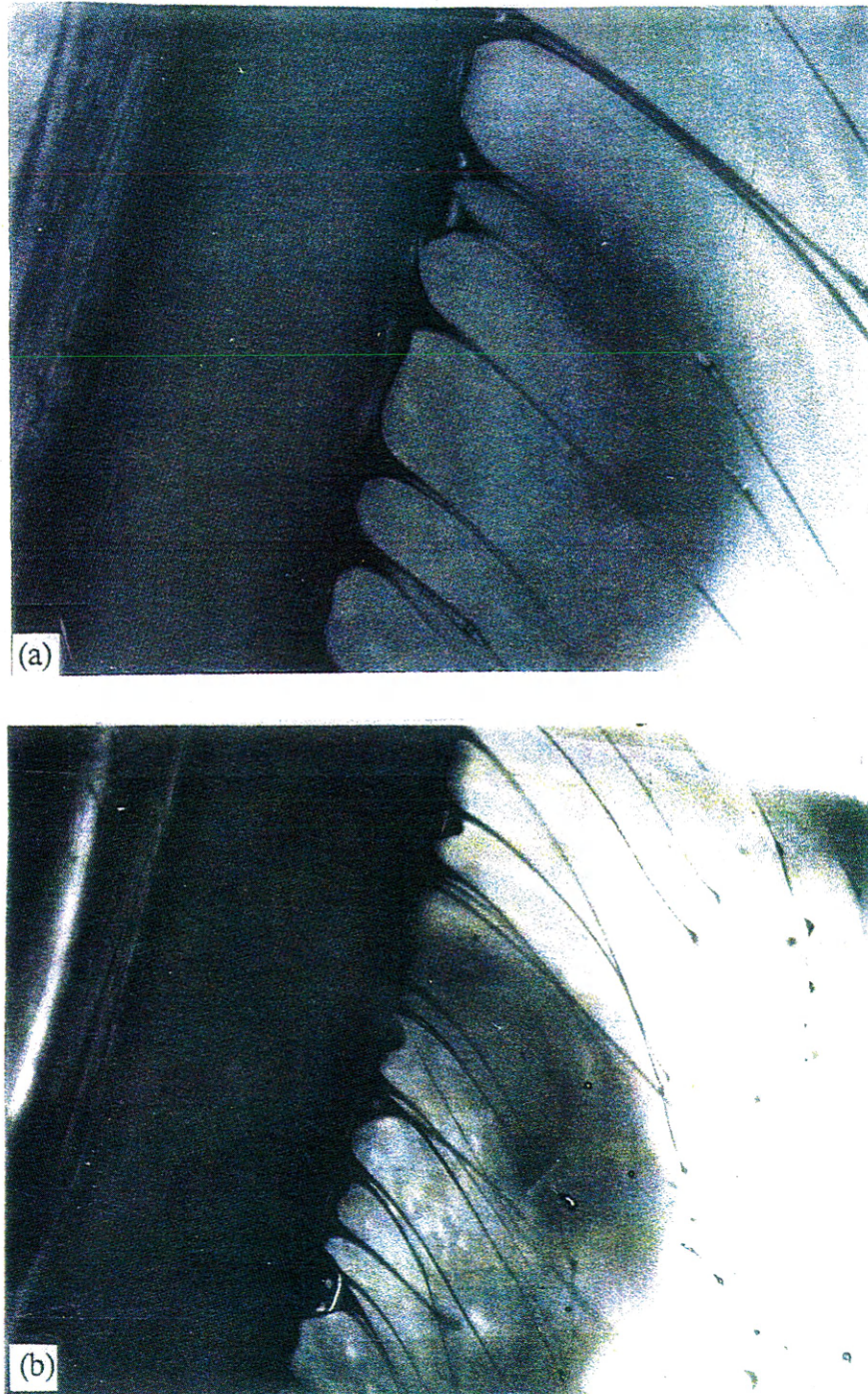


Figure 4.4. Photographs taken using the large format camera and stroboscope system for different rotation speeds n at $D=0.381$ m, $T=25$ °C, $\Delta H=4.3$ mm, $M=4.39$: (a) $n=260$ rpm, (b) $n=400$ rpm.

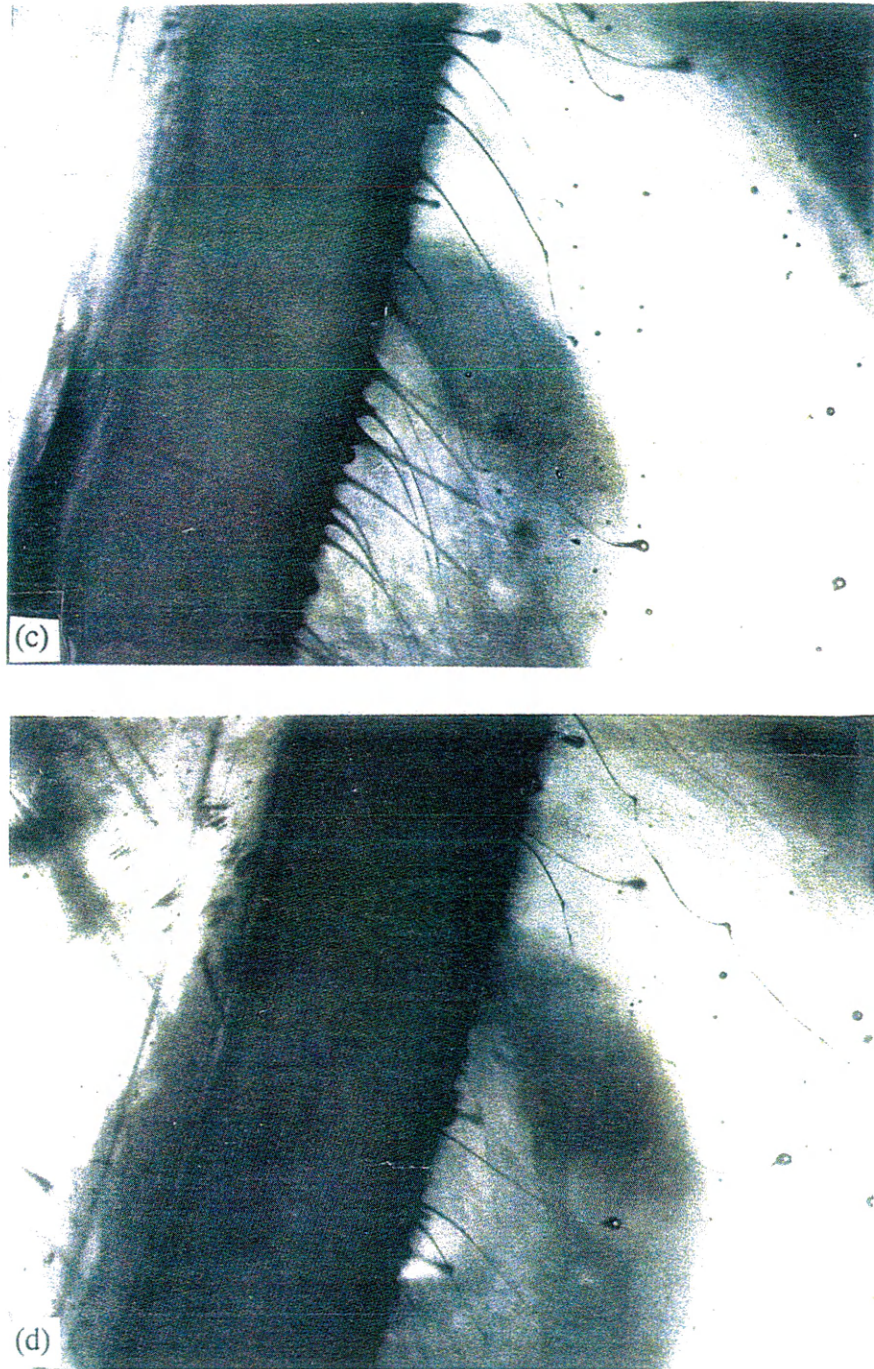


Figure 4.4. Photographs taken using the large format camera and stroboscope system for different rotation speeds n at $D=0.381$ m, $T=25$ °C, $\Delta H=6.7$ mm, $M=4.39$: (c) $n=670$ rpm, (d) $n=920$ rpm.

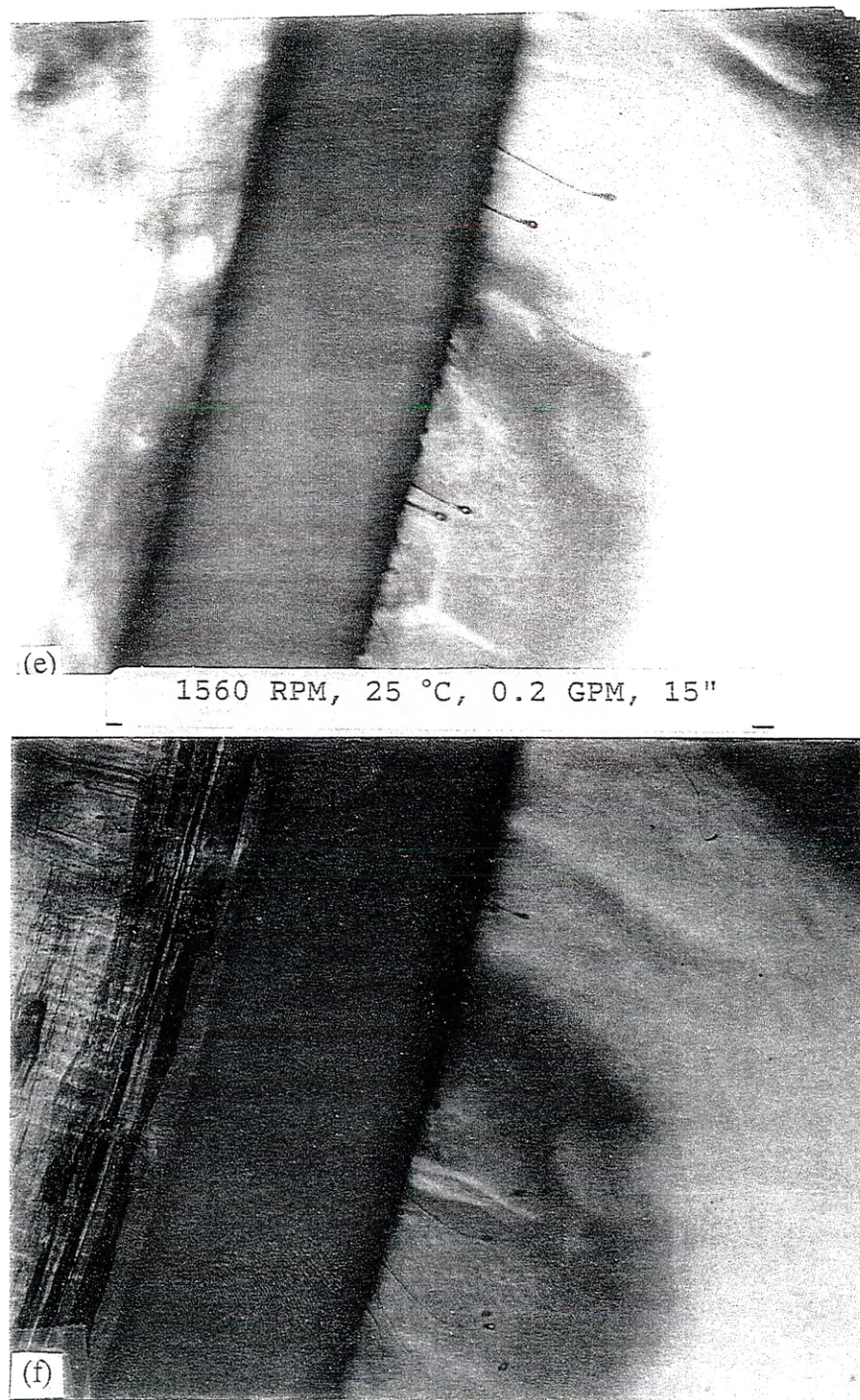


Figure 4.4. Photographs taken using the large format camera and stroboscope system for different rotation speeds n at $D=0.381$ m, $T=25$ °C, $\Delta H=6.7$ mm, $M=4.39$: (e) $n=1200$ rpm, (f) $n=1560$ rpm.

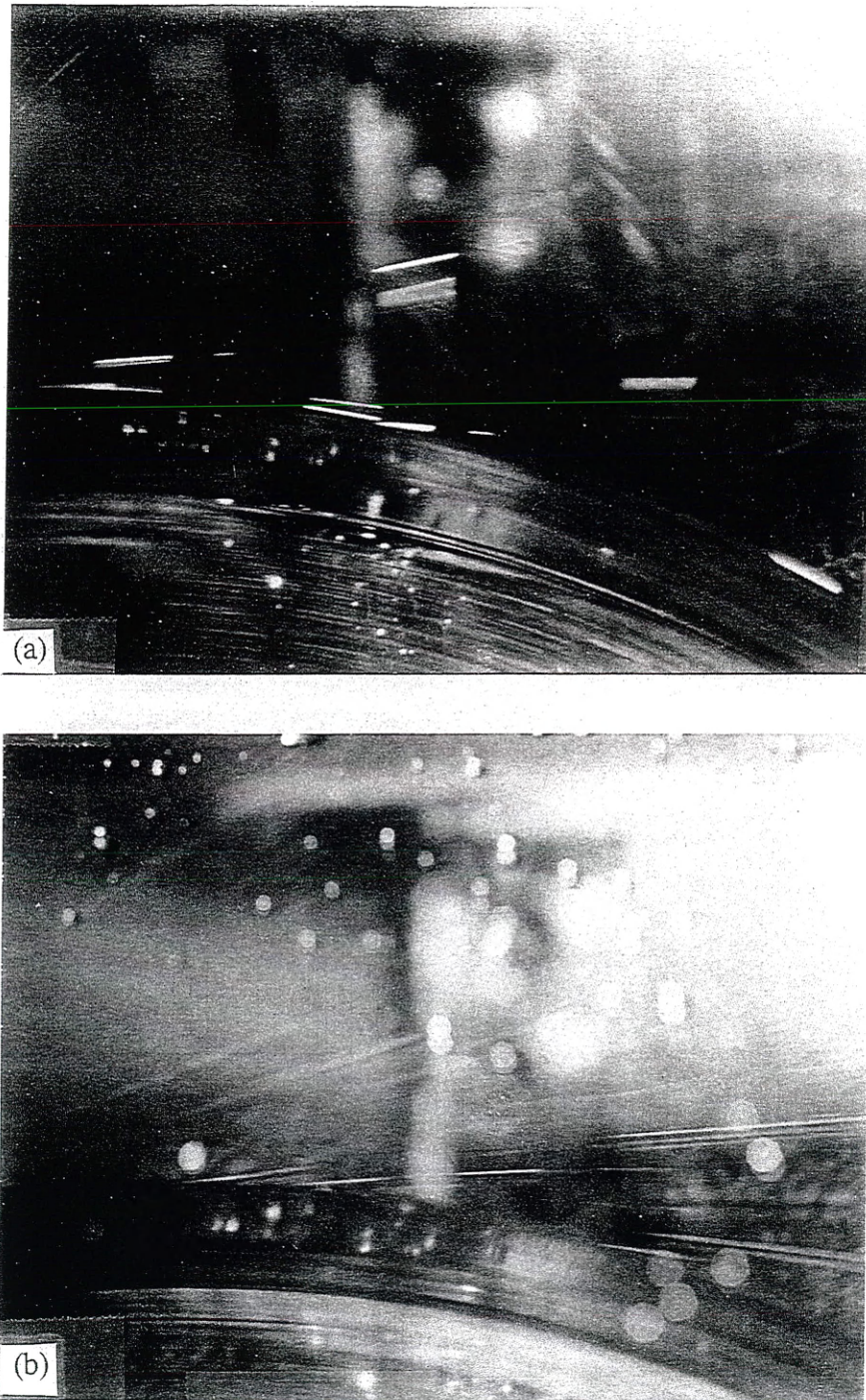


Figure 4.5. Photographs taken using the large format camera and laser system for different rotation speeds n at $D=0.381$ m, $T=25$ °C, $Q=0.2$ GPM and $M=1.76$: (a) $n=90$ rpm, (b) $n=260$ rpm.

4.2.2 The Effect of Liquid Viscosity on Thread Parameters

The effect of glycerine viscosity on thread parameters is shown on Figure 4.6 (a)-(d). The disk rotation speed and diameter, liquid flow rate, and camera magnification were held constant. The glycerine viscosity was varied with the liquid temperature at a constant when liquid composition of 95 wt% glycerine and 5 wt% water. The viscosity varied from 0.336 N-s/m² to 0.051 N-s/m² as the temperature was changed from 25 °C to 50 °C.

The four photographs show that the thread parameters decrease as the temperature increases. Since liquid viscosity decreases as temperature increases, the thread parameters decrease as liquid viscosity decreases when the other controllable parameters are held constant.

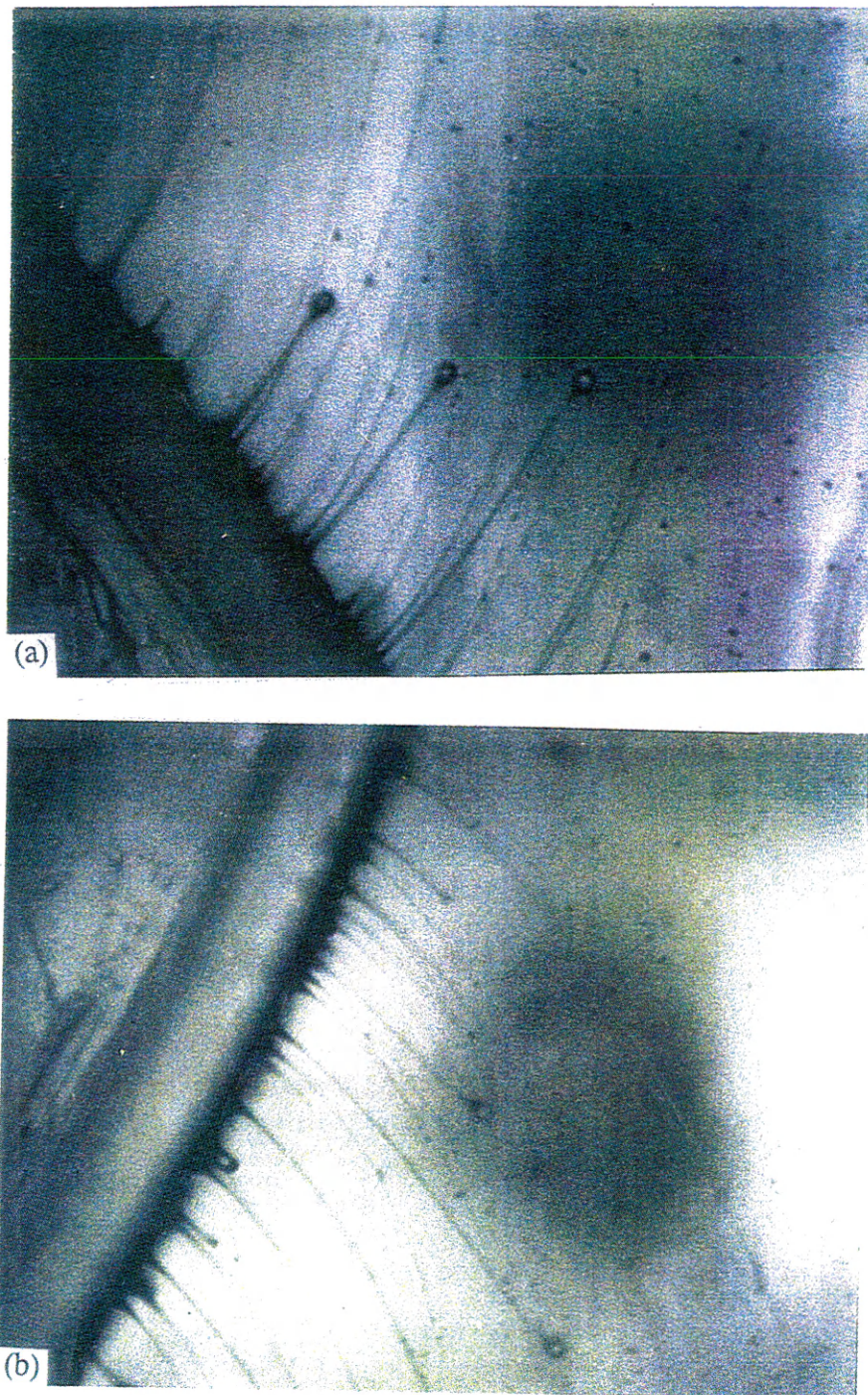


Figure 4.6. Photographs taken using the camera-stroboscope system for varied viscosities at $n=260$ rpm, $D=0.381$ m, $M=1.9$, $\Delta H=6$ mm: (a) $\mu=0.336$ N-s/m², $T=20$ °C, (b) $\mu=0.24$ N-s/m², $T=30$ °C.

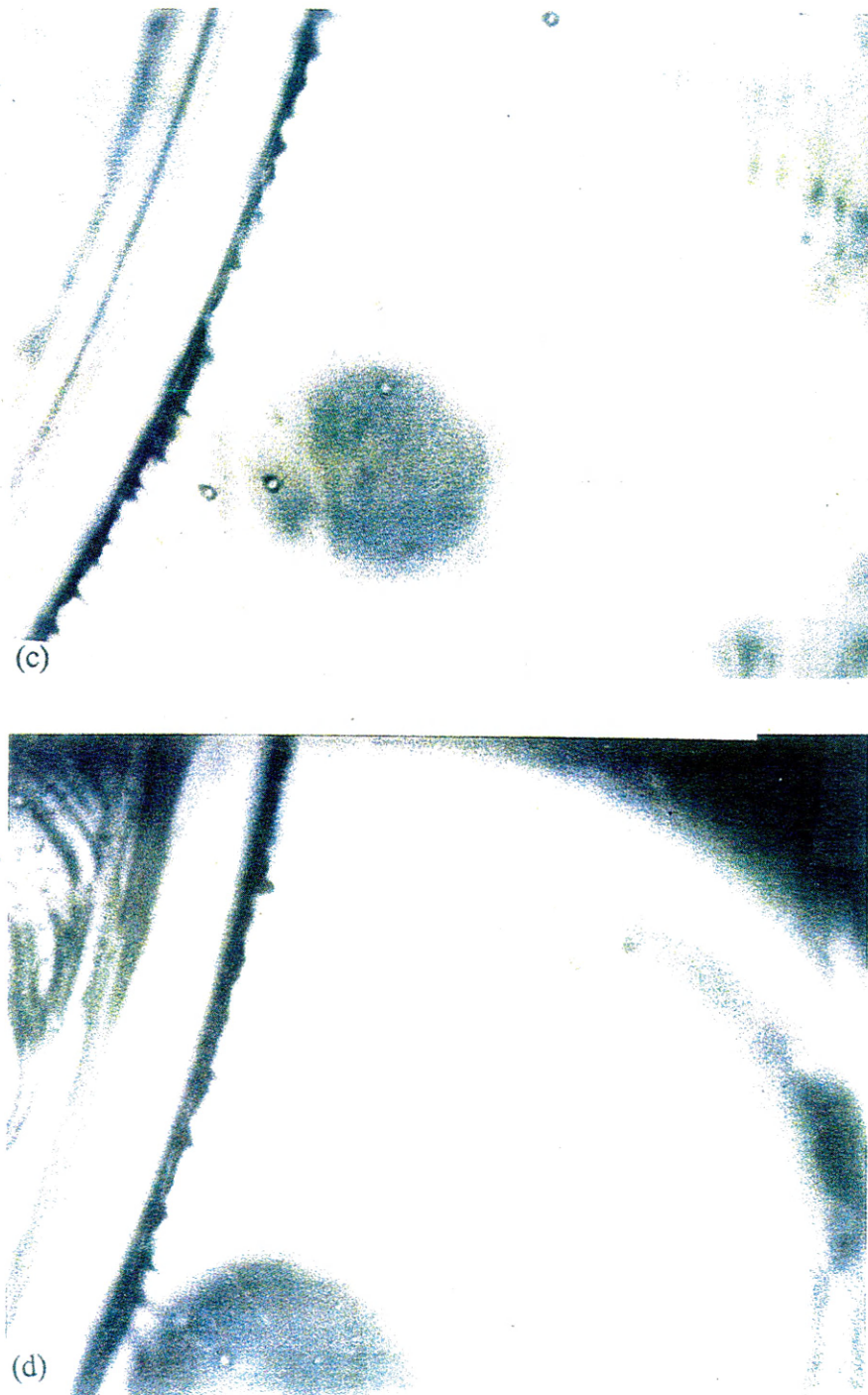


Figure 4.6. Photographs taken using the camera-stroboscope system for varied viscosities at $n=260$ rpm, $D=0.381$ m, $M=1.9$, $\Delta H=6$ mm: (c) $\mu=0.108$ N-s/m², $T=40$ °C, (d) $\mu=0.051$ N-s/m², $T=50$ °C.

4.2.3 The Effect of Disk Diameter on Thread Parameters

The effect of disk diameter or disk curvature on thread parameters is shown in Figure 4.7a-b for low disk rotation speed and Figure 4.8a-b for middle disk rotation speed. The disk diameter was varied between 0.457 meters, 0.381 meters and 0.203 meters, while the disk rotation speed, the glycerine viscosity and the camera magnification were held constant for the 95 wt% glycerine and 5 wt% water composition.

Both figures show that the fiber diameter, length and the instability wavelength for the 0.457 meters disk diameter are slightly smaller than those for the 0.381 meter disk diameter. This indicated that thread parameters decrease with increasing disk diameters when the other controllable parameters are held constant.

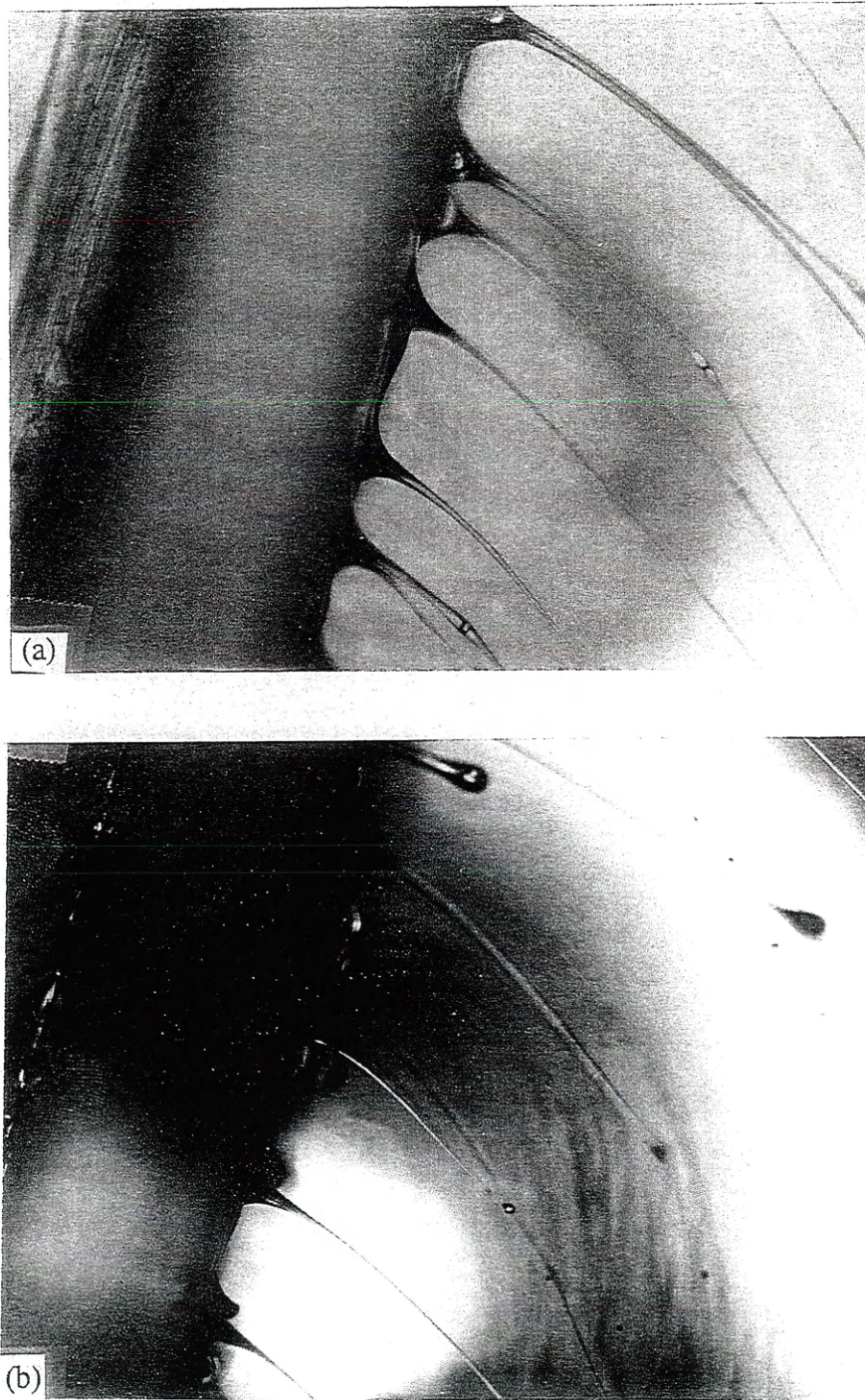


Figure 4.7. Photographs taken using the large format camera and stroboscope system for different disk diameter at $n=260$, $T=25\text{ }^{\circ}\text{C}$, $M=4.39$, (a) $D=0.381\text{ m}$, $\Delta H=4.3\text{ mm}$, (b) $D=0.457\text{ m}$, $\Delta H=6.7\text{ mm}$.

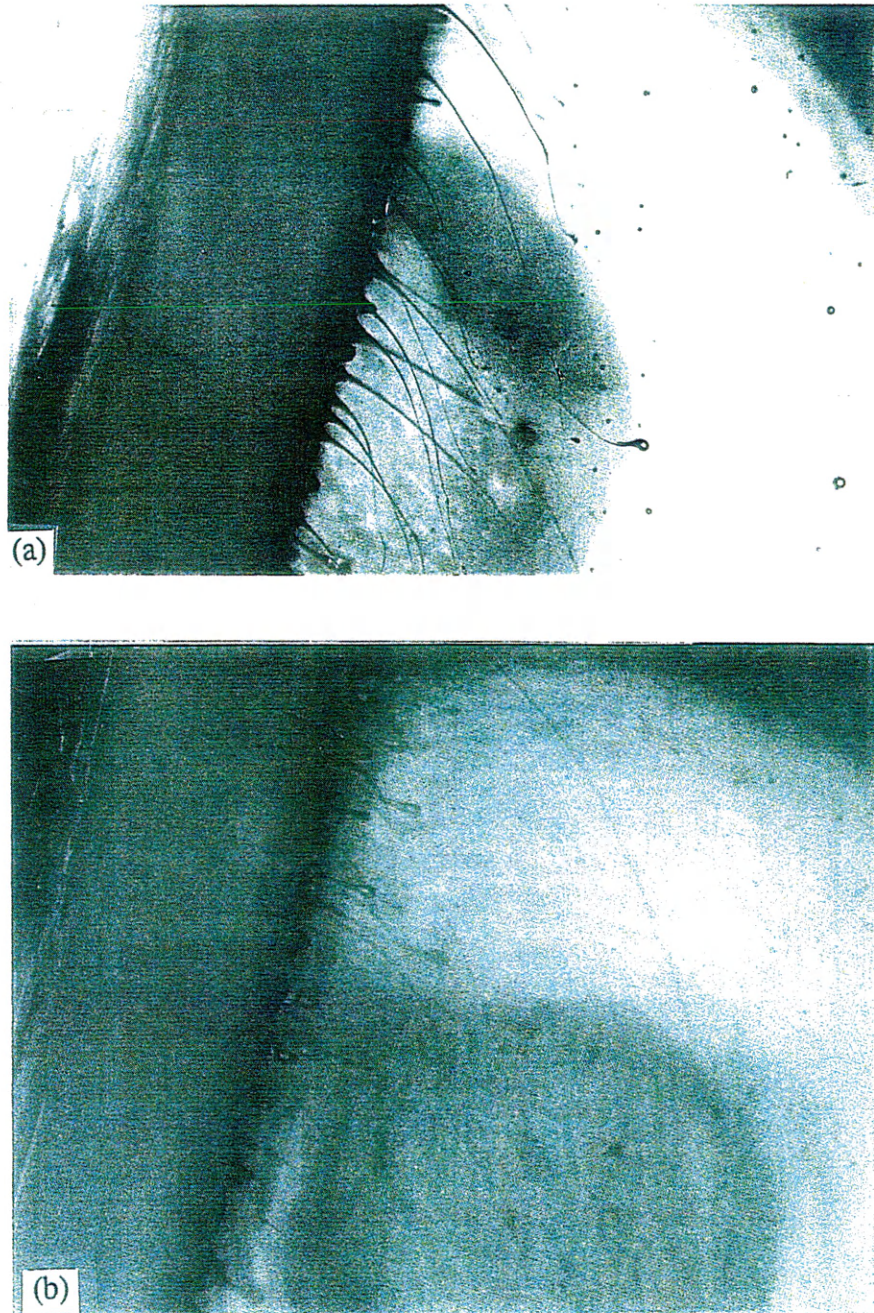


Figure 4.8. Photographs taken using the large format camera and stroboscope system for different disk diameter at $n=670$, $T=25\text{ }^{\circ}\text{C}$, $M=4.39$, (a) $D=0.381\text{ m}$, $\Delta H=6.7\text{ mm}$, (b) $D=0.457\text{ m}$, $\Delta H=6.7\text{ mm}$.

From the above analysis, it is realized that the thread parameters decreased with increasing the disk rotation speed and diameter and decreasing the liquid viscosity and surface tension. By comparing Figure 4.4 with Figures 4.6-4.8, it is also noticed that the fiber parameters decreased more rapidly due to increasing the disk rotation speed than they did due to both decreasing the liquid viscosity and increasing the disk diameter. This means that the disk rotation speed, when comparing the effects of the other two controllable parameters, plays a major role in changing the fiber parameters. This is also consistent with the previous results expressed in equation 2.1 where the number of fibers was proportional to $V^{10/12}$ (the disk tangent velocity) and $D^{7/12}$ (the disk diameter), and inversely proportional to $\mu^{4/12}$ (liquid viscosity).

4.3 Measurement and Calculation of Thread Parameters

This section presents how the thread parameters are measured and calculated. First, the measurement and calculation of thread diameter, thread length, and wavelength of the instability are discussed. The thread parameters were scaled on the images using the disk rim wall thickness (6.8 mm) as a reference length. Next, the uncertainty analysis is presented for measurements of the thread and controllable parameters. Finally, the calculation of thread growth velocity is introduced.

4.3.1 Measurement of Thread Diameter, Length Instability Wavelength

Thread diameter (d), length (L) and wavelength (λ) of the instability have been measured by an optical magnifier with a gradation on the uncertainty of ± 0.05 mm, and calculated from photographs taken using the large format camera and stroboscope system. They were calculated as follows: let F_r represent the experimentally determined real thread parameter (such as d, λ , L), it is equal to the measured thread parameter F_m on a picture divided by the magnification M of that picture taken at the specific controllable parameters. M is a ratio of the disk wall thickness t_m measured on the photograph to the real thickness t_r measured on the disk itself. Therefore, the real thread parameter is

$$F_r = \frac{F_m}{M} = \frac{F_m}{\frac{t_m}{t_r}} = F_m \frac{t_r}{t_m} \quad (4.1)$$

The thread parameters for most threads on each picture are calculated using this formula, and their averaged value is taken as thread parameter datum for each picture. Since each photograph represents a particular combination of the controllable parameters, each datum corresponds to one combination of controllable parameters. Tables 4.1-4.3 list the real thread diameter, length, and instability wavelength, respectively, for different disk diameters, rotation speeds and glycerine temperatures.

**Table 4.1. Thread Diameter for 95 wt% Glycerine
and 5 wt% Water System**

	T °C	μ N-s/m ²	Calculated thread diameter (μ m) at different rotation speed (rpm)					
			260	400	670	920	1200	1560
D = 0.457 m	25	0.336	100	84	64	50	34	27
	40	0.108	88	75	54	45	31	23
	50	0.051	84	67	48	41	26	20
	60	0.024	80	63	42	35	25	20
D = 0.381 m	25	0.336	136	99	75	56	46	38
	40	0.108	127	81	65	42	39	32
	50	0.051	113	75	55	36	30	27
	60	0.024	104	67	47	32	26	22

**Table 4.2. Thread Length for 95 wt%
Glycerine and 5% Water System**

	T °C	μ N-s/m ²	Calculated thread length (mm) at different rotation speed (rpm)					
			260	400	670	920	1200	1560
D = 0.457 m	25	0.336	11.2	9.4	8.2	6.2	5.2	3.6
	40	0.108	10.8	8.0	6.1	4.5	3.6	2.8
	50	0.051	9.6	7.2	5.0	4.0	3.2	2.4
	60	0.024	8.7	6.5	4.8	3.5	2.9	2.2
D = 0.381 m	25	0.336	17.0	11.1	8.6	6.7	5.7	4.4
	40	0.108	11.1	8.1	6.2	5.0	4.3	3.8
	50	0.051	11.0	7.5	5.5	4.1	3.5	2.5
	60	0.024	9.4	6.7	5.5	3.8	3.2	2.4

Table 4.3. Instability Wavelength for 95 wt% Glycerine and 5 wt% Water System

	T °C	μ N-s/m ²	Calculated instability wavelength (mm) at different rotation speed (rpm)			
			260	400	670	920
D = 0.457 m	25	0.336	3.17	2.17	1.38	0.59
	40	0.108	2.94	1.96	1.32	0.59
	50	0.051	2.30	1.76	1.13	0.56
D = 0.381 m	25	0.336	4.41	2.45	1.78	0.90
	40	0.108	2.86	1.61	1.09	0.85
	50	0.051	2.72	1.39	0.88	0.65

4.3.2 Uncertainty Analysis on Measurements

As discussed above, the fiber parameters are not measured from the photographs directly, but are calculated by the equation (4.1). Assuming that the experimental model is dynamically similar to the actual process, the fiberization process is functionally related to the Reynolds and Weber numbers. Each fiber parameter is therefore correlated to a dimensionless variable F with a reference length scale D (rotation disk diameter), and equal to

$$F = \frac{F_r}{D} = \frac{F_m}{D M} = \frac{F_m t_r}{D t_m} \quad (4.2)$$

The uncertainty of the F value was determined from the uncertainty of the measurements of disk diameter, disk wall thickness, and the wall thickness measured on the photographs.

The Reynolds and Weber numbers are calculated from the controllable parameters and liquid properties. Therefore, the uncertainty of any combination of these numbers depends on the uncertainty of the variables and properties from which they are formed. For example, the product P of Reynolds and Weber numbers is expressed as

$$P = Re * We = \left(\frac{VD\rho}{\mu}\right)\left(\frac{V^2D\rho}{\sigma}\right) \quad (4.3)$$

$$= \left(\frac{\pi}{60}\right)^3 \frac{n^3 D^5 \rho^2}{\mu \sigma}$$

The uncertainty of P value was determined by the uncertainty of measurements of disk diameter, disk rotation speed, and liquid operating temperature on which the liquid properties depend.

Taking the thread parameters and combination of dimensionless numbers as the experimentally determined function (Θ), the uncertainty of Θ is determined from the uncertainty of its dependent variables ϕ_i . The method of estimating the propagation of measurement uncertainty presented by Holman and Gajda (1989) was used to estimate uncertainty in this study. The uncertainty for the experimental results is estimated on the basis of the uncertainties in the primary measurements.

The relationship Holman and Gajda (1989) provided was applied to the experimentally determined function (Θ), so that the uncertainty in that function (W_Θ) could be determined while using estimates of the uncertainties of each fiber and controllable parameter ϕ .

$$W_\Theta = \sqrt{\sum_{i=1}^n \left(\frac{\partial \Theta}{\partial \phi_i} W_{\phi_i} \right)^2} \quad (4.4)$$

Therefore, for the experimentally determined function of fiber parameters (F), the uncertainties for F is

$$\begin{aligned} W_F &= \sqrt{\left(\frac{\partial F}{\partial F_m} W_{F_m} \right)^2 + \left(\frac{\partial F}{\partial D} W_D \right)^2 + \left(\frac{\partial F}{\partial t_r} W_{t_r} \right)^2 + \left(\frac{\partial F}{\partial t_m} W_{t_m} \right)^2} \\ &= \sqrt{\left(\frac{t_r}{Dt_m} W_{F_m} \right)^2 + \left(\frac{F_m t_r}{t_m D^2} W_D \right)^2 + \left(\frac{F_m}{Dt_m} W_{t_r} \right)^2 + \left(\frac{F_m t_r}{Dt_m^2} W_{t_m} \right)^2} \end{aligned} \quad (4.5)$$

for the product of Re and We (P), the uncertainty of P is

$$\begin{aligned} W_P &= C \sqrt{\left(\frac{\partial P}{\partial n} W_n \right)^2 + \left(\frac{\partial P}{\partial D} W_D \right)^2 + \left(\frac{\partial P}{\partial \rho} W_\rho \right)^2 + \left(\frac{\partial P}{\partial \mu} W_\mu \right)^2 + \left(\frac{\partial P}{\partial \sigma} W_\sigma \right)^2} \\ &= C \frac{n^2 D^4 \rho}{\mu \sigma} \sqrt{(3D\rho W_n)^2 + (5n\rho W_D)^2 + (2DnW_\rho)^2 + \left(\frac{nD\rho}{\mu} W_\mu \right)^2 + \left(\frac{nD\rho}{\sigma} W_\sigma \right)^2} \end{aligned} \quad (4.6)$$

where $C=(\pi/60)^3$ is a constant. The units for all variables in above equations are the SI units.

The uncertainty calculations are performed for three points. Point A is taken at $n=260$ rpm, $D=0.381$ m, $T=25$ °C. Point B is taken at $n=1560$ rpm, $D=0.457$ m and $T=60$ °C. Point C is taken at $n=920$ rpm, $D=0.457$ m and $T=50$ °C.

Uncertainties of P values are calculated at all three points. Uncertainties of thread diameter and length are calculated at point A and B while uncertainty of the instability wavelength is calculated at points A and C. The measured dependent variables and their uncertainties are listed in Table 4.4 for the three points mentioned above. The uncertainty of each dependent variable is estimated based on measuring tools. The liquid properties and their uncertainties are based on the liquid temperatures and the uncertainties of the temperature measurements. Based on the input data of dependent variables, the experimentally determined functions and their uncertainties for these three points were also calculated, and are listed in Table 4.5.

**Table 4.4. Input Data of Dependent Variables
at Three Points for Uncertainty Analysis**

Variables (unit)	Point A	Point B	Point C
D (m)	0.381	0.457	0.457
W_D (m)	$\pm 3.0E-03$	$\pm 3.0E-03$	$\pm 3.0E-03$
n (rps)	4.333	26.0	15.3
W_n (rps)	± 0.167	± 1.0	± 0.6
T (°C)	25	60	50
W_T (°C)	± 1	± 2	± 2
μ (N-s/m ²)	0.336	0.024	0.051
W_μ (N-s/m ²)	$\pm 2.0E-03$	$\pm 5.0E-03$	$\pm 5.0E-03$
ρ (kg/m ³)	1250.0	1230.0	1240.0
W_ρ (kg/m ³)	± 0.5	± 1.0	± 1.0
σ (N/m)	0.064	0.061	0.062
W_σ (N/m)	$\pm 5.0E-05$	$\pm 1.0E-04$	$\pm 1.0E-04$
t_m (m)	0.03	0.031	0.032
W_{t_m} (m)	$\pm 5.0E-04$	$\pm 5.0E-04$	$\pm 5.0E-04$
t_r (m)	6.833E-03	5.969E-03	5.966E-03
W_{t_r} (m)	$\pm 5.0E-04$	$\pm 5.0E-04$	$\pm 5.0E-04$
d_m (m)	6.0E-04	1.0E-04	
W_{d_m} (m)	$\pm 5.0E-05$	$\pm 5.0E-05$	
L_m (m)	0.075	0.011	
W_{L_m} (m)	$\pm 5.0E-04$	$\pm 5.0E-04$	
λ_m (m)	0.019		3.5E-03
W_{λ_m} (m)	$\pm 5.0E-04$		$\pm 5.0E-04$

Table 4.5. Uncertainties of the Experimentally Determined Functions for Three Points

Functions		Point A	Point B	Point C
d	d/D	3.60E-04	4.40E-5	
	$W_{d/D}$	$\pm 3.02E-5$	$\pm 4.30E-6$	
	% of uncertainty	8.39	9.77	
	Log (d/D)	-3.44	-4.36	
	$W_{\text{Log}(d/D)}$	$\pm 3.50E-02$	$\pm 4.05E-02$	
L	L/D	4.50E-02	4.80E-03	
	$W_{L/D}$	$\pm 1.17E-03$	$\pm 4.42E-04$	
	% of uncertainty	2.60	9.21	
	Log (L/D)	-1.35	-2.32	
	$W_{\text{Log}(L/D)}$	$\pm 1.11E-02$	$\pm 3.83E-02$	
λ	λ/D	1.16E-02		1.30E-03
	$W_{\lambda/D}$	$\pm 6.00E-04$		$\pm 2.10E-04$
	% of uncertainty	5.17		16.2
	Log (λ/D)	-1.94		-2.89
	$W_{\text{Log}(\lambda/D)}$	$\pm 2.19E-02$		$\pm 6.50E-02$
P	P	1.48E+09	1.14E+13	1.10E+12
	W_P	$\pm 1.38E+08$	$\pm 1.19E+12$	$\pm 1.14E+11$
	% of uncertainty	9.32	10.4	10.4
	Log (P)	9.17	13.1	12.0
	$W_{\text{Log}(P)}$	$\pm 3.87E-02$	$\pm 4.31E-02$	$\pm 4.28E-02$

Table 4.5 shows that the uncertainty range for this study was about 10%. The uncertainty of the instability wavelength is slightly higher, because of the difficulty in measurement of the wavelength of 3-dimensional waves from 2-dimensional photographs taken at high disk rotation speeds. Because of the large axial disk width (about 40 mm) relative to the camera depth of field, it was difficult to determine accurately whether the waves were in the same axial plane. In other words, using 2-dimensional images, it was not possible to determine a depth scale associated with the axial dimension. The experimentally determined functions and their uncertainties are marked as error bars in Figures 4.14-4.16.

4.3.3 Calculation of the Thread Growth Velocity

The thread growth velocity V is calculated by the thread length growth ΔL divided by the time interval $\Delta\tau$ within which ΔL is generated. ΔL is the length measured as the difference of the pixel positions within $\Delta\tau$ on the monitor screen from the tape recorded by high speed Motion Analyzer, and divided by the magnification M of the recording image. M is also the ratio of the measured disk rim wall thickness t_m on the image to the real thickness t_r . The total pixel count on the screen is 240x192 (length by height of screen), which is converted to 180 mm long and 160 mm high. The value of $\Delta\tau$ is equal to the number of pictures passing through from τ_0 to τ_i divided by the recording rate [pictures per second (pps)] of the motion analyzer. Table 4.6 illustrates a typical example of the thread growth rate

calculation for a thread recorded at a disk rotation speed of 90 rpm and a video recording rate of 1000 pps.

Table 4.6. Calculation of Thread Growth Rates

Time τ_i (s)	Picture # N_i	length L_i (mm)	ΔN	$\Delta\tau = \Delta N/1000$	ΔL (mm)	$V = \Delta L/\Delta\tau$ (mm/s)
$\tau_0=0$	122	13.1				
$\tau_1=0.01$	132	19.6	10	0.01	6.5	650
$\tau_2=0.02$	142	27.8	10	0.01	8.2	820
$\tau_3=0.03$	152	38.4	10	0.01	10.6	1060
$\tau_4=0.032$	154	40.7	2	0.002	2.3	1150

The thread lengths and growth rates are calculated for different stages of thread formation recorded at different recording rates (500-6000 pps). It was found that both the thread length and growth rate are functions of time as shown in Figures 4.9 and 4.10a. At the initial stage, the thread grows very slow while it grows rapidly at the final stage. Due to the limited spatial resolution of the motion analyzer, the calculations were performed for low disk rotation speeds of 90 rpm and 150 rpm only. The functional behavior of the fiber length and growth rate, at two rotation speeds, are also compared in Figures 4.9 and 4.10a.

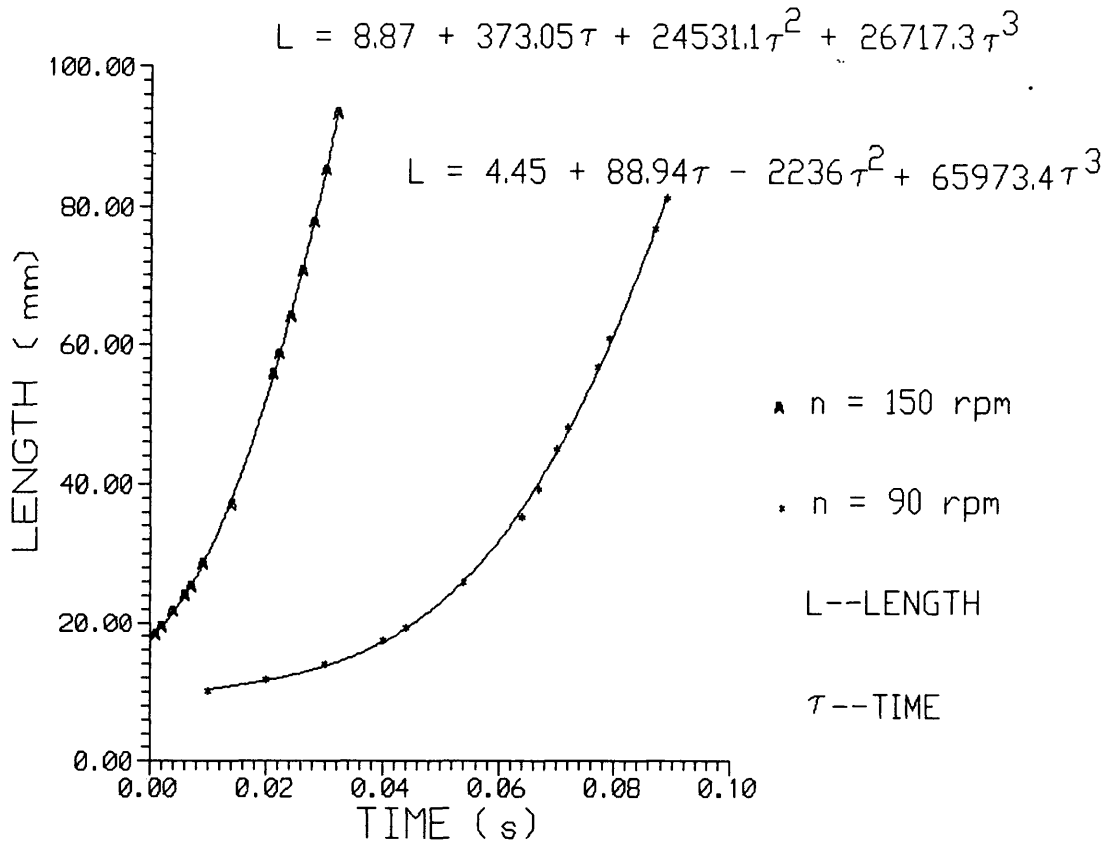


Figure 4.9. Thread growth length versus time (data obtained by the recording tape using the motion analyzer).

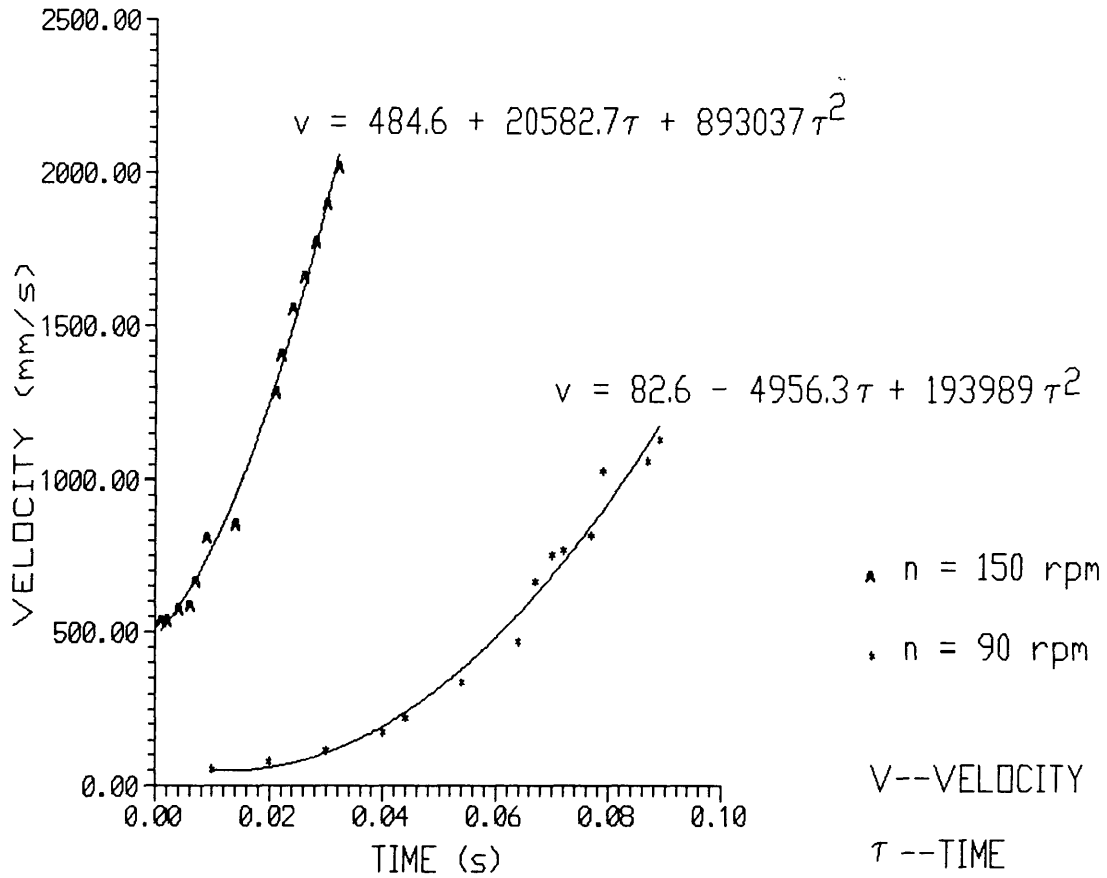


Figure 4.10a. Thread growth velocity versus time (data obtained by the recording tape using the motion analyzer).

Figure 4.9 showed that the thread growth length is a third order function of time while Figure 4.10a showed that thread growth velocity is a second order function of time for both disk rotation speeds of 90 rpm and 150 rpm. These results are consistent with the fluid dynamic theory. Velocity is the derivative of length with respect to time, and it is modeled by a polynomial one order lower than that for the length with respect to time.

Both figures show that thread length and growth velocity are functions of disk rotation speeds. They increase as the disk rotation speed increases. Therefore, a general correlation between the thread growth rate V and the disk rotation speed n is derived from the data obtained for low disk rotation speeds. The thread growth rate is expressed as

$$V = 2144.95 \ln \frac{\pi [nR - (n - n_0)R_0]}{30} - 14291.3 \quad (4.7)$$

Because of the limited resolution of the motion analyzer, no data were taken at high disk rotation speeds to test this correlation at higher speeds. Therefore, this relationship may be not very accurate at high disk speeds, but it reflects the tendency of thread growth related to the disk rotation speed. It is useful for calculation of the effective mass flow rate, \dot{m}_e . The \dot{m}_e is the mass flow rate of forming threads per unit time. Also, the effects of the other controllable parameters on the thread growth velocity were not investigated due to the above limitation. A higher resolution motion analyzer may be needed for further study on this subject.

The thread growth velocity is plotted against the relative disk tangent velocity in a natural logarithmic form as shown in Figure 4.10b. The very high R^2 value indicates that they are correlated to each other very well.

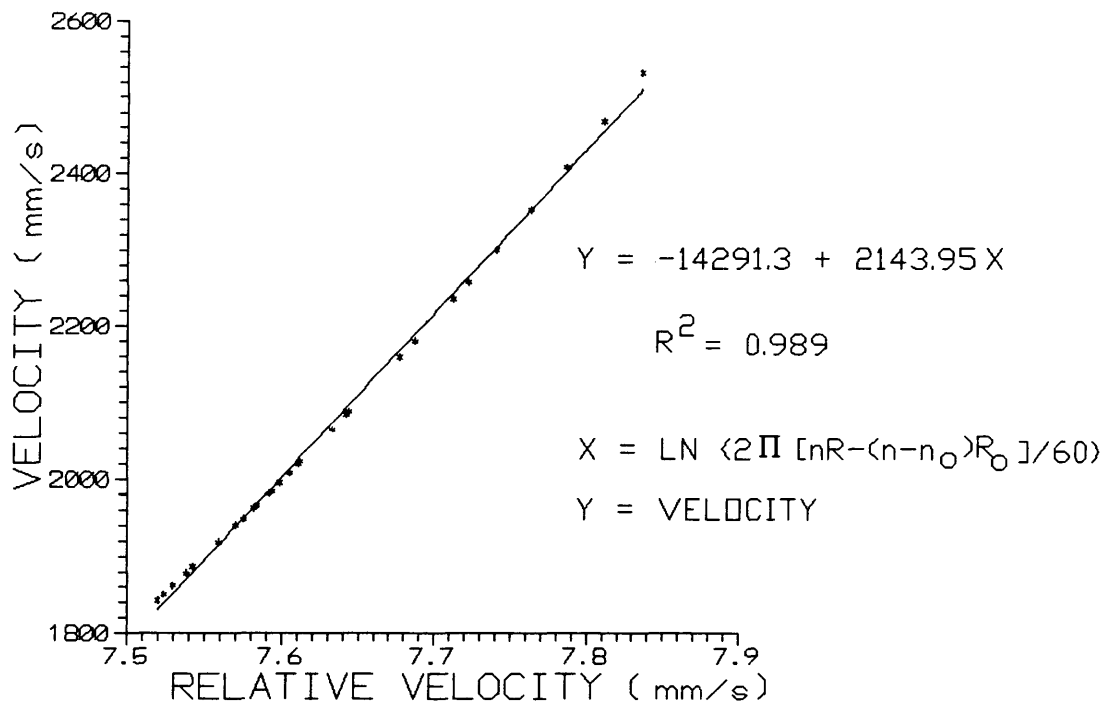


Figure 4.10b. Thread growth velocity versus relative disk tangent velocity.

4.4 Quantitative Relationships Between the Thread and the Controllable Parameters

According to dynamic similarity analysis, the fiberization process is related to Reynolds and Weber numbers, which combine the fluid properties and controllable parameters. In an attempt to correlate the experimental results, a search ensued for a relationship between each thread parameter and various combinations of the Reynolds and Weber numbers. Since the Reynolds and Weber numbers are dimensionless numbers, the thread parameters are also correlated to dimensionless numbers with a reference length scale D (rotation disk diameter). The dimensionless thread parameters are plotted versus Reynolds number only, Weber number only, their ratio and their product in log-log form, respectively in Figures 4.11-4.14. The linear correlation coefficient, R^2 , is also calculated for each plot. As mentioned previously, all data in these figures are taken from photographs using the large format camera and stroboscope system.

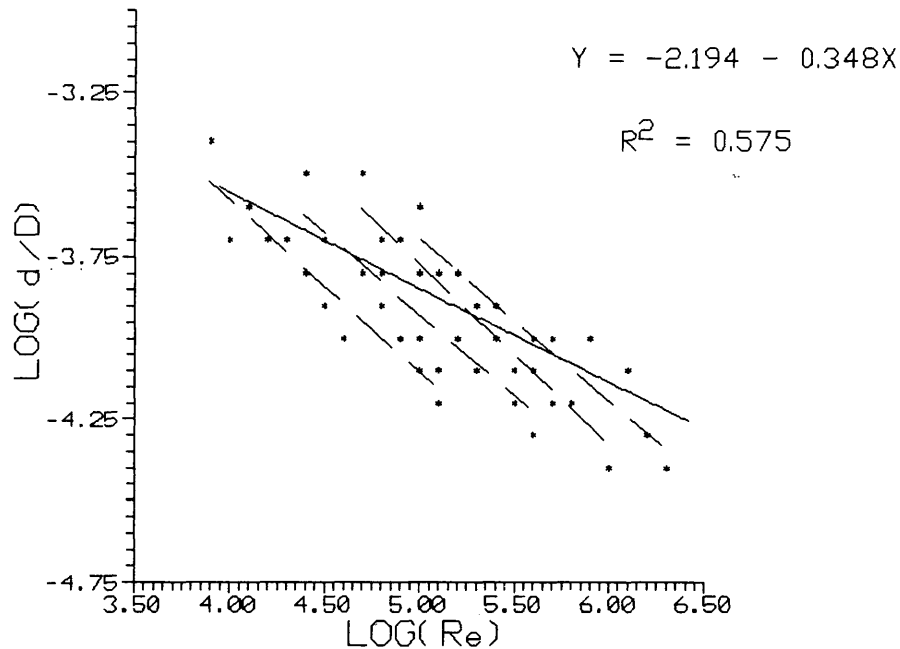


Figure 4.11. Dimensionless thread diameter versus Reynolds number only.

Note: this figure shows that there are four repeat patterns (shown in dashed lines) corresponding to different glycerine viscosities. Each pattern indicates the effect of the disk rotation speed on thread diameters. It shows that the Reynolds number depends on the liquid viscosity and the disk rotation speed equally. This means that the liquid viscosity plays the same role as that as the disk rotation speed does for changing thread diameters. This is not consistent with the observation from experimental photographs which shows that the fiber diameter is mainly controlled by the disk rotation speed as discussed in Section 4.2. Therefore, this figure cannot describe the overall relationship between the thread and the controllable parameters.

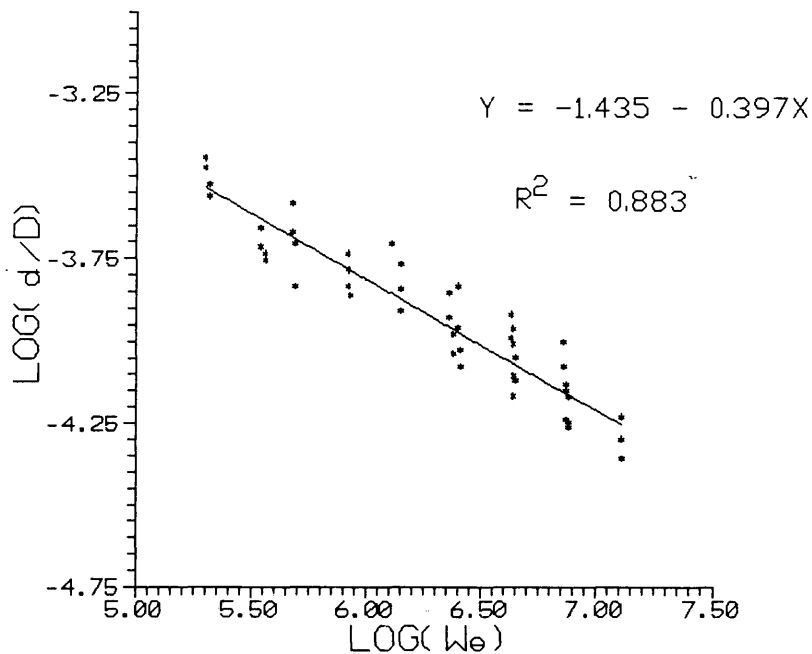


Figure 4.12. Dimensionless thread diameter versus Weber number only.

Note: this figure also shows several patterns of data points falling on vertical lines corresponding to different disk rotation speeds. The data points in each pattern represent different thread diameters resulting from glycerine at different temperatures. This means that the thread diameter does not depend on the Weber number for a constant disk rotation speed. Since the Weber number is independent to the temperature, this figure does not show how the thread diameter is affected by the glycerine temperature. In fact, measurable changes in fiber diameter were observed with changes in glycerine temperatures. Therefore, this figure cannot describe the relationship between the thread diameter and the controllable parameters.

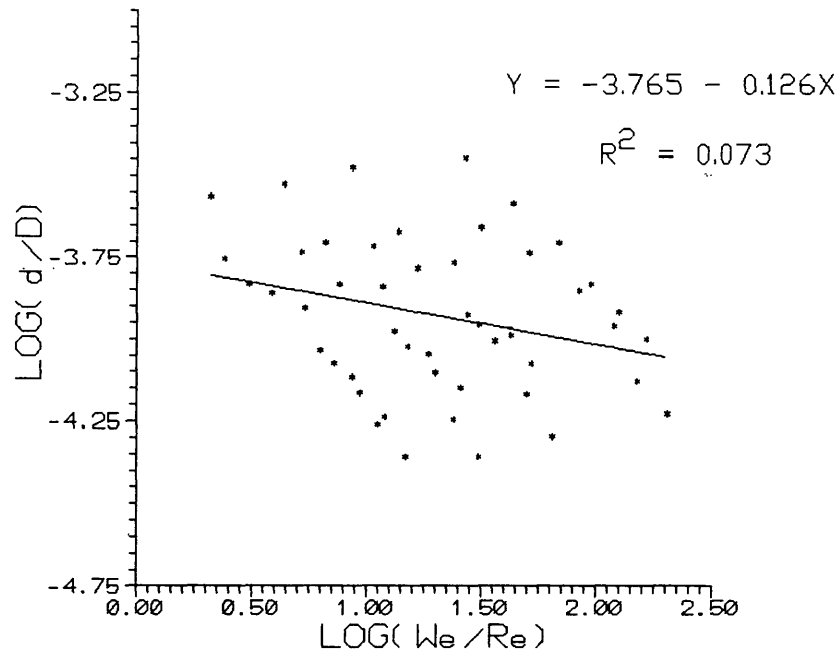


Figure 4.13. Dimensionless thread diameter versus ratio of Weber Number to Reynolds number.

Note: this figure shows that the thread diameter does not correlate very well with the ratio of the Weber number to the Reynolds number. The ratio of Weber and Reynolds numbers equals to $\pi n D \mu / \sigma$. Since the liquid surface tension is almost constant in this study, We/Re is proportional to the disk rotation speed, diameter and the liquid viscosity. This relationship indicates that three the factors play the equal roles in changing the thread diameters. This is not consistent with observations from experimental photographs which show that the fiber diameter is mainly controlled by the disk rotation speed as discussed in Section 4.2. Therefore, this figure cannot describe the relationship between the thread diameter and the controllable parameters.

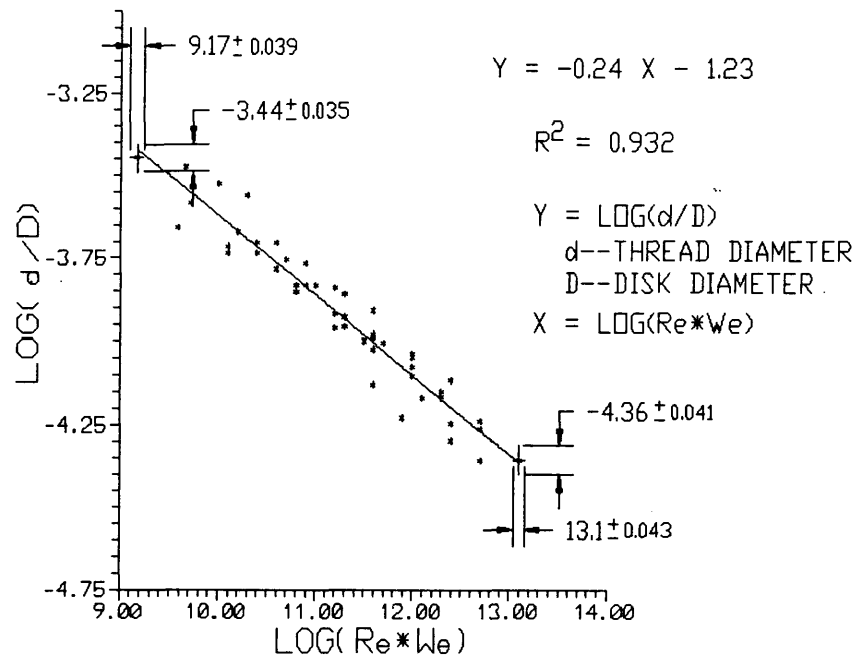


Figure 4.14. Dimensionless thread diameter versus the product of Reynolds and Weber numbers.

Note: this figure shows that the thread diameter correlates very well with the product of Reynolds and Weber numbers. The $Re*We$ equals to $\rho^2 V^3 D^2 / \mu \sigma$. Since the liquid density and surface tension are almost constant in this study, $Re*We$ is proportional to the third power of the disk tangent velocity, the second power of the disk diameter and the liquid viscosity. This relationship indicates that the disk speed plays the major role in changing the thread diameters. This is consistent with the observation from experimental photographs as discussed in section 4.2. Therefore, it is believed that this figure best describes the relationship between the thread diameter and the controllable parameters.

Comparing these four plots, the highest linear correlation coefficient was obtained for the plot of dimensionless thread diameter versus the product of Reynolds (Re) and Weber numbers (We). The results indicate that thread diameters correlate strongly to the $Re*We$ (Figure 4.14). This correlation holds for the dimensionless thread length and instability wavelength, as shown in Figures 4.15 and 4.16.

Since the experimental results for thread numbers (Z) generated by a spinning cup during atomization process obtained by Hinze and Milborn (1950) are related to the same combination of the controllable parameters as that for the $Re*We$, the results are plotted as the dimensionless wavelength of instability versus $Re*We$ in the Figure 4.16 for comparison. The dimensionless instability wavelength was calculated by π/Z based on the equation 2.1. Comparing these results with our glycerine experimental results, the slopes of two lines (best fit lines for two experiments) are close to each other while the intercepts are different due to different experimental parameters (D, n) and liquid properties (σ, μ, ρ). This indicates that the relationship between the instability wavelength and the product of Reynolds and Weber numbers obtained from this study is consistent with the previous experimental results.

Linear regression analysis of the data presented in Figures 4.14 - 4.15 indicates that both have acceptably high linear correlation coefficients, R^2 . However, that for instability wavelength is lower. A possible reason for the additional scatter in the data is the inaccuracy of 3-dimensional wavelength measurements from 2-dimensional photographs taken at high rotation speeds as discussed in section 4.3.2.

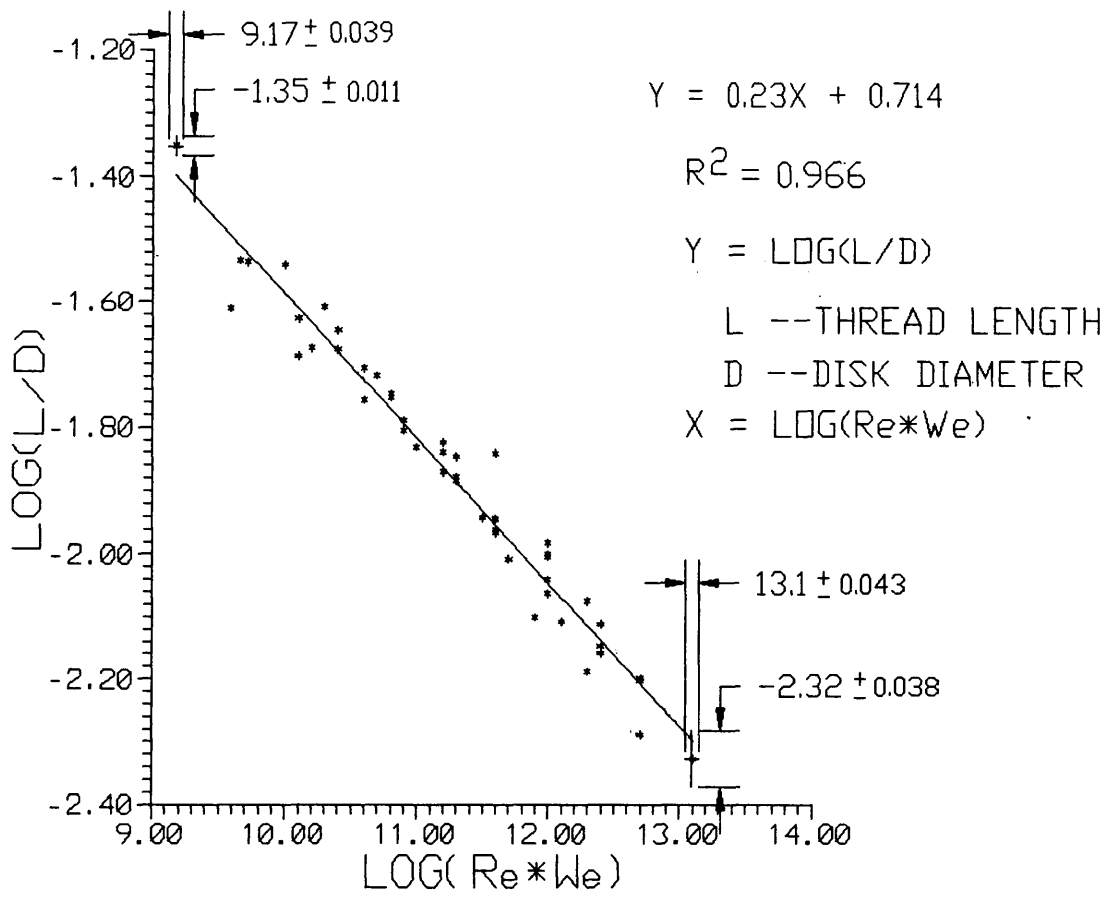


Figure 4.15. Dimensionless thread length versus the product of Reynolds and Weber numbers.

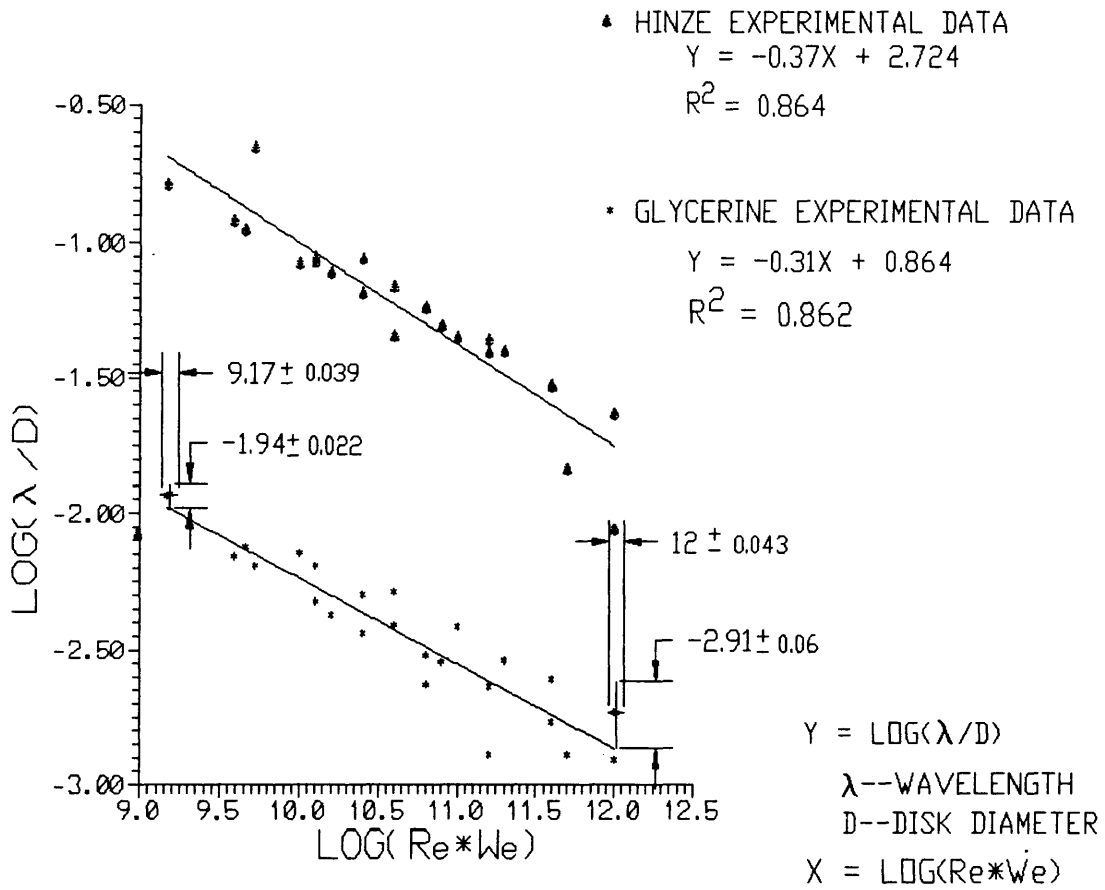


Figure 4.16. Dimensionless instability wavelength versus the product of Reynolds and Weber numbers.

The relationships between the thread parameters and $Re*We$ have been established in Figures 4.14-4.16. Since $Re*We$ is a combination of the controllable parameters, the relationships between the thread and controllable parameters are quantitatively established using a least square curve fitting routine and are expressed in equations (4.8)-(4.10).

$$\begin{aligned} \frac{d}{D} &= 0.061 (Re*We)^{-0.24} \\ &- 0.51 \left(\frac{\rho^2 n^3 D^5}{\sigma \mu} \right)^{-0.24} \end{aligned} \quad (4.8)$$

$$\begin{aligned} \frac{\lambda}{D} &= 7.34 (Re*We)^{-0.31} \\ &- 61.34 \left(\frac{\rho^2 n^3 D^5}{\sigma \mu} \right)^{-0.31} \end{aligned} \quad (4.9)$$

$$\begin{aligned} \frac{L}{D} &= 5.199 (Re*We)^{-0.23} \\ &- 43.475 \left(\frac{\rho^2 n^3 D^5}{\sigma \mu} \right)^{-0.23} \end{aligned} \quad (4.10)$$

These relationships are believed to be acceptable mathematical models for the fiber spinning process. If the dynamic similarity assumptions hold, then the industrial fiber formation process can be improved with these models. Therefore, these formulas should be useful for fiber manufacturing engineers in obtaining desired fiber characteristics by adjusting controllable parameters within the process. For example,

to reduce fiber diameter d from $4\ \mu\text{m}$ to $1\ \mu\text{m}$, the disk rotation speed should be increased from 12700 rpm to 40400 rpm for spinning conditions of refractory fibers (48 wt% Al_2O_3 and 52 wt% SiO_2) at melt temperature $T=2003\ ^\circ\text{C}$.

Also, it may be possible to make low viscosity refractory fibers using the melt spinning method based on the same product value (P) of Reynolds and Weber numbers from the experimental results. Mullite [Al_2O_3 (72 wt%), SiO_2 (28 wt%)] may be made by matching the same P value of existing environment of spinning process. For example, the P value for a refractory material with composition of Al_2O_3 (48 wt%) and SiO_2 (52 wt%) is $4.3\text{E}+12$ at Schuller Corporation at Denver. The rotation speed of disk should be reduced to about 7500 rpm in order to match P value and obtain the same fiber diameter ($d=4\ \mu\text{m}$) as that of the existing material. The comparison is shown in Table 4.7. Fiber properties listed in the table are properties of the liquid melt at $T=2003\ ^\circ\text{C}$. Transport property data are given by Bansal and Doremus (1986).

**Table 4.7. Disk Rotation Speed Comparison for
Different Composition Fibers with Same
Fiber Diameter and Re*We Value**

Al ₂ O ₃ (wt%)	SiO ₂ (wt%)	μ (N-s/m ²)	ρ (kg/m ³)	σ (N/m)	n (rpm)
48	52	0.48	2900	0.419	12700
72	28	0.12	3300	0.445	7523

4.5 Physical Meaning of Mathematical Models

This section presents the explanation of physical meaning of mathematical models and a comparison with previous work. The driving and resistance forces for fiber formation and growth are also discussed.

From the experimental results shown in Figure 4.14 through 4.16, it is seen that the thread diameter d and length L are nearly proportional to the instability wavelength λ . Figure 4.17 illustrates the relationship between the thread diameter and the instability wavelength. Clearly, there is a linear relationship between them. The instability wavelength is equal to

$$\lambda = \frac{2\pi}{K} \quad (4.11)$$

where K is the wave number of the wavelike perturbations. Eisenklam (1964) gave an expression of K for a rotating cup under the combined action of viscosity and surface tension as:

$$K \propto A \left[\frac{\rho}{\sigma} \left(\frac{\omega^2 D}{2} \right) \right]^{\frac{1}{2}} \quad (4.12)$$

where A is a coefficient related to viscosity, and decreases as viscosity increases.

The wave number K increases with increasing density ρ and disk angular acceleration, $\omega^2 D/2$. K decreases with increasing viscosity μ and surface tension σ . On the other hand, increasing the density and disk angular acceleration results in increasing the centrifugal force while increasing μ and σ results in increasing viscous and surface forces. Therefore, the wave number K increases with increasing centrifugal force and decreases with increasing viscous and surface forces.

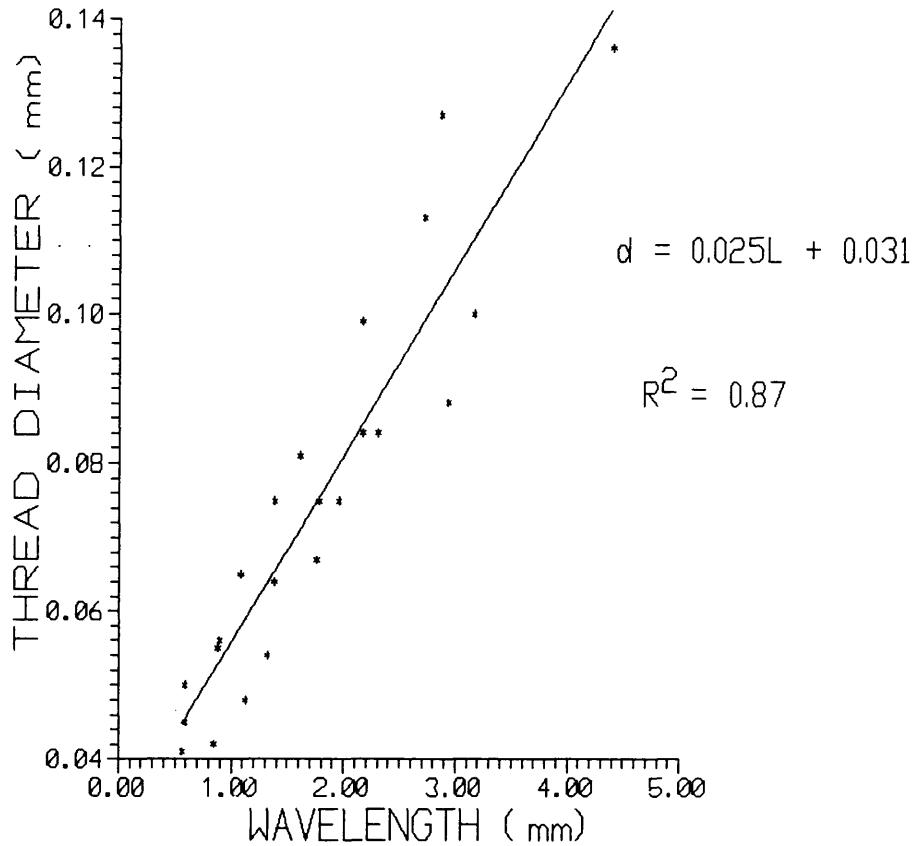


Figure 4.17. Relationship between thread diameter and instability wavelength.

Since d , L and λ are inversely proportional to K , they decrease with the increasing density ρ and acceleration, $\omega^2 D/2$, and increase with the increasing viscosity μ and surface tension σ . Therefore, the experimental results of this study are consistent with these previously determined relationships.

The growth rate of the instability depends on the wave number K and can be

expressed as $\delta=(aK)^{1/2}$ for a fluid with a constant acceleration, a (Kull, 1991). A large K value results in an increased growth rate of the RT instability and a larger number of thinner fibers. Since increasing the centrifugal force increases the K value (corresponding to increasing the instability growth rate, δ), the centrifugal force is the driving force of the fiber formation. On the other hand, since increasing viscous and surface tension forces decreases K value (corresponding to decreasing the instability growth rate), the viscous and the surface forces resist the fiber formation. Since the aerodynamic drag is a resistance force to the centrifugal force, it is also a resistance force to the fiber formation.

4.6 Estimation of the Effective Mass Flow Rate

The relationship between the fiber growth velocity and disk rotation speed as well as the correlations for fiber diameter, length and wavelength of the instability were used to estimate the effective mass flow rate for a given disk rotation speed. It was found that the total volumetric flow rate, Q_{Tr} , depends on the disk rotation speed, and the ratio of the mass of fibers produced to the mass of melt incident on the disk.

The total mass flow rate (\dot{m}_T) is equal to the product of total volume flow rate and the density. Since density does not change very much for given compositions of materials, the fiber mass flow rate, \dot{m}_T , depends directly on Q_{Tr} . The Q_{Tr} is equal to

$$Q_{Tf} = \frac{\pi d^2}{4} VZ \quad (4.13)$$

Where the fiber diameter (d) is calculated using equation 4.8 for each disk rotation speed (n). The number of fibers generated for each n is inversely proportional to the instability wavelength (λ) while λ is calculated using equation 4.9. The fiber growth velocity (V) is calculated by equation 4.7 in which a variable L (fiber length) is calculated by equation 4.10. Based on the above calculated data, the fraction of Q_{Tf} to the incident flow rate Q_m is also evaluated, and plotted in Figure 4.18 with respect to the disk rotation speed. All calculated results are presented in Table 4.8. All properties of glycerine are at a temperature 25 °C.

In addition to the mass flow rate calculation, the Reynolds numbers based on fiber diameter and speed for the fiber growth were calculated for each disk rotation speed, and are also listed in Table 4.8. The Reynolds number decreases as the fiber is thinned and elongated. The range of the Reynolds number is between 0.3 and 2.5 for $n=90$ -- 920 rpm.

Table 4.8. Calculation of Fraction of Effective Flow Rate to the Incident Flow Rate

n (rpm)	90	150	260	400	670	920
d (mm)	0.302	0.209	0.141	0.103	0.071	0.057
L (mm)	31.96	22.46	15.37	11.42	8.00	6.43
λ (mm)	10.74	6.68	4.00	2.68	1.66	1.24
V (mm/s)	925.9	1099.1	1313.1	1502.6	1757.5	1930.3
Fiber growth Reynolds number	2.54	1.48	0.35	0.34	0.27	0.79
Q_r (GPM)	1.8E-5	10.0E-6	5.4E-6	3.3E-6	1.9E-6	1.3E-6
# Rows	4.4	7.0	11.7	17.5	28.3	38.0
# Columns	111.5	179.2	299.0	446.3	721.0	968.3
Z	488	1262	3509	7920	20411	36815
Q_{Tr} (GPM)	0.009	0.013	0.019	0.026	0.038	0.047
Q_m (GPM)	0.2	0.2	0.2	0.2	0.2	0.2
Q_{Tr}/Q_m (%)	4.3	6.3	9.5	13.0	19.0	24.0

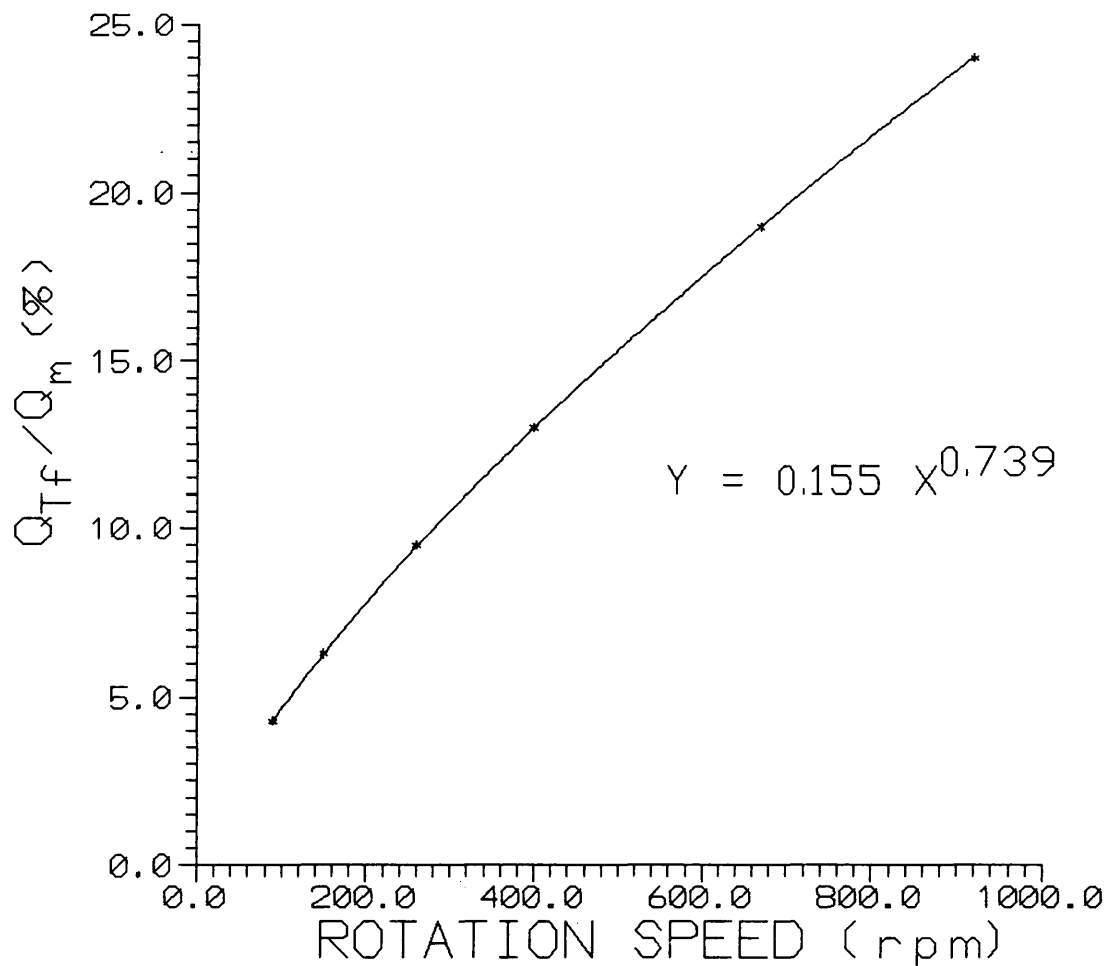


Figure 4.18. Fraction of effective fiber flow rate to the incident flow rate versus disk rotation speed.

CHAPTER 5

THEORETICAL ANALYSIS AND COMPUTER MODELING

This chapter presents the theoretical analysis and computer modeling performed to help understand the fiber formation by the spinning process. The governing equations for the three stages of fiber formation are introduced first. The numerical modeling results and limitations are then discussed.

5.1 Governing Equations of Three Stages of Fiber Formation

5.1.1 Governing Equations for Perturbation Forming due to Rayleigh Taylor Instability

As mentioned previously, perturbations form and grow due to the Rayleigh-Taylor instability in the first stage of the fiberizing process. The RT instability is driven by the centrifugal force in the radial direction of the disk. Since the flow is assumed to be independent of the disk axial direction, we need only consider two-dimensional perturbations periodic along the outer circumference of disk. Therefore, the coordinate system is set up relative to the disk rotating system and in a plane perpendicular to the disk rotation axis. The x and y axes have an origin at the outer surface of the disk and are oriented in the tangential and normal directions as shown in Figure 2.2. Each individual fiber is subjected to the following forces: centrifugal

force, gravitational force, viscous force, surface force, and air drag.

According to Newhouse (1991), the RT instability principle is classified as linear and nonlinear theories based on the behavior of perturbations. Linear instability theory predicts whether an infinitesimally small sinusoidal perturbation of the position of the layer surface will initially grow or decay in time, the rate of growth or decay, and the wavelength of the fast growing perturbation. Linear theory was used in this study for calculating the instability growth rate at the initial conditions. Nonlinear instability theory predicts the long time behavior of a disturbance when perturbations grow, and can be applied to entire formation process of ordered structures from the initial state to final state. Since the whole fiber formation process represents the longtime behavior of disturbances and the nonlinear interactions between liquid and gas continuously occur, nonlinear theory is selected for solving the whole process in this study. This theory is categorized into inviscid and viscous flows, depending on the Reynolds number of the flow. The nonlinear viscous flow model deals with the instability at conditions of creeping motion, and is applied to single or multiple liquid layers resting on a horizontal plane. For stage 1 of the fiber formation process, the Reynolds number of fiber growth is very low in the range of between 0.3 and 2.5 according to the results shown in Section 4.6, and the liquid layer rests on the outer surface of the disk. The viscous flow model of nonlinear instability theory will apply to this stage. The following assumptions are made to derive the governing equation for stage 1.

1. There is no slip at the interface between the liquid layer and disk circular surface.
2. Two fluids are considered as incompressible fluids.
3. The gravitational force and air drag are negligible compared to the centrifugal force due to high rotation speeds, and the centrifugal force is considered as the body force.
4. The interface between liquid and air is a plane $y=0$. The initial perturbation motion along this surface is a sinusoidal wave with a small amplitude compared to the wavelength (Bellman,1954) by taking the stream function (ψ) and potential function (ϕ) as:

$$\psi = A e^{(-Ky + \delta r)} \cos(Kx) \qquad \phi = B e^{(-my + \delta r)} \sin(Kx)$$

5. The mass flow rate of liquid (\dot{m}) is constant for a given disk rotation speed, diameter, and physical properties of fluids. The fiber mass flow rate, \dot{m} , depends on volume flow rate Q while Q depends on the liquid layer thickness. The liquid thickness is constant for given n , D , and fluid properties. Therefore, the continuity equation is satisfied.
6. The Reynolds number of fiber growth is negligible due to higher viscosity and lower fiber growth velocity at the first stage. Therefore, the advective terms in the Navier-Stokes equations are also negligible.

Based on the above assumptions, the RT instability due to the centrifugal force, with the effects of both viscosity and surface tension, is modeled by the following

continuity and Navier-Stokes equations

$$\begin{aligned}
 \frac{\partial U}{\partial x} + \frac{\partial V}{\partial y} &= 0 \\
 \frac{\partial U}{\partial \tau} + \frac{1}{\rho} \frac{\partial p}{\partial x} - \nu \left(\frac{\partial^2 U}{\partial x^2} + \frac{\partial^2 U}{\partial y^2} \right) & \\
 \frac{\partial V}{\partial \tau} + \frac{1}{\rho} \frac{\partial p}{\partial y} + \omega^2 R - \nu \left(\frac{\partial^2 V}{\partial x^2} + \frac{\partial^2 V}{\partial y^2} \right) &
 \end{aligned} \tag{5.1}$$

Since the surface forces appear at the interface between a liquid and a gas, they do not appear directly in the equations of motion, but enter only in the boundary conditions. The boundary conditions at the free surface (interface between liquid and air) are:

$$\begin{aligned}
 U_1 &= U_2; \quad V_1 = V_2 \\
 p_1 - 2\mu_1 \frac{\partial V_1}{\partial y} &= p_2 + 2\mu_2 \frac{\partial V_2}{\partial y} - \sigma \frac{\partial^2 \eta}{\partial x^2} = 0 \\
 \mu_1 \left(\frac{\partial V_1}{\partial x} + \frac{\partial U_1}{\partial y} \right) &= \mu_2 \left(\frac{\partial V_2}{\partial x} + \frac{\partial U_2}{\partial y} \right)
 \end{aligned} \tag{5.2}$$

where η is the displacement of the free surface and can be expressed as (Bellman and Pennington, 1954) :

$$\eta = K(A+B)\delta^{-1}e^{\delta\tau} \cos(kx)$$

δ is the growth rate of RT instability and is related to the frequency ω and the wavenumber K of perturbations. According to the linear instability theory, if δ is negative, the system is stable. On the other hand, if δ is positive, the system is

unstable, and the RT instability occurs. The δ expression was derived by solving equation (5.1) using the boundary conditions (5.2) and the expression of η at $\tau=0$.

Bellman and Pennington (1954) yields an expression about δ as

$$[-a(\rho_2 - \rho_1)K + \sigma k^3 + (\rho_1 + \rho_2)\delta^2] \left[\frac{1}{\mu_1 K + (\mu_2^2 K^2 + \mu_2 \rho_2 \delta)^{1/2}} + \frac{1}{\mu_2 K + (\mu_1^2 K^2 + \mu_1 \rho_1 \delta)^{1/2}} \right] + 4\delta K - 0$$

δ values are calculated using the above expression for different disk rotation speeds and liquid viscosities corresponding to the fiber spinning system as shown in Table 5.1. Results show that all δ values are positive. As expected, the system is unstable and RT instability occurred at these speeds, which is verified by the experimental results and industrial observations.

Table 5.1. Calculation of Instability Growth Rates

viscosity μ (N-s/m ²)	δ (s ⁻¹) at different disk rotation speed n (rpm)					
	260	400	670	920	1200	1560
0.36	126.9	211.1	379.1	537.6	714.9	950.6
0.108	213.4	382.6	756.6	1140.4	1595.7	2225.1
0.051	250.2	461.2	948.1	1468.1	2105.8	3012.2
0.025	273.5	512.6	1078.9	1699.3	2475.7	3599.8

These results also indicate that the instability growth rate increases with increasing rotation speed and decreases with increasing viscosity, which again verifies that the centrifugal force is a driving force of RT instability growth and the surface tension force and viscous force are resistance forces to the instability growth.

Linear instability theory can only predict that the RT instability will occur at given operation conditions of fiberization process, but cannot be used to analytically solve the transient two-dimensional governing equations (5.1). Equations (5.1) have to be solved using numerical methods.

5.1.2 Governing Equations for Free Surface Flow

As the perturbation grows, liquid threads are thinned and stretched. As the fiberization process reaches stage 2, it can be treated as a free surface flow in the form of a two-dimensional jet. The conservation of mass and momentum equations for the free surface flow under the effects of surface tension, viscosity, and air drag are expressed as:

$$\begin{aligned} \frac{\partial U}{\partial x} + \frac{\partial V}{\partial y} &= 0 \\ \frac{\partial U}{\partial \tau} + U \frac{\partial U}{\partial x} + V \frac{\partial U}{\partial y} + \frac{1}{\rho} \frac{\partial p}{\partial x} &= \nu \left(\frac{\partial^2 U}{\partial x^2} + \frac{\partial^2 U}{\partial y^2} \right) \\ \frac{\partial V}{\partial \tau} + U \frac{\partial V}{\partial x} + V \frac{\partial V}{\partial y} + \frac{1}{\rho} \frac{\partial p}{\partial y} + \omega^2 R &= \nu \left(\frac{\partial^2 V}{\partial x^2} + \frac{\partial^2 V}{\partial y^2} \right) \end{aligned} \quad (5.4)$$

Since the free surface moves in both x and y directions, the velocity components in the two directions are both functions of x and y. Thus, the nonlinear advective terms are included in the equations (5.3). Boundary conditions at the free surface are:

$$\begin{aligned} -\frac{\partial p}{\partial x} + \mu_1 \left(\frac{\partial^2 U}{\partial x^2} + \frac{\partial^2 U}{\partial y^2} \right) &= -\frac{2\sigma}{dx} - \frac{\rho C_x [\omega(R+y) - V_2]}{dy} \\ -\frac{\partial p}{\partial y} + \mu_1 \left(\frac{\partial^2 V}{\partial x^2} + \frac{\partial^2 V}{\partial y^2} \right) &= -\frac{\sigma}{dy} + \omega^2(R+y) \end{aligned} \quad (5.5)$$

where the air resistance in the y-direction is ignored. V_2 is the velocity of the surrounding air along the x-direction, which is expressed as follows (Schlichting, 1968):

$$V_2 = \frac{R}{R+y} \omega R \left[1 - \exp\left(-\frac{(R+y)^2}{4} \nu \tau\right) \right] \quad (5.6)$$

μ_1 is the temperature dependent viscosity of the refractory materials, which can be obtained from the following equation (Paek and Schroeder, 1988):

$$\mu_1 = B \exp\left(\frac{E}{R_0 T}\right) \quad (5.7)$$

As the fiber is elongated and thinned, it is rapidly cooled by convective and radiative heat transfer to the surroundings. As stated earlier, the temperature of the fiber has a decisive effect at this stage of fiber formation, which represents the effect of the melt viscosity. Hence, the energy equation (5.8) developed by Westerlund and Hoikka (1989) for this process is introduced for studying the temperature distribution along fiber length.

$$\frac{\partial T_f}{\partial \tau} = \frac{\Lambda}{\rho C_v} \frac{\partial^2 T_f}{\partial y^2} - \frac{C_p v}{C_v} \frac{\partial T_f}{\partial y} - \frac{4}{d \rho C_v} [h(T_f - T_a) + \epsilon_1 \sigma_o (T_f^4 - T_a^4) + \epsilon_2 \sigma_o (T_f^4 - T_m^4)] \quad (5.8)$$

This is a nonlinear second-order partial differential equation, which describes the temperature of the fiber in time and space. This equation and its initial and boundary conditions shown in equation (5.9) can be solved numerically.

$$T_f(y=0) = T_0$$

$$-\Lambda \frac{\partial T_f}{\partial y} = [h + \sigma_o ((T_f^2 + T_a^2)(T_f + T_a))](T_f - T_a) \quad (5.9)$$

The modeling results provided by Westerlund and Hoikka (1989) show that the temperature gradient along fiber length varies dramatically as illustrated in Figure 5.1. The temperature distribution was plotted as a function of both the fiber length

(s) and the time (t) in the figure. The fiber at 1400 °C when it was out of the disk edge was cooled to the room temperature when the fiber length was elongated to 0.1 meters. The cooling rate of fiber depended on several factors such as fiber diameter, length, growth rate, heat transfer coefficients between the fiber and air, and the environment temperature.

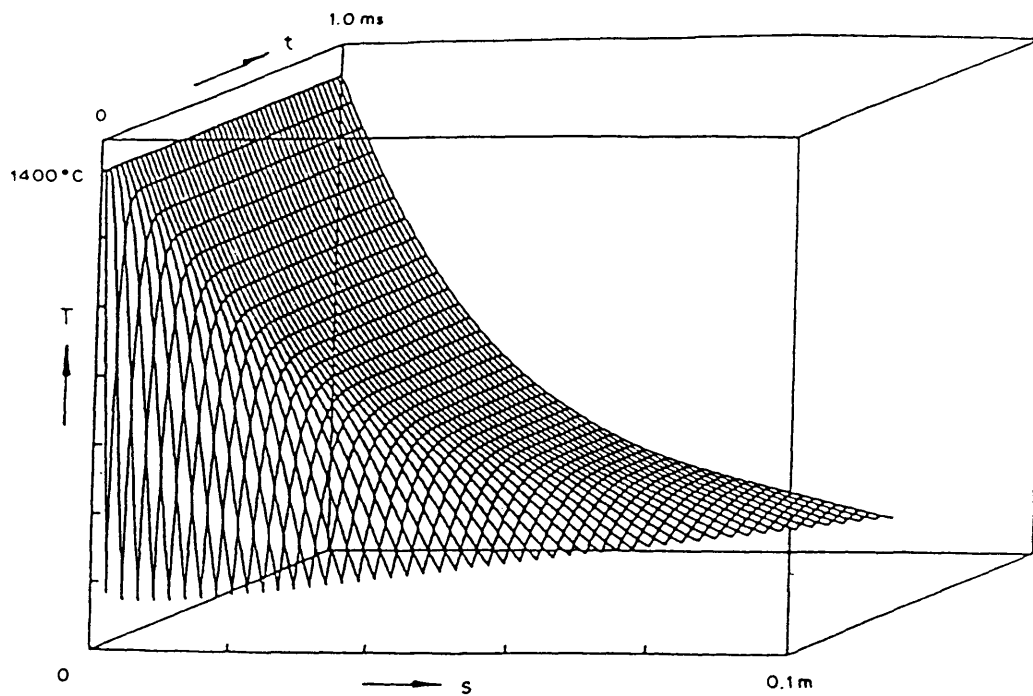


Figure 5.1. Temperature distribution along fiber length (Westerlund and Hoikka, 1989)

5.1.3 Break-up Mechanism of a Fiber by Air Drag

Presumably the fiber finally breaks free from the disk by the centrifugal and air drag forces. The break-up mechanism is different in two directions. In the axial direction of the fiber, the fiber is broken by tensile stress, where the centrifugal force and the air drag exceeds the resistive viscous and surface forces. An empirical integral drag coefficient expression for cylinders given by Glicksman (1968) is used to calculate the air drag D_y in this direction.

$$\begin{aligned}
 C_y &= 0.4 \left[\frac{V_{2y} d}{2v_2} \right]^{-0.7} \\
 D_y &= \int_0^L \frac{1}{2} \rho_2 d V_{2y}^2 C_y dy \\
 &= 0.325 \frac{\rho_2 d^{-0.3}}{v_2^{-0.7}} \int_0^y V_{2y}^{0.3} dy
 \end{aligned} \tag{5.10}$$

In the transverse direction of the fiber, the fiber is broken by the bending stress caused by the transverse air drag at some point where the fiber has solidified. In this case, air flowing over a fiber is similar to the cross flow over a circular cylinder.

The transverse air drag D_x per unit length is calculated by

$$D_x = C_x \frac{1}{2} \rho V_{2x}^2 d \tag{5.11}$$

where the velocity V_x is taken as the velocity profile of the flow outside a cylinder (disk) rotating in an infinite fluid, and expressed as equation (5.5). It is a function of fiber length and generating time. C_x is the transverse air drag coefficient, and calculated by the following empirical expression (Westerlund, 1989):

$$C_x = 1.018 + 1.458 Re^{-0.50} + 8.151 Re^{-0.8}$$

Where Re is the Reynolds number of air in the transverse direction, and is taken as $Re = V_x d / \nu_a$. Therefore, the bending stress at outer surface of fiber is calculated by

$$\zeta = \frac{16\rho}{\pi d^2} \int_{L_0}^L [1.018 V_x^2 + 1.458 \left(\frac{d}{\nu}\right)^{-0.5} V_x^{1.5} + 8.151 V_x^{1.2}] dy$$

where L_0 is some point along fiber length where the fiber is solidified. The combination of the tensile and bending stress breaks the fiber.

5.2 Numerical Modeling by the Finite Element Method

The experimental results at high disk speeds are limited by the spatial resolution and magnification of the camera experimental device. Analytical or numerical solutions are needed to extend the model to high speed while modeling the realistic fiber formation process. However, the governing equations for both the RT instability and free surface flows for this process are nonlinear, two dimensional and transient equations, and are difficult to solve analytically in a timely fashion. Therefore, FIDAP, a fluid dynamic analysis package using the finite element method

was used to obtain the numerical solution for the free surface flow and RT instability growth of the fiber formation process.

As mentioned in Chapter 2, the basic approach of FIDAP to the free surface problem is Eulerian in which the coordinate system remains stationary while allowing the boundary nodes to move such that they remain on the moving boundary. Since the location and shape of the free surface are unknown, it is necessary to specify additional boundary conditions for problem closure. For an interface between a liquid and a gas, with the gas being treated as an effective vacuum, the boundary conditions require that a new degree of freedom be introduced at each node on the interface and the stress is continuous (FDI, 1993). The constant surface tension boundary conditions can be expressed as

$$\frac{\partial S}{\partial \tau} + u_j S_{,j} = 0 \quad \text{on } \Gamma$$

$$\zeta_i = (2 \sigma H - P_a) n_i \quad \text{on } \Gamma$$

where S is the interface, H is the mean curvature of the surface, and n_i is the normal direction of axes.

5.2.1. Numerical Model Set up

The glycerine experimental model at $D=0.381$ m, $n=260$ rpm and $T=25$ °C, was the first to be modeled numerically, followed by the realistic fiber formation process. The first two stages of the fiberization process were modeled separately.

The first stage model was developed to predict the onset of the RT instability. From the experimental work the expectation was to see waves form at the edge of the disk. The free surface flow, designated as stage two, was introduced after the waves had already formed. The expectation for this stage was to see the thread shape similar to that seen in the experimental photographs.

For both models, the interface between glycerine and air was the free surface boundary. The ambient environment was treated as an effective vacuum. The computation domain was restricted to the liquid phase (glycerine). The disk outer surface was considered to be a solid (no slip) boundary. The liquid layer thickness was calculated according to definition of air boundary layer thickness, Δ_{997} , which is the distance from the disk outer surface to where the tangent velocity of liquid reaches 99.7% of the tangent velocity of the disk in the disk radial direction. The liquid tangent velocity is also taken as the velocity profile (V_x) of the flow outside a disk rotating in an infinite fluid at the beginning of the process, then the liquid layer thickness is:

$$V_x = \frac{\omega R^2}{R + \Delta_{997}} = 0.997 V = 0.997 \omega R$$

$$\Delta_{997} = 0.003 R$$

For a disk diameter of 0.381 m and a rotation speed of 260 rpm, $\Delta_{997}=0.5$ mm was calculated from the above equation for both models. This value was consistent with the experimental measurements. A 2.5 degree liquid layer and disk arc was modeled. The geometry of RT instability model is shown in Figure 5.2.

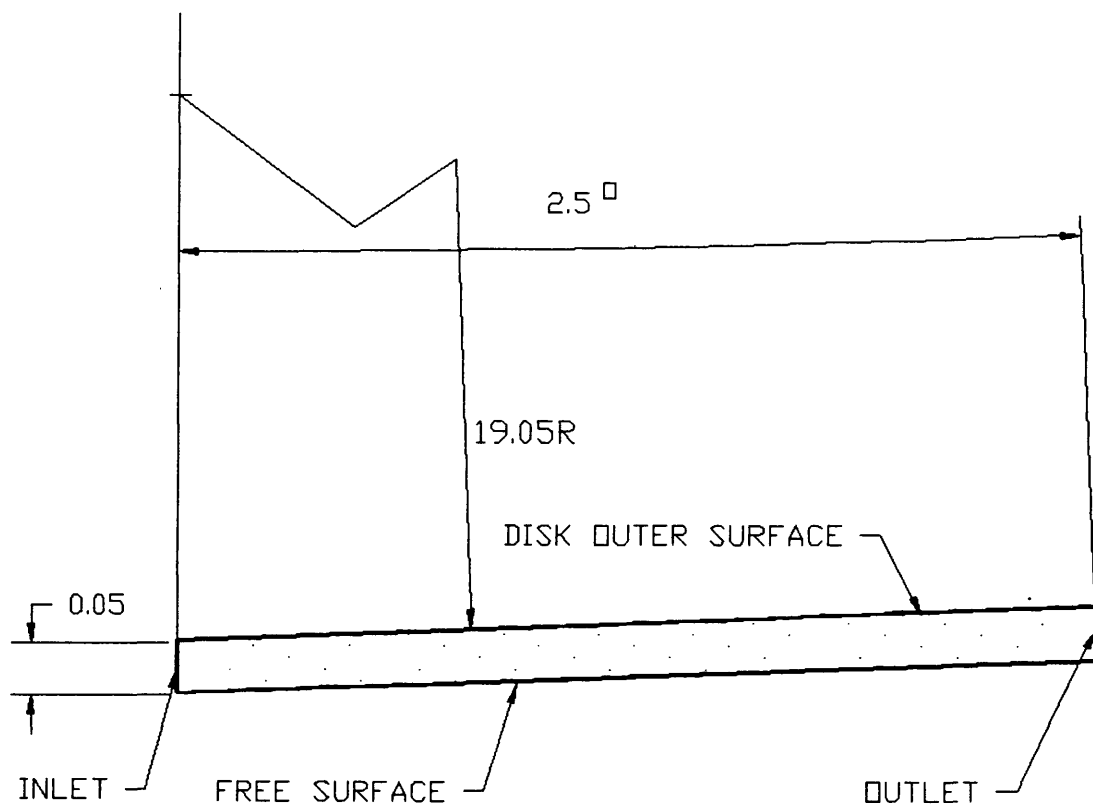


Figure 5.2. Geometry of the RT instability model

For the free surface model, a sinusoidal wave was assumed to form on the free surface. The wave length and amplitude were determined from the experimental photographs as shown in Figure 5.3. All dimensions in both figures are in centimeters.

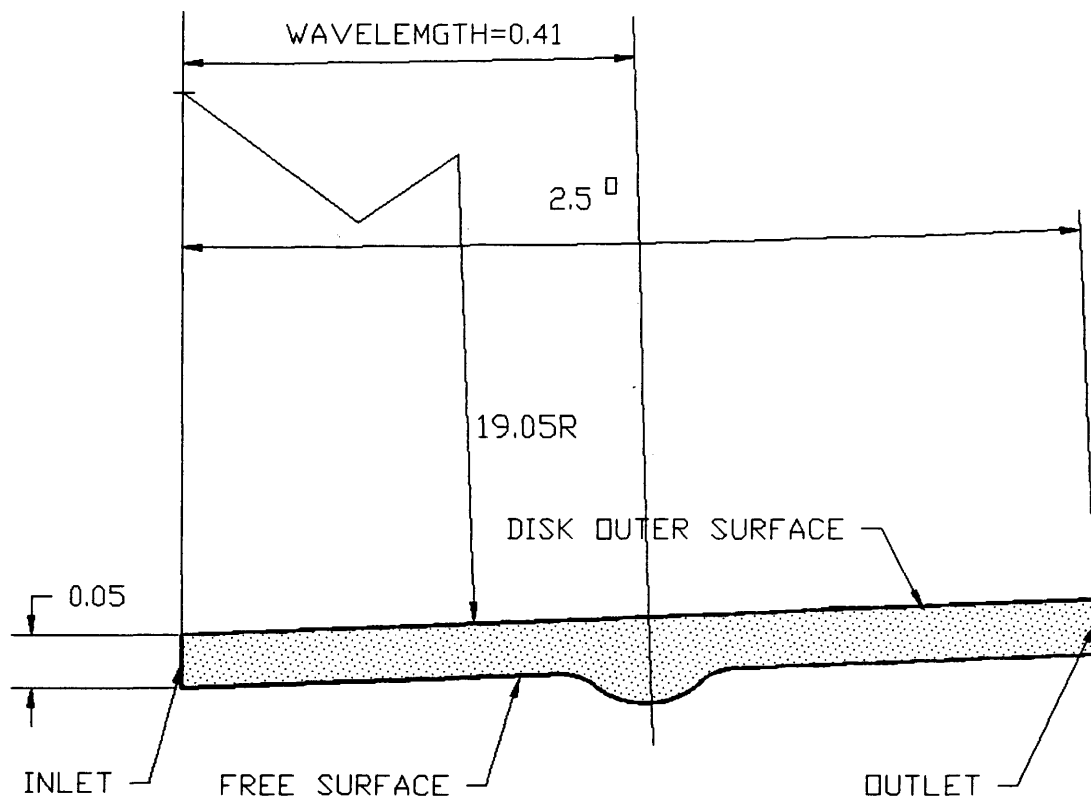


Figure 5.3. Geometry of the Free surface flow model

5.2.2. Numerical Modeling Results

Both models were meshed using the map mesh command in FIDAP, which is required for the free surface problems. Each element was a rectangular shape using this method. Similar physical properties of glycerine at $T=25$ °C were input for both models, but the initial and boundary conditions were different for each model. Several combinations of the initial and boundary conditions were tested in both models. Only a one combination of the boundary condition for each model is presented here.

The RT instability model has 864 elements and 793 nodes as shown in Figure 5.4. Since the RT instability generation was expected to be observed from this model, the initial condition was that the velocity was zero at every node. The centrifugal force ($m\omega^2R$) was considered to be the body force, and was input as force per unit volume. The input and output velocities and the gas pressure near the free surface were set to zero. The time step interval was 5×10^{-6} seconds. The input data are listed in Appendix B.

The Quasi-Newton iteration method was used to obtain the nonlinear solutions of unknowns for this model. The position of the nodes on the free surface and the field variables such as velocity and pressure at the new nodal positions were calculated simultaneously after convergence was attained. The solution converged until the running time equaled 5.6×10^{-4} seconds, and then it began to diverge.

With the above input conditions, the modeling results using the FIDAP program

for this model were unexpected. Figure 5.5 illustrates the free surface profile from the beginning to the final convergent time step. No perturbation waves are observed at the time when the solution began to diverge. Figures 5.6a-c are the mesh histories for this same run. Note that some elements are deformed dramatically at the final converged step.

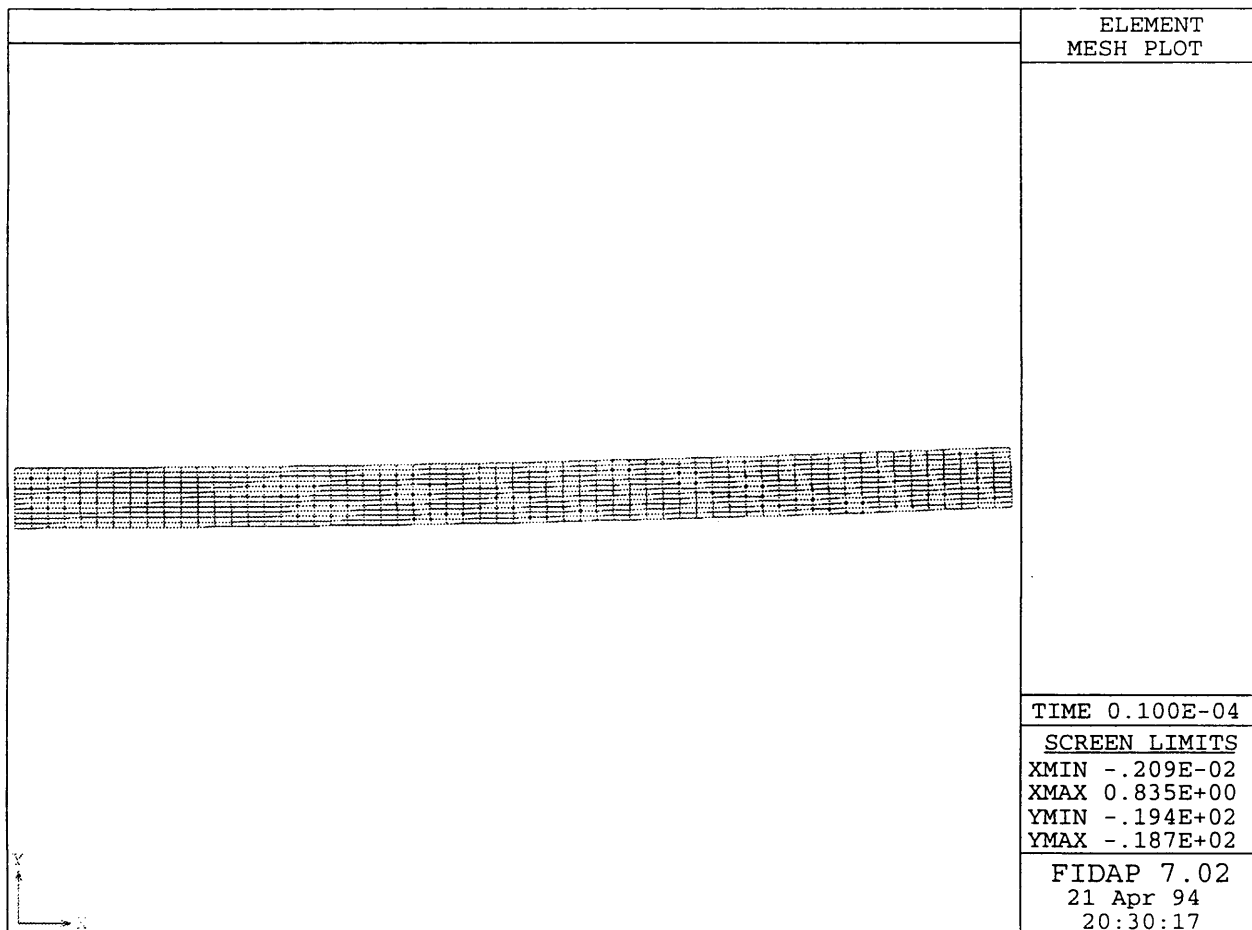


Figure 5.4. Geometry mesh of the RT instability model

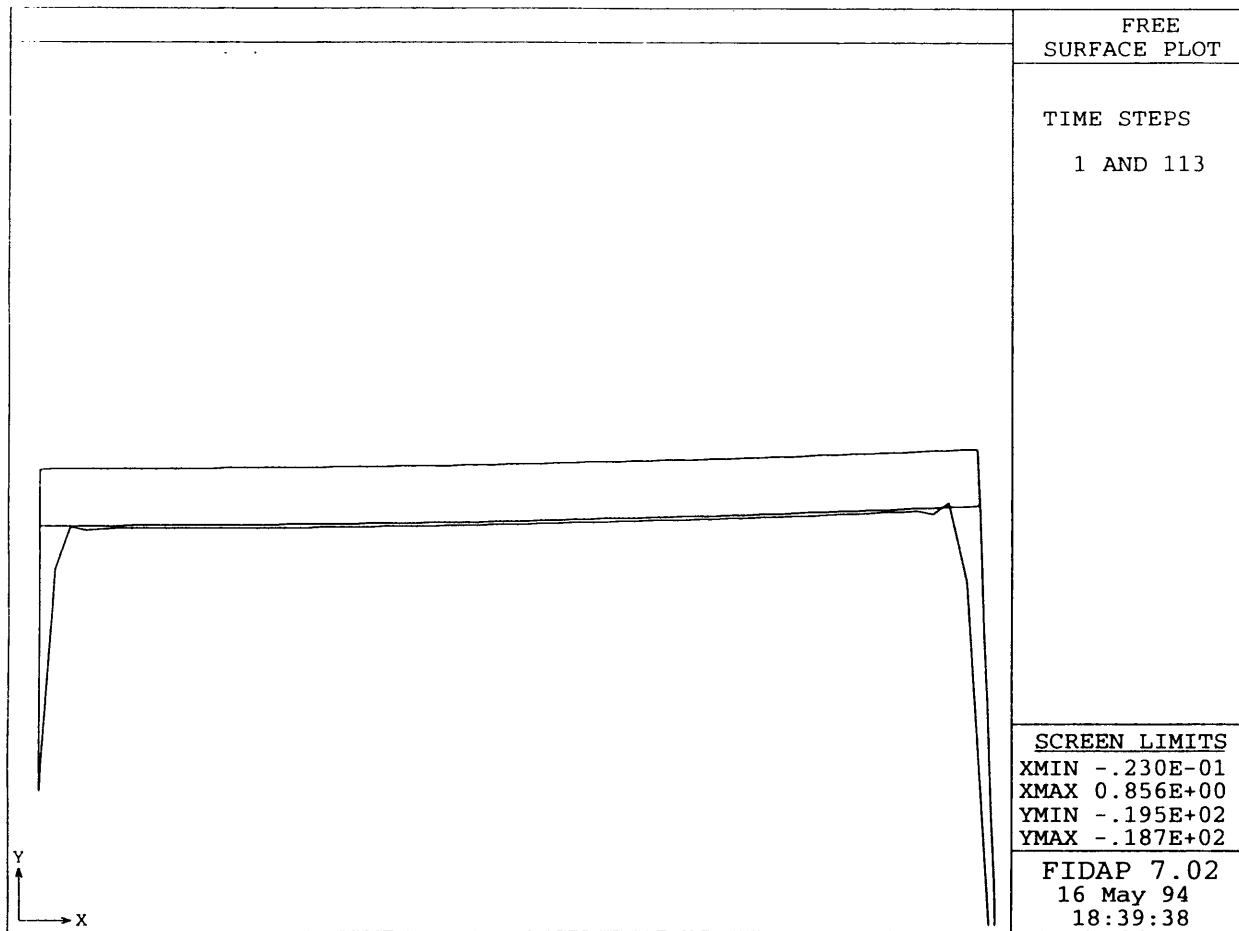


Figure 5.5. Free surface profile of the RT instability model at running time equaled 5.6×10^{-4} seconds.

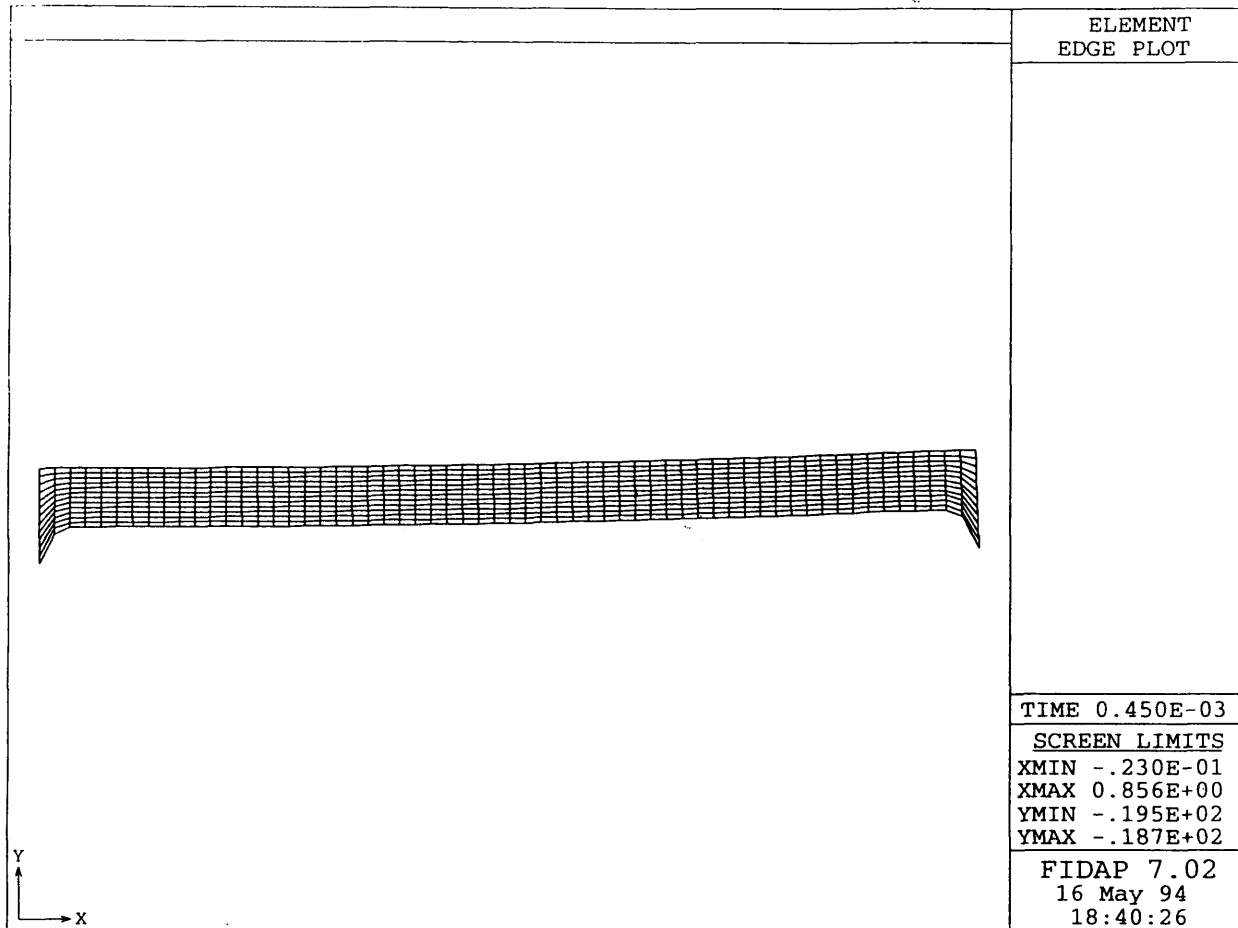
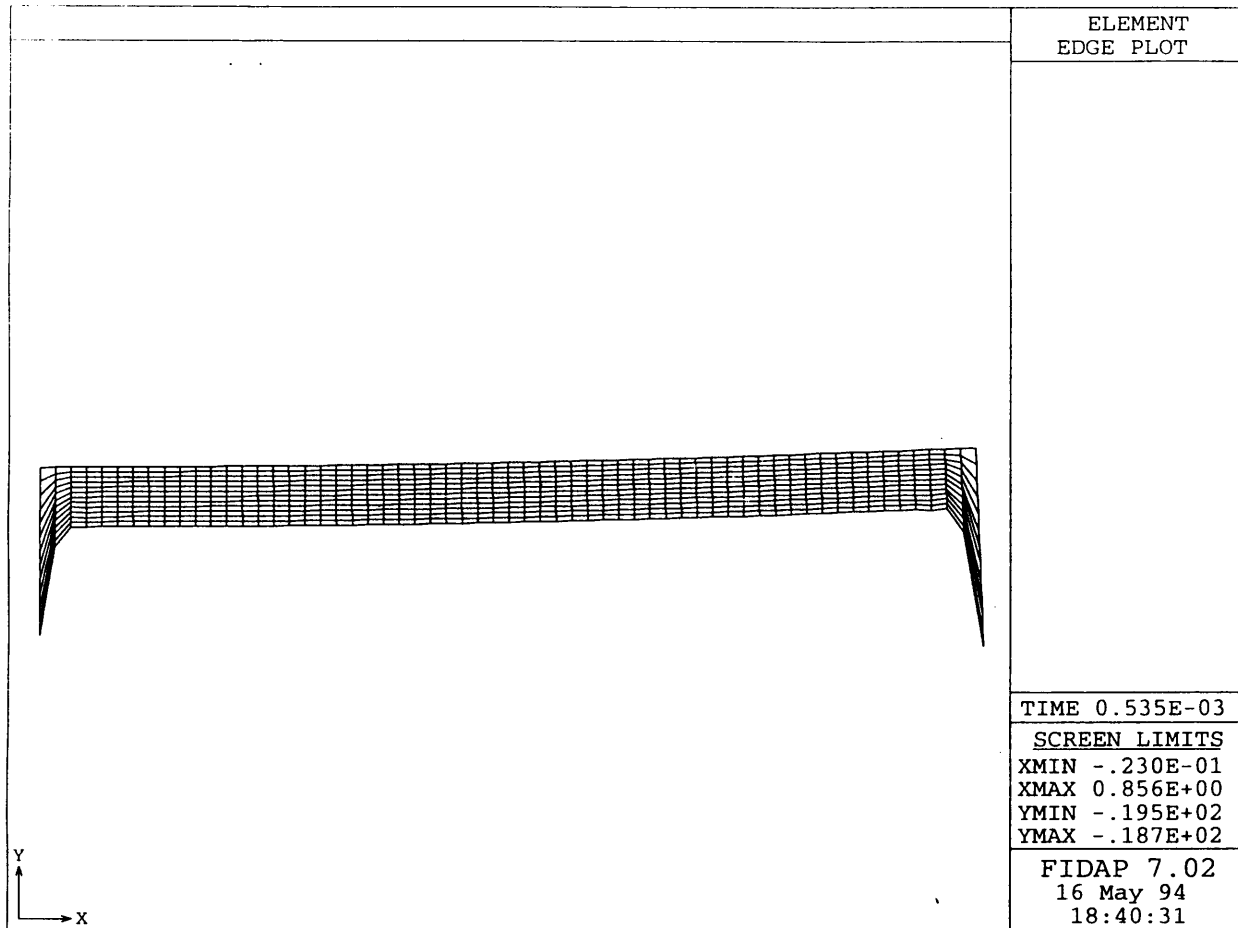
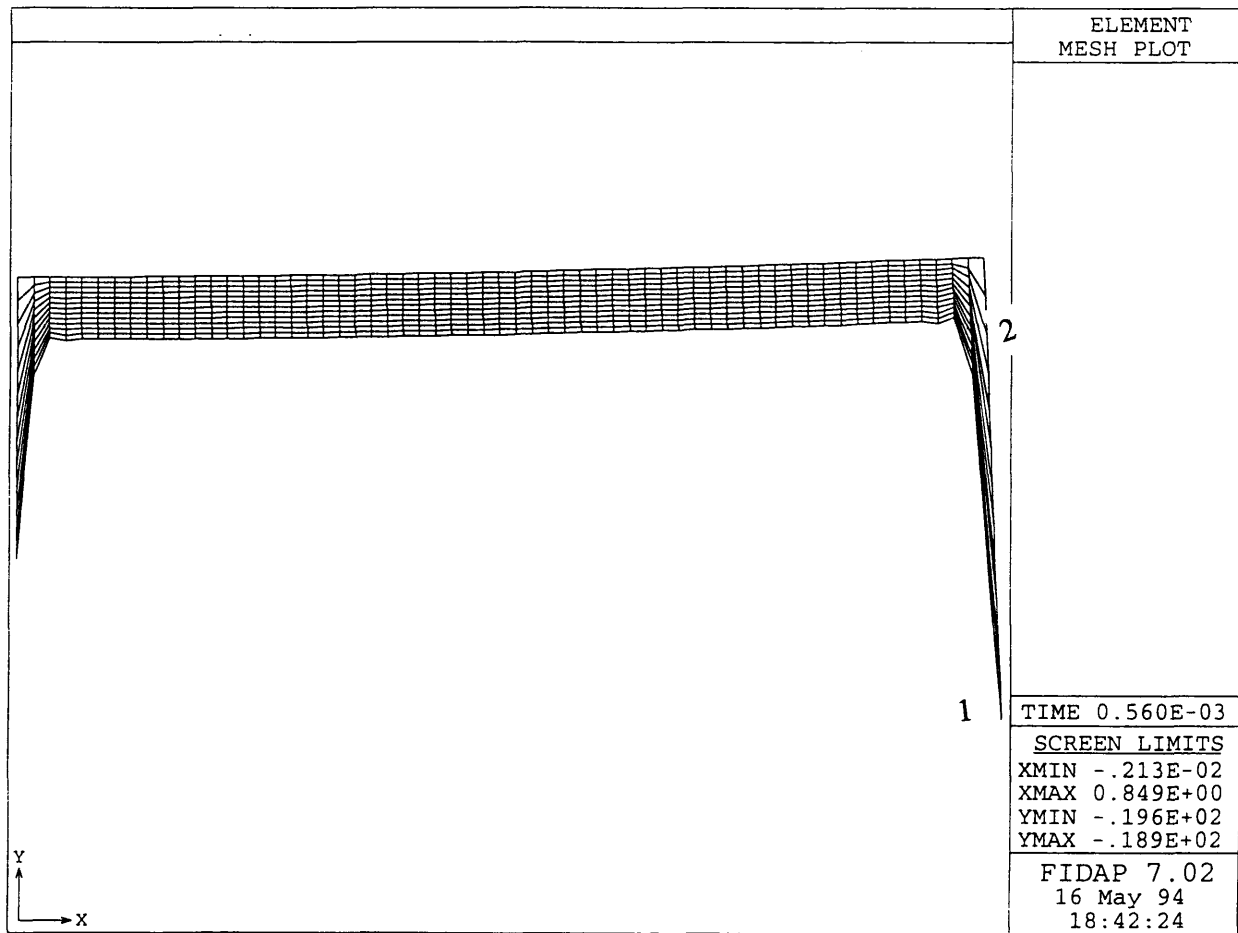


Figure 5.6. Mesh histories of the RT instability model:
a) Mesh at time = 4.5×10^{-4} seconds



**Figure 5.6. Mesh histories of the RT instability model:
b) Mesh at time = 5.35×10^{-4} seconds**



**Figure 5.6. Mesh histories of the RT instability model:
c) Mesh at time = 5.65×10^{-4} seconds**

The free surface model has 1100 elements and 1001 nodes as shown in Figure 5.7. At this point in the fiber formation process, the perturbation waves were already formed on the free surface. Therefore, the initial condition for the tangential glycerine velocity was equal to the disk tangent velocity ($V_T=518.7$ cm/s). The boundary conditions for this model included the disk tangent velocity, input velocity ($V_i=518.7$ cm/s), output velocity ($V_o=518.7$ cm/s) and pressure on the free surface ($P_s=1$ atm.). The time step was 5×10^{-6} seconds. All input data are listed in Appendix C.

The Quasi-Newton iteration method was also to obtain the nonlinear solutions of unknowns for this model. The position of the nodes on the free surface and the field variables such as velocity and pressure at the new nodal positions were calculated simultaneously after convergence was attained. Solutions were convergent until running time was equal to 1.15×10^3 seconds, and then it was divergent.

Figure 5.8 illustrates the free surface profile from the beginning to the final convergent time step. Note that the initial wave peak was destroyed, the final position of the wave peak was moved to the inlet side, the final shape of the thread was very different from that of the experimental results, and the diameter of the thread was much greater than expected. Figure 5.9 indicated the mesh histories. Some elements deformed dramatically and the element aspect ratio increased substantially. Also, some meshes were beyond the solid boundary, which resulted in a negative Jacobian value, and a divergent solution.

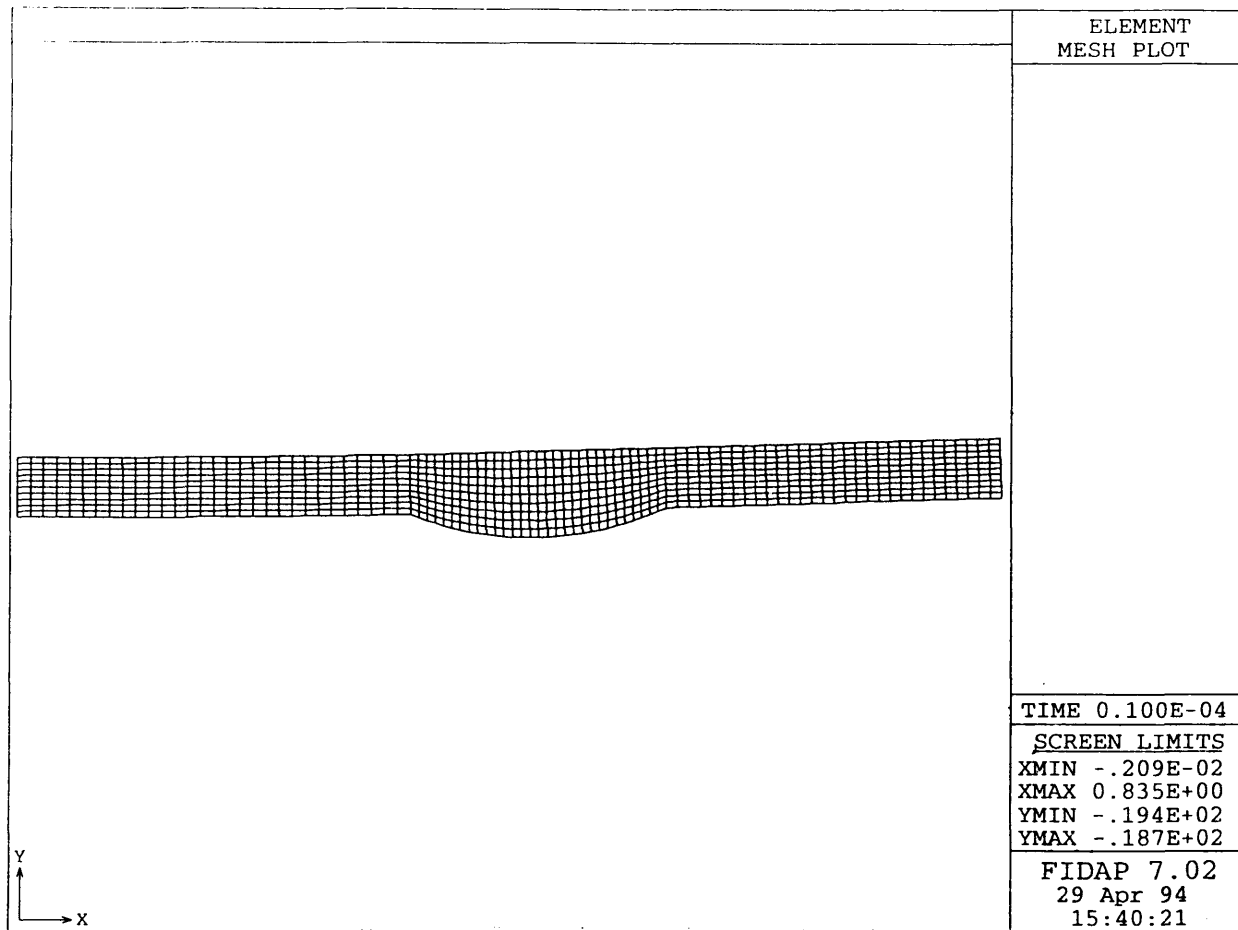


Figure 5.7. Geometry mesh of the free surface model

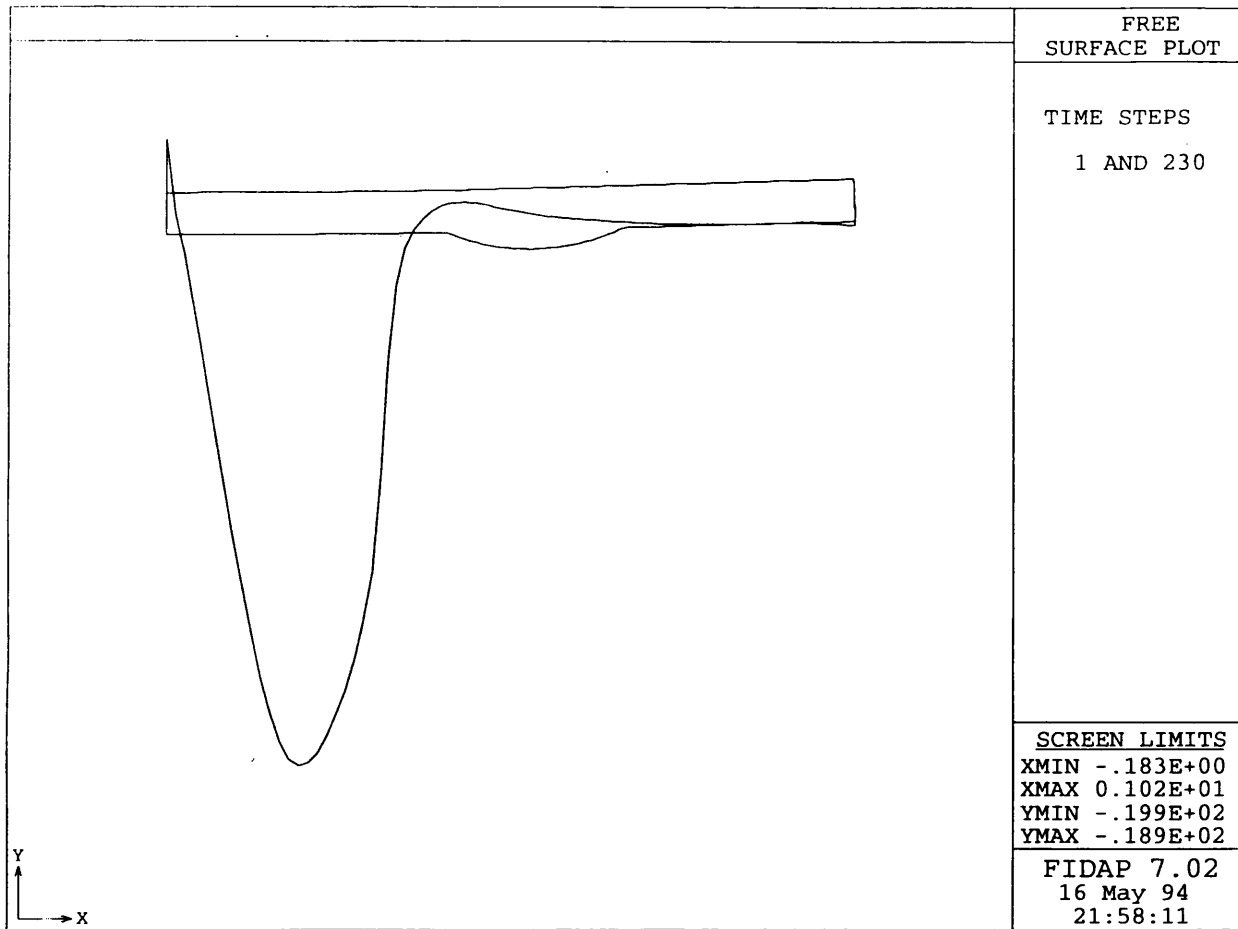


Figure 5.8. Free surface profile of the free surface model at running time equaled 1.15×10^{-3} seconds.

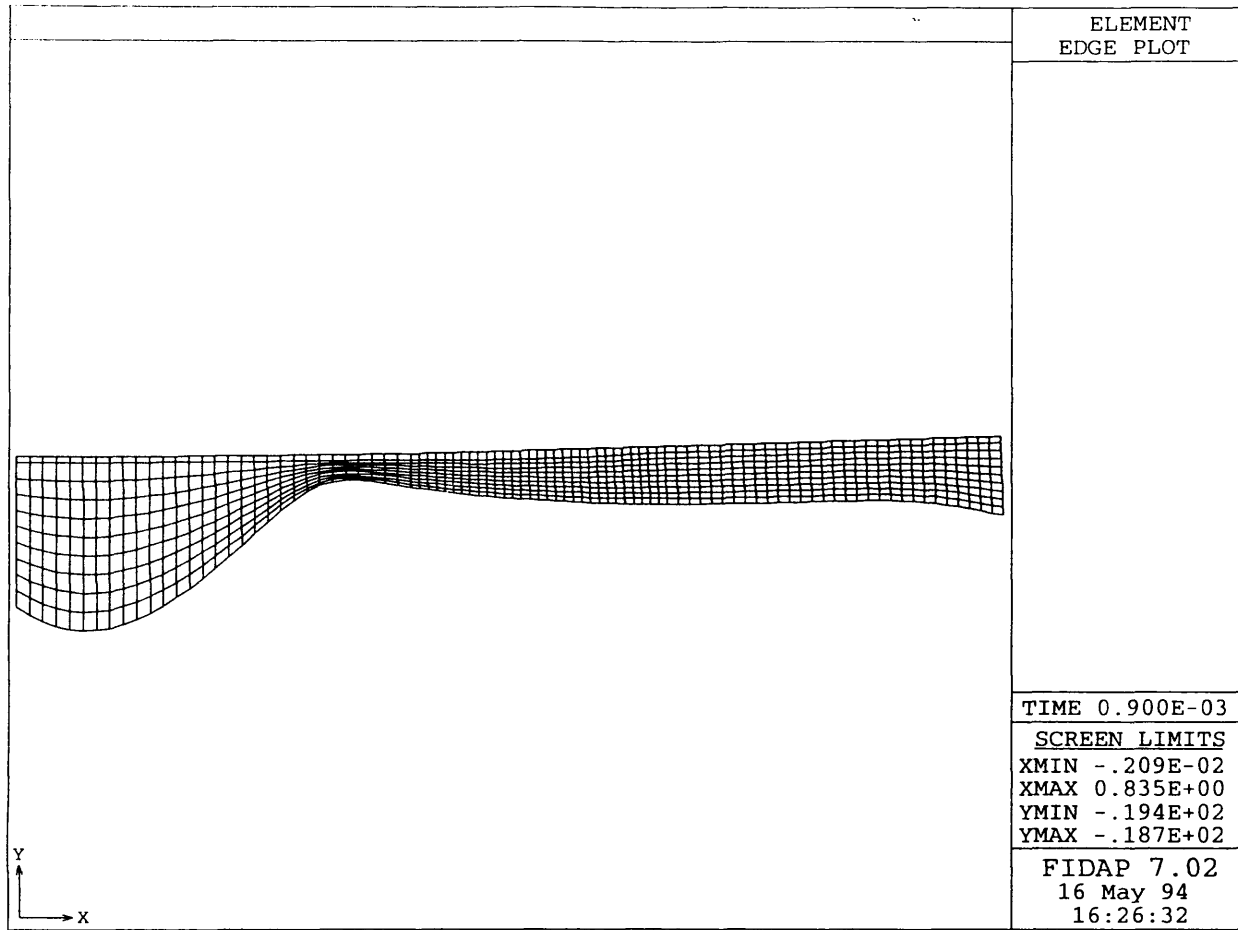
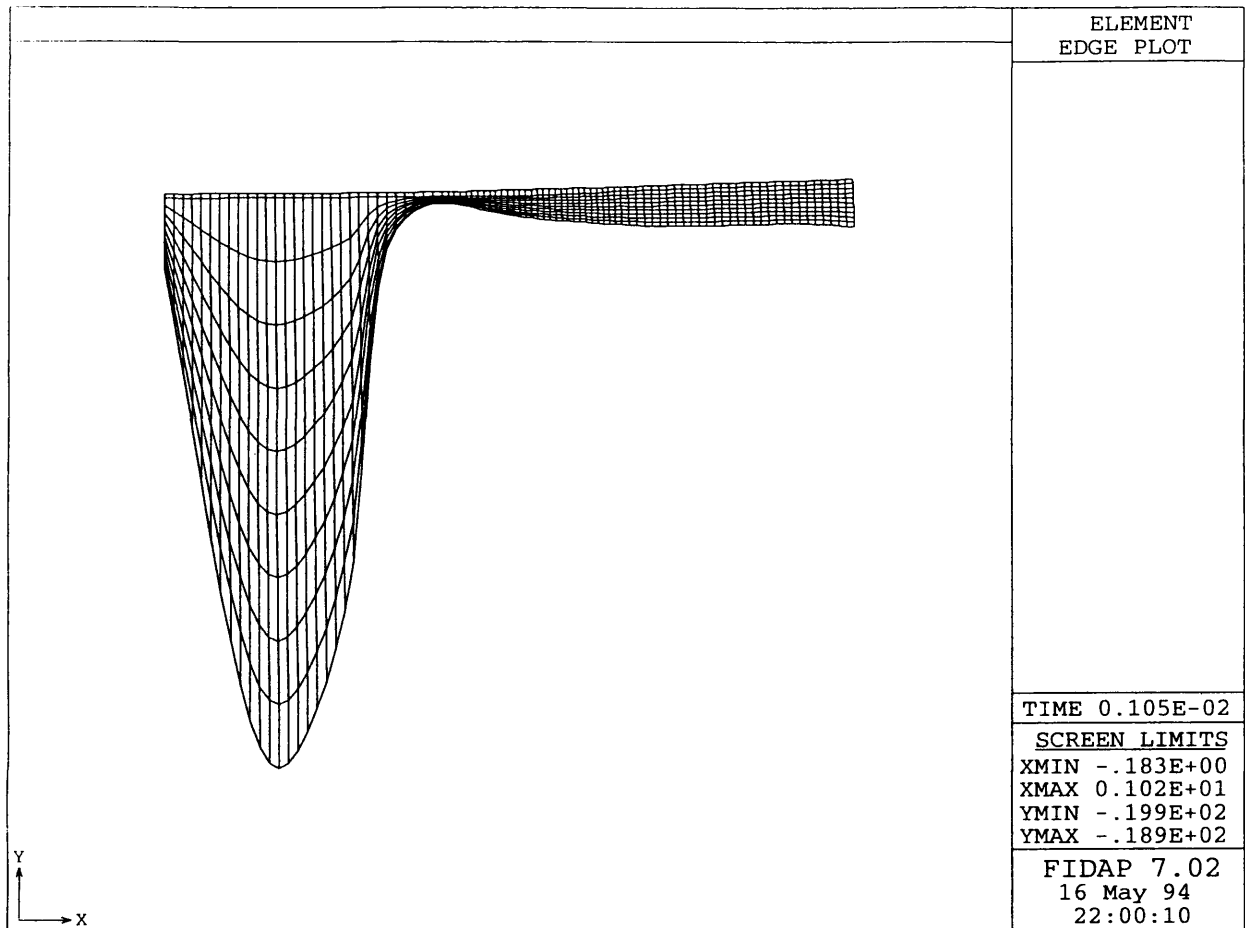


Figure 5.9. Mesh histories of the free surface model:
a) Mesh at time = 9.0×10^{-4} seconds.



**Figure 5.9. Mesh histories of the free surface model:
b) Mesh at time = 1.05×10^{-3} seconds**

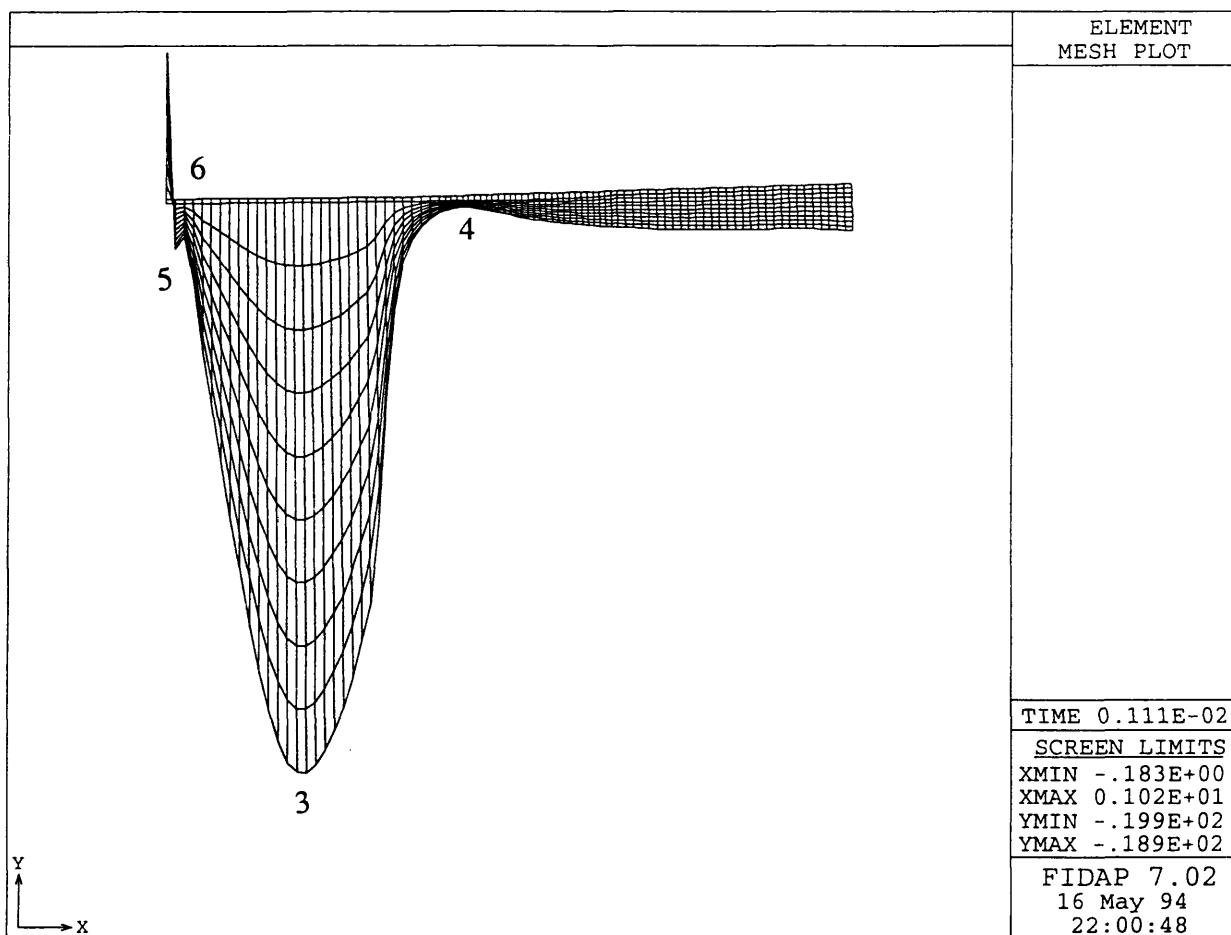


Figure 5.9. Mesh histories of the free surface model:
c) Mesh at time = 1.11×10^{-3} seconds.

5.2.3. Reasons for Unexpected Results

The numerical modeling results from both models did not follow the characteristics observed in experiments. One probable explanation is related to the convergence difficulty due to the large free surface deformation. Another is the incorrect free surface movement.

What causes these problems? The problem with convergence is perhaps due to the limitation of the FIDAP program because it did not have an adaptive remeshing function. When the free surface was deformed rapidly due to high centrifugal force or high input velocity, some elements enlarged and the shape of the elements was changed dramatically. Enlarged element size influences the convergence of the solution directly, because of a rough mesh of a configuration. Also, the aspect ratio, the ratio of the largest dimension of the element to the smallest dimension of the element for two dimensional elements (Rao, 1982), increased, resulting in convergence difficulties. Generally, elements with an aspect ratio of nearly one yield best results (Rao, 1982). If a mesh refinement function is provided, this problem may be overcome.

On the other hand, the changed element shape results in changes of interior angles of elements. Angle change causes the Jacobian value to change. If the interior angle is greater than π , the Jacobian value will be negative. The Jacobian is the determinant of the Jacobian matrix used for transformation between global and local coordinates of the element nodes. The necessary and sufficient conditions for

continuity requirements of the field variables is that the value of the Jacobian must be positive while the requirement for convergence is that the field variable must be continuous within the elements (Rao, 1983). Reddy (1993) pointed out that elements with any interior angle greater than π should not be used in any finite element mesh. In general, any interior angle θ should not be too small or too large, otherwise, the Jacobian value J will be very small. The well conditioned element shapes are defined as elements in which θ is in range $60^\circ < \theta < 120^\circ$ (Mustoe, 1989). As can be seen in Figures 5.6c and 5.9c, the interior angles of some deformed elements are very small, such as in element 1, some of them are very large, such as in element 2 in Figure 5.6c. Some elements became very small, such as in element 3, while other elements became very large, such as in element 4, in Figure 5.9c. The aspect ratio for some elements changed by more than an order of magnitude. If the deformed elements can be broken into smaller elements, with aspect ratio near unity, the interior angle and the aspect ratio will not change very much and convergence should follow. However, this modification was deemed beyond the scope of this study.

The problem with incorrect free surface profile is probably due to the limitation of finite element methods. Although the range and power of finite element methods present a formidable challenge to any other contending methods, the whole body discretization scheme leads to very large numbers of finite elements, within each of which the solution variables do not all vary continuously but frequently show unrealistic jumps in value between adjoining elements (Banerjee and Butterfield,

1981). It was the unrealistic value jumps that caused the incorrect surface profile. As we can see from the deformed meshes of the two models, the connection between some elements was not smooth, some singularity occurs as shown in Figure 5.9c, at position 5, elements were separated in opposite directions, at position 6, jumps occurred between elements. The singularity develops as the time steps increase. Finally, the results obtained did not represent realistic free surface movement. In the author's opinion, free surface displacement for fiberization process modeling is the dominant variable, and should be solved before either proceeding to any discretization scheme or introducing any approximations. But it is treated as the boundary conditions in the finite element methods after body discretization and approximation on geometry and linearization.

Another reason for the incorrect free surface movement may be related to the inaccuracies associated with using a 2-D model for a 3-D phenomenon. Because the free surface movement in the direction of the disk axis can not modeled in the 2-D model, and it may be varied dramatically along the disk axis. Therefore, a 3-D model may be needed for modeling the fiber formation process.

CHAPTER 6

CONCLUSIONS AND SUGGESTIONS FOR FURTHER WORK

6.1. Conclusions

Fiber formation by a spinning process has been modeled experimentally. As a result of this study, the mechanisms of this process are better understood.

Experimental results have verified that the centrifugal force is the driving force for fiber formation while the surface and viscous forces are the resisting forces to the fiber formation. The effects of the controllable parameters on the fiber parameters were qualitatively studied. Relationships between the fiber and controllable parameters have been quantitatively established. The author believes that the results can be used to improve the fiber formation process by appropriate adjustment of the controllable parameters. Therefore, the low viscosity fiber melt may also be manufactured by the spinning process.

In addition to experimental simulation, theoretical mechanisms for three stages of fiberization have been analyzed. Trends of the predicted RT instability growth rates, based on the linear instability theory, are consistent with those observed experimentally. Numerical modeling using the finite element program (FIDAP) has been attempted for two models. Although modeling results are not consistent with the experimental results, reasons for unexpected results have been found, which will provide a basis for further study on this subject.

6.2. Suggestions for Further Work

Although successful results for this work were obtained from the experimental simulation using glycerine as the substitute liquid, no analytical solutions and numerical modeling results were obtained for comparison. Also, some of the experimental results were limited to low disk rotation speeds. To better understand the whole process and provide more realistic information on process control, it will be necessary to find the appropriate numerical method to model this process.

Since the problem involved with fiberization process by spinning disk represents a free surface flow with large deformation and nonlinear advection, the problem is complicated, and most likely will not be solved by one single method. Because the Finite Element Method (FEM) is powerful for solving the nonlinear problem while the Boundary Element Method (BEM) is good on solving free surface flow problems, balancing the benefits between FEM and BEM on solving a particular problem is very important.

The author's suggestion for this problem is to utilize benefits from both methods by combination of FEM and BEM. First, the boundary integral representation should be constructed to satisfy the interfacial boundary conditions using BEM. The interfacial boundary conditions include the continuity of velocity across the interface and a constitutive relation for the discontinuity in the interfacial surface force (Pozrikidis, 1992). Newhouse (1991) has construct a boundary integral representation of the flow field capable of describing large layer deformations using Green's function

(an essential element of BEM). BEM is a method to find a solution by numerical integration while FEM is used to find a solution by numerical differentiation. Since numerical integration is always much more stable and precise than numerical differentiation (Banerjee and Butterfield, 1981), BEM holds promise to yield a convergent solution than does FEM.

Since BEM is only applicable to either completely linear systems or those which are or can be approximated as incremental linear systems, values of the solution variables can be calculated by FEM once the proper boundary information is obtained. Better results can be obtained using FEM for nonlinear problems. Furthermore, the adaptive remesh function should be provided at each time step to improve the degree of convergence.

REFERENCES CITED

- Baker, G. R., Meiron D. I. and Orszag S. A., 1984, Boundary integral methods for axisymmetric and three-dimensional Rayleigh-Taylor instability problems, Physica 12D, pp. 19-31.
- Banerjee, P. K. and Butterfield, R., 1981, Boundary Element Methods in Engineering Science, McGRAW-HILL Book Company (UK) Limited, London.
- Bansal, N.P., and Doremus R.H., 1986, Handbook of Glass Properties, Academic Press, New York.
- Bellman, Richard and Pennington, Ralph H., 1954, Effects of surface tension and viscosity on Taylor instability, Quarterly of Applied Mathematics, Vol. 12, pp. 151-162.
- Chandrasekhar, S., 1968, Hydrodynamic and Hydromagnetic Stability, Oxford University Press.
- Chen, Jim S.J., Praisner, T.L., Fields, L.A., Nornhold, R.T., and Frazier, William E., Rapid Solidification Processing of Titanium Aluminides by Melt Spinning, 1992, HTD-Vol.218/AMD-Vol.139, Micro/Macro Scale Phenomena, ASME.
- Dalziel, S. B., 1993, Rayleigh-Taylor instability: experiments with image analysis, Dynamics of atmospheres and Oceans, V20, n 1/2, pp. 127.
- Eisenklam, P., 1964, On ligament formation from spinning discs and cups, Chemical Engineering Science, Vol. 19, pp. 693-694.
- Fermigier M., Limat L. Wesfreid, J.E., Boudinet, P., and Quilliet, C., 1992, Two-dimensional patterns in Rayleigh-Taylor instability of a thin layer, Journal of Fluid Mechanics, Vol. 236, pp. 349-383.
- FDI (Fluid Dynamics International, Inc.), 1993, FIDAP7.0 package, Evanston, IL.
- Fraser, R. P., Dombrowski, N. and Routley, J. H., 1963, The filming of liquids by spinning cups, Chemical Engineering Science, Vol. 18, pp. 323-337.

- Glicksman, L.R., 1968, The cooling of glass fibers, Glass Technology, No. 9, pp. 131-138.
- Henney, Keith, and Dudley, Beverly, Handbook of Photography, 1939, Whittlesey House, New York.
- Hinze, J.O., and Milborn, H., 1950, Atomization of Liquids by Means of a Rotating Cup, Journal of Applied Mechanics, Vol. 17, pp. 145-153.
- Holman, J.P., and Gajda, W.J., 1989, Experimental Methods for Engineers, 5th Ed., McGraw-Hill, New York.
- Kull, H.J., 1991, Theory of the Rayleigh-Taylor Instability, Physics Reports, Vol. 206, No. 5.
- Kundu, Pijush K., Fluid Mechanics, 1990, Academic Press, Inc., New York.
- Liley, P.E, Makita, T., and Tanaka, Y., 1988, Properties of Inorganic and Organic Fluids, Vol. 1, Hemisphere Publishing Corporation, New York.
- Mekias Hocine and Vanden-Broeck Jean-Marc, 1989, Supercritical free-surface flow with a stagnation point due to submerged source, Physics of Fluids A 1(10), pp. 1694-1697.
- Mustoe, Graham, 1989, Class Notes of Introduction to the Finite Element Method, Colorado School of Mines, Golden, Colorado.
- Newhouse, L. A. and Pozrukidis C., 1990, The Rayleigh-Taylor instability of viscous liquid layer resting on a plane all, Journal of Fluid Mechanics, Vol. 217, pp. 615-638.
- Newhouse, L. A., 1991, Nonlinear instability of liquid layers, Ph.D. Dissertation, University of California, San Diego.
- Olds, Leonard, 1992, Personal communication, Schuller International, Denver.
- Paek, U. C., Schrieder C. M. and Kurkjian C. R., 1988, Determination of the viscosity of high silica glasses during fibre drawing, Glass Technology, Vol. 29, No 6, pp. 263-266.

- Parhi, S. and Nath G., 1991, A sufficient criterion for Rayleigh-Taylor instability of incompressible viscous three-layer flow, International Journal of Engineering Science, Vol. 29, No. 11. pp 1439-1450.
- Pozrikidis, C., 1992, Boundary Integral and Singularity Methods for Linearized Viscous Flow, Cambridge University Press, New York.
- Rao, S. S., 1982, The Finite Element Method in Engineering, Pergamon Press, Oxford, England.
- Reddy, J. N., 1993, An Introduction to the Finite Element Method, Second Edition, McGraw-Hill, Inc., New York.
- Schlichting, H., 1968, Boundary-Layer Theory, Sixth Edition, McGraw-Hill, Inc.
- Sharp, D. H., 1984, An overview of Rayleigh-Taylor instability, Physica 12D; pp 3-18.
- Subochev, I. G., Pitak, N. V., Eremina, I.V., Kornitskii, L.I., Yakovlev, A.I., Rasput'ko, G.S., and Churilov, V.V, 1989, Refractory fiber formation processes, plenum publishing Corporation, Translated from Ogneupory, No. 12, pp. 3-8.
- Vargaftik, N.B., 1983, Handbook of Physical Properties of Liquids and Gas, 2nd Ed., Hemisphere Pub. Corp., Washington.
- Weast, R.C. and Selby, S. M., 1976, Handbook of Chemistry and Physics, 48 Ed., The Chemical Rubber CO., Ohio.
- Westerlund T. and Hoikka T., 1989, On the modeling of mineral fiber formation, Computers of Chemical Engineering, Vol. 13, No. 10, PP 1153-1163.
- Wilson, T.L., Nichols, B.D., Hirt, C.W. and Stein, L.R., 1980, SOLA-VOF: A solution Algorithm for transient fluid flow with multiple free boundaries, Report No. LA-8355, Los Alamos Scientific Laboratory, University of California.
- Youngs, David L., 1984, Numerical simulation of turbulent mixing by Rayleigh-Taylor instability, Physica 12D, pp. 32-44.

Ziabicki, Andrzej, 1976, Fundamentals of Fibre Formation, John Wiley & Sons, New York.

APPENDIX A

CALIBRATED RELATIONSHIPS USED IN THE EXPERIMENTS

The calibrated relationship between the disk rotation speed and the DC output voltage of the tachometer plotted in Figure A1 was obtained by following procedures. First, a disk rotation speed was set to the lower speed, and measured using a contacted tachometer after a DC motor rotated smoothly. Next, a DC output voltage from a voltage meter generated by the disk speed tachometer was recorded, which corresponds to the rotation speed. A set of data was obtained. Six sets of data related to different rotation speeds were obtained. Finally, the data were analyzed using a least square method to correlate their relationship. It was found that their relationship is linear as shown in the Figure A1. This relationship was used to measure the disk rotation speed for the experiment based on readings of the voltage meter.

The calibrated relationship between the liquid flow rate and the DC output voltage of the flowmeter plotted in the Figure A2 was obtained as follows. Glycerine weight (w) within a period of time ($\Delta\tau$) was measured using a weight scale, and the liquid flow rate was calculated by $w/\rho\Delta\tau$. A DC voltage from a voltage meter generated by the liquid flow meter was recorded. A set of data including the liquid flow rate and voltage was obtained. A linear relationship was obtained by analyzing

five sets of this data using a least square method. Also, this relationship was used in the experiments to measure the liquid flow rate based on the voltage readings from a voltage meter.

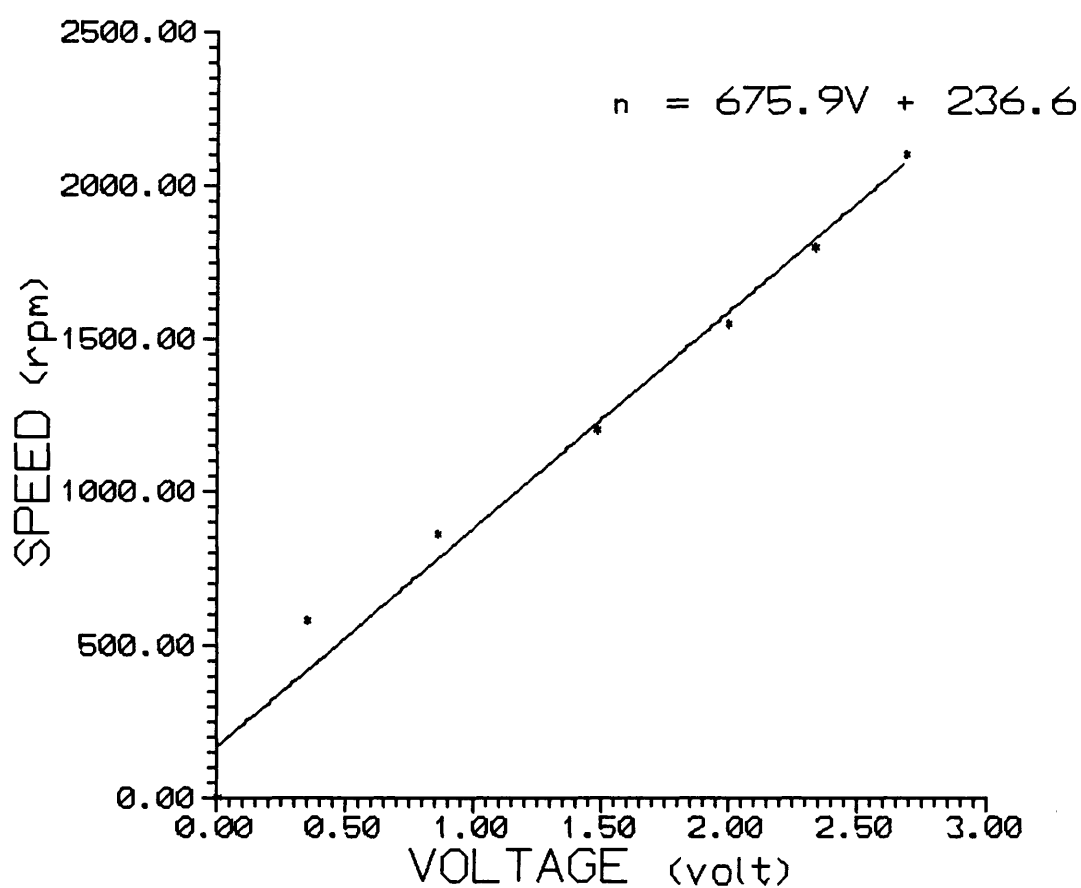


Figure A1. Disk rotation speed versus voltage.

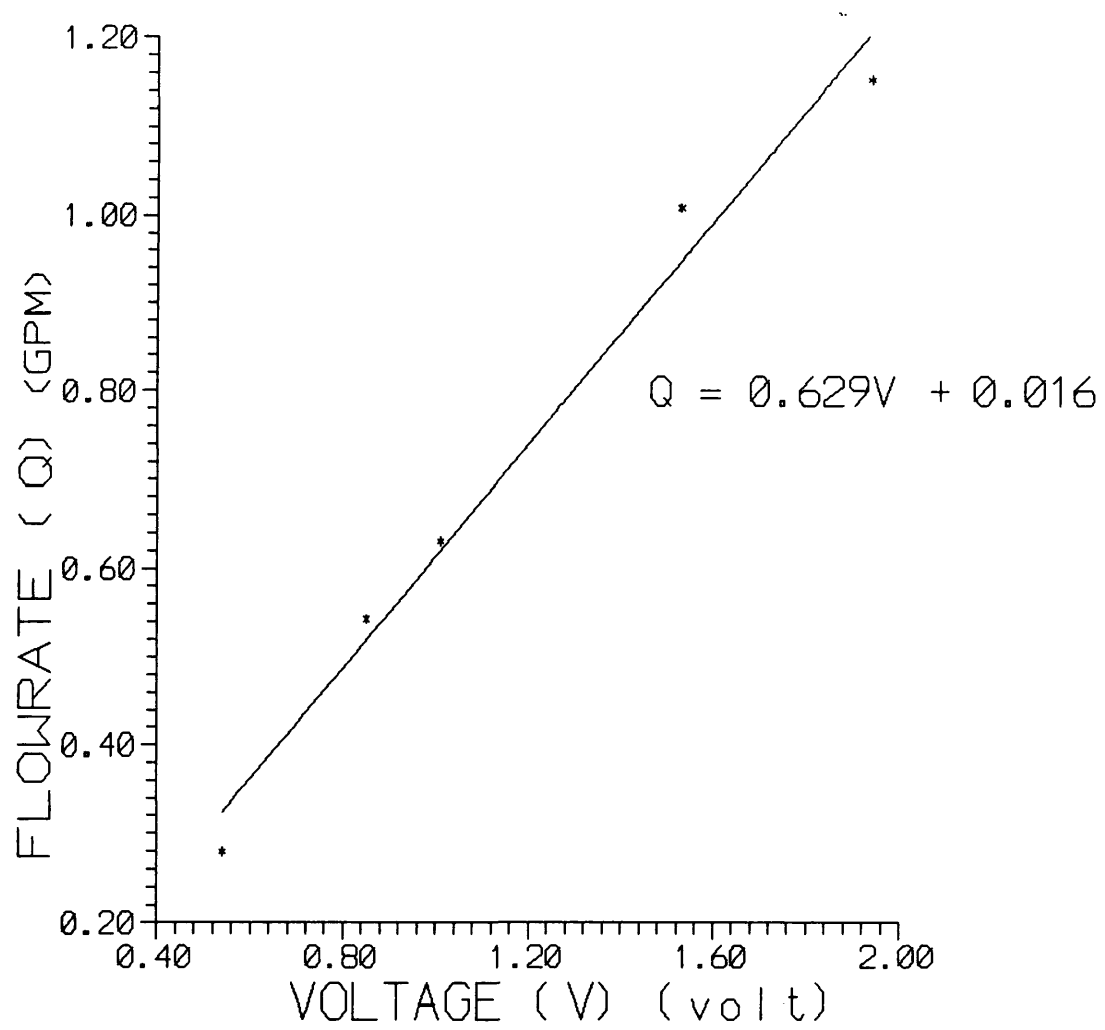


Figure A2. Glycerine flow rate versus voltage.

APPENDIX B

INPUT FILE FOR THE RT INSTABILITY MODEL

(The unit used in this file is the CGS unit, that is using centimeter for length, gram for mass and second for time.)

TITLE

INSTABILITY MODEL FOR MODELING FIBER FORMATION PROCESS
 FI-GEN (ELEMENT=1, POINT=1, CURVE=1, SURFACE=1, NODE=0,
 MEDGE=1, MLOOP=1, MFACE=1, BEDGE=1, SPAVE=1, MSHELL=1,
 MSOLID=1)

WINDOW(CHANGE= 1, MATRIX)

1.000000	0.000000	0.000000	0.000000		
0.000000	1.000000	0.000000	0.000000		
0.000000	0.000000	1.000000	0.000000		
0.000000	0.000000	0.000000	1.000000		
-10.00000	10.00000	-7.50000	7.50000	-7.50000	7.50000

pgrid(on)

pgrid(snap)

WINDOW(CHANGE= 1, MATRIX)

1.000000	0.000000	0.000000	0.000000		
0.000000	1.000000	0.000000	0.000000		
0.000000	0.000000	1.000000	0.000000		
0.000000	0.000000	0.000000	1.000000		
-24.87685	24.87685	-18.65764	18.65764	-5.78387	5.78387

WINDOW(CHANGE= 1, MATRIX)

1.000000	0.000000	0.000000	0.000000		
0.000000	1.000000	0.000000	0.000000		
0.000000	0.000000	1.000000	0.000000		
0.000000	0.000000	0.000000	1.000000		
-30.52678	30.52678	-22.89508	22.89508	-7.09748	7.09748

point(add,coordinates,x=0,y=-19.05)

point(add,coordinates,x=0.3325,y=-19.047)

point(add,coordinates,x=0.831,y=-19.0319)

point(add,coordinates,x=0,y=-19.1008)

point(add,coordinates,x=0.3334,y=-19.0979)

point(add,coordinates,x=0.833,y=-19.0826)

WINDOW(CHANGE= 1, MATRIX)

1.000000	0.000000	0.000000	0.000000
0.000000	1.000000	0.000000	0.000000
0.000000	0.000000	1.000000	0.000000

```

0.000000  0.000000  0.000000  1.000000
-0.02082  0.85382  -19.39434  -18.73836  -0.87465  0.87465
pgrid(off)
pgrid(nosnap)
point(select,location,window=1)
    0.022,    0.524
/ ID = 1
    0.404,    0.524
/ ID = 2
    0.978,    0.541333
/ ID = 3
    0.031,    0.438667
/ ID = 4
    0.41,     0.430667
/ ID = 5
utility(unselect,last)
utility(unselect,last)
curve(add,arc)
point(select,location,window=1)
    0.027,    0.44
/ ID = 4
    0.409,    0.437333
/ ID = 5
    0.976,    0.464
/ ID = 6
curve(add,arc)
point(select,location,window=1)
    0.024,    0.516
/ ID = 1
    0.024,    0.436
/ ID = 4
curve(add,line)
point(select,location,window=1)
    0.979,    0.552
/ ID = 3
    0.98,     0.465333
/ ID = 6
curve(add,line)
medge(setdefaults,intervals=3)
medge(setdefaults,intervals=60)
curve(select,location,window=1)

```

```

    0.762,    0.538667
/ ID = 1
    0.757,    0.456
/ ID = 2
medge(add,intervals=60)
curve(select,location>window=1)
    0.03,    0.481333
/ ID = 2
curve(select,next=1)
/ ID = 3
curve(select,location>window=1)
    0.991,    0.517333
/ ID = 4
medge(add)
medge(setdefaults,intervals=12)
medge(select,location>window=1)
    0.981,    0.517333
/ ID = 1
medge(select,next=1)
/ ID = 4
medge(select,location>window=1)
    0.034,    0.486667
/ ID = 1
medge(select,next=1)
/ ID = 2
medge(select,next=1)
/ ID = 3
medge(modify,intervals=12)
curve(select,location>window=1)
    0.788,    0.532
/ ID = 1
    0.982,    0.514667
/ ID = 4
    0.846,    0.461333
/ ID = 2
    0.03,    0.489333
/ ID = 3
mloop(add,map,visible,edg1cnt=1,edg2cnt=1,edg3cnt=1,edg4cnt=1)
curve(select,all)
mface(wireframe,edg1cnt=1,edg2cnt=1,edg3cnt=1,edg4cnt=1)
curve(select,location>window=1)

```

```

    0.653,    0.530667
/ ID = 1
    0.982,    0.518667
/ ID = 4
    0.882,    0.457333
/ ID = 2
    0.029,    0.489333
/ ID = 3
mface(wireframe,edg1cnt=1,edg2cnt=1,edg3cnt=1,edg4cnt=1)
mface(select,location>window=1)
    0.918,    0.465333
/ ID = 1
mface(mesh,map,entity="glycerine")
medge(setdefaults,intervals=12)
medge(select,location>window=1)
    0.582,    0.534667
/ ID = 1
element(setdefaults,edge,nodes=2)
medge(mesh,map,entity="disk-slip")
medge(select,location>window=1)
    0.67,     0.456
/ ID = 2
medge(mesh,map,entity="free")
medge(select,location>window=1)
    0.025,    0.482667
/ ID = 2
medge(select,next=1)
/ ID = 3
medge(mesh,map,entity="inlet")
END

```

FIPREP

DATAPRINT(ADD, CONTROL)

EXECUTION(ADD, NEWJOB)

PRESSURE(ADD, MIXED, DISCONTINUOUS)

PRINTOUT(ADD, NONE, BOUNDARY)

PROBLEM(ADD, 2-D, NONLINEAR)

SOLUTION(ADD, Q.N.=25, VELCONV=0.01, RESCONV=0.1, ACCF=0.,
NOLINESRCH)

ENTITY(ADD, NAME="glycerine", FLUID)

ENTITY(ADD, NAME="disk-slip", SLIP)


```

ENTITY( ADD, NAME="free", SURFACE, DEPTH=0, CONTINUE, SPINES,
STRAIGHT, ANG1= 180.0, ANG2= 5.0 )
NTITY( ADD, NAME="inlet", PLOT )
ENTITY( ADD, NAME="outlet", PLOT )

DENSITY( ADD, SET=1, CONSTANT=1.26 )
SURFACETENSION( ADD, SET=1, CONSTANT=62.3, PRESSURE=0 )
VISCOSITY( ADD, SET=1, CONSTANT=6.29 )
RELAXATION( ADD, SURFACE=0 )
SOLUTION( REPLACE, ENTRY=1, Q.N.= 25, VELCONV= 0.1, RESCONV=
0.1,
ACCF= 0.000000000000E+00, NOLINESRCH )BCNODE( ADD, COORDINATE,
NODES=1 )

BCNODE( ADD, COORDINATE, NODES=2 )
BCNODE( ADD, COORDINATE, NODES=63 )
BCNODE( ADD, COORDINATE, NODES=62 )
BCNODE( ADD, UT, ENTITY="disk-slip", zero )
BCNODE( ADD, UX, ENTITY="inlet", zero )
BCNODE( ADD, UX, ENTITY="outlet", zero )
BCNODE( ADD, UN, ENTITY="disk-slip", ZERO )
BCNODE( ADD, UN, ENTITY="free", ZERO )
BODYFORCE( ADD, CONSTANT, FX=0., FY=17653, FZ=0. )

ICNODE( ADD, UX, ZERO, ENTITY="glycerine" )
ICNODE( ADD, SURFACE, ZERO )

TIMEINTEGRATION( REPLACE, ENTRY=1, BACKWARD, NSTEPS= 500,
TSTART= 0.000000000000E+00, DT= 0.500000000000E-05, FIXED, WINDOW )
FIPOST ( )
DEVICE( POSTSCRIPT, HARDWARE )
FREE( FIRST=1, LAST=230 )
MOVIE( STEPS, DT=5, FIRST=210, LAST=236 )
MESH( )
CONTOUR( UX, AUTOMATIC )
CONTOUR( UY, AUTOMATIC )
CONTOUR( STREAMLINE, AUTOMATIC )
CONTOUR( REYNOLDS, AUTOMATIC )
VECTOR( VELOCITY )
CONVERGENCE( ALL, SOLUTION, LINEAR )
END

```

APPENDIX C

INPUT FILE FOR THE FREE SURFACE MODEL

(The unit used in this file is the CGS unit, that is using centimeter for length, gram for mass and second for time.)

TITLE

THE FREE SURFACE MODEL OF MODELING FIBER FORMATION
 FI-GEN(ELEMENT=1, POINT=1, CURVE=1, SURFACE=1, NODE=0,
 MEDGE=1, MLOOP=1, MFACE=1, BEDGE=1, SPAVE=1, MSHELL=1,
 MSOLID=1)

WINDOW(CHANGE= 1, MATRIX)

1.000000	0.000000	0.000000	0.000000		
0.000000	1.000000	0.000000	0.000000		
0.000000	0.000000	1.000000	0.000000		
0.000000	0.000000	0.000000	1.000000		
-10.00000	10.00000	-7.50000	7.50000	-7.50000	7.50000

pgrid(on)

pgrid(snap)

WINDOW(CHANGE= 1, MATRIX)

1.000000	0.000000	0.000000	0.000000		
0.000000	1.000000	0.000000	0.000000		
0.000000	0.000000	1.000000	0.000000		
0.000000	0.000000	0.000000	1.000000		
-24.87685	24.87685	-18.65764	18.65764	-5.78387	5.78387

WINDOW(CHANGE= 1, MATRIX)

1.000000	0.000000	0.000000	0.000000		
0.000000	1.000000	0.000000	0.000000		
0.000000	0.000000	1.000000	0.000000		
0.000000	0.000000	0.000000	1.000000		
-30.52678	30.52678	-22.89508	22.89508	-7.09748	7.09748

point(add,coordinates,x=0,y=-19.05)

point(add,coordinates,x=0.3325,y=-19.047)

point(add,coordinates,x=0.831,y=-19.0319)

point(add,coordinates,x=0,y=-19.1008)

point(add,coordinates,x=0.3334,y=-19.0979)

point(add,coordinates,x=0.833,y=-19.0826)

WINDOW(CHANGE= 1, MATRIX)

1.000000	0.000000	0.000000	0.000000		
0.000000	1.000000	0.000000	0.000000		

```

0.000000  0.000000  1.000000  0.000000
0.000000  0.000000  0.000000  1.000000
-0.02082  0.85382  -19.39434  -18.73836  -0.87465  0.87465
point(add,location,window=1)
    0.917,    0.684
/ (X,Y,Z) = 0.781236 -18.9458 0
point(add,coordinates,x=1.6603,y=-18.9775)
WINDOW(CHANGE= 1, MATRIX )
    1.000000  0.000000  0.000000  0.000000
    0.000000  1.000000  0.000000  0.000000
    0.000000  0.000000  1.000000  0.000000
    0.000000  0.000000  0.000000  1.000000
    -0.04151  1.70181  -19.69289  -18.38541  -1.74331  1.74331
point(select,location,window=1)
    0.506,    0.509333
/ ID = 3
    0.225,    0.494667
/ ID = 2
    0.029,    0.492
/ ID = 1
curve(add,arc)
point(select,location,window=1)
    0.512,    0.46
/ ID = 6
    0.344,    0.466667
/ ID = 10
    0.217,    0.458667
/ ID = 5
    0.026,    0.448
/ ID = 4
curve(add,arc)
point(select,location,window=1)
    0.506,    0.464
/ ID = 6
    0.215,    0.458667
/ ID = 5
    0.028,    0.453333
/ ID = 4
curve(add,arc)
point(select,location,window=1)
    0.504,    0.504

```

```
/ ID = 3
    0.504,    0.466667
/ ID = 6
curve(add)
point(select,location>window=1)
    0.394,    0.866667
curve(select,location>window=1)
    0.339,    0.465333
/ ID = 32
curve(select,next=1)
/ ID = 33
curve(select,next=1)
/ ID = 34
curve(select,location>window=1)
    0.216,    0.456
/ ID = 32
utility(unselect,all)
curve(select,location>window=1)
    0.392,    0.461333
/ ID = 34
point(select,location>window=1)
    0.217,    0.457333
/ ID = 5
curve(split)
curve(select,location>window=1)
    0.441,    0.470667
/ ID = 33
curve(select,next=1)
/ ID = 36
point(select,location>window=1)
    0.341,    0.461333
/ ID = 10
curve(split)
curve(select,location>window=1)
    0.277,    0.462667
/ ID = 32
curve(select,next=1)
/ ID = 33
curve(select,next=1)
/ ID = 39
curve(delete)
```

```
point(add,location,window=1)
    0.337,    0.504
/ (X,Y,Z) = 0.547206 -19.0423 0
curve(select,location,window=1)
    0.274,    0.496
/ ID = 33
point(select,location,window=1)
    0.22, .    0.492
/ ID = 2
curve(split)
curve(select,location,window=1)
    0.451,    0.497333
/ ID = 38
curve(select,next=1)
/ ID = 39
curve(delete)
curve(select,location,window=1)
    0.44,    0.448
/ ID = 38
curve(delete)
point(select,location,window=1)
    0.503,    0.506667
/ ID = 3
    0.339,    0.496
/ ID = 10
point(select,next=1)
/ ID = 11
point(select,location,window=1)
    0.233,    0.513333
/ ID = 2
curve(add,arc)
point(select,location,window=1)
    0.508,    0.462667
/ ID = 6
    0.342,    0.461333
/ ID = 10
    0.214,    0.454667
/ ID = 5
curve(add,arc)
curve(select,location,window=1)
    0.35,    0.464
```

```
/ ID = 32
curve(select,next=1)
/ ID = 42
point(select,location>window=1)
    0.348,    0.454667
/ ID = 10
curve(split)
curve(select,location>window=1)
    0.288,    0.464
/ ID = 32
curve(select,next=1)
/ ID = 41
curve(select,next=1)
/ ID = 44
curve(delete)
curve(select,location>window=1)
    0.174,    0.496
/ ID = 37
curve(select,next=1)
/ ID = 40
curve(select,location>window=1)
    0.473,    0.502667
/ ID = 35
curve(select,next=1)
/ ID = 41
curve(select,location>window=1)
    0.507,    0.489333
/ ID = 35
    0.477,    0.46
/ ID = 43
    0.327,    0.449333
/ ID = 32
    0.183,    0.453333
/ ID = 37
    0.024,    0.470667
/ ID = 29
mface(wireframe,edg1cnt=2,edg2cnt=1,edg3cnt=3,edg4cnt=1)
WINDOW(CHANGE= 1, MATRIX )
    1.000000  0.000000  0.000000  0.000000
    0.000000  1.000000  0.000000  0.000000
    0.000000  0.000000  1.000000  0.000000
```

```

0.000000  0.000000  0.000000  1.000000
-0.02086  0.85383  -19.41539  -18.75938  -0.87469  0.87469
point(select,location,window=1)
    0.03,    0.496
/ ID = 1
    0.219,   0.494667
/ ID = 2
    0.509,   0.504
/ ID = 3
curve(add,arc)
point(add,location,window=1)
    0.337,   0.505333
/ (X,Y,Z) = 0.547206 -19.0406 0
curve(select,location,window=1)
    0.452,   0.462667
/ ID = 18
curve(delete)
curve(select,location,window=1)
    0.454,   0.494667
/ ID = 33
    0.217,   0.489333
/ ID = 21
point(select,location,window=1)
    0.217,   0.490667
/ ID = 2
curve(split)
utility(unselect,all)
curve(select,location,window=1)
    0.409,   0.490667
/ ID = 33
curve(split)
utility(unselect,all)
curve(select,location,window=1)
    0.463,   0.504
/ ID = 33
point(select,location,window=1)
    0.222,   0.490667
/ ID = 2
curve(split)
curve(select,location,window=1)
    0.472,   0.508

```

```
/ ID = 35
curve(delete)
point(select,location,window=1)
    0.217,    0.496
/ ID = 2
    0.349,    0.505333
/ ID = 11
    0.51,    0.510667
/ ID = 3
curve(add,arc)
point(select,location,window=1)
    0.215,    0.452
/ ID = 5
    0.352,    0.458667
/ ID = 10
    0.52,    0.457333
/ ID = 6
curve(add,arc)
point(select,location,window=1)
    0.504,    0.508
/ ID = 3
    0.511,    0.465333
/ ID = 6
curve(add)
point(select,location,window=1)
    0.218,    0.496
/ ID = 2
    0.217,    0.454667
/ ID = 5
curve(add)
point(select,location,window=1)
    0.343,    0.497333
/ ID = 10
    0.345,    0.492
/ ID = 10
    0.343,    0.498667
/ ID = 10
    0.343,    0.508
/ ID = 11
curve(add)
curve(select,location,window=1)
```



```

    0.466,    0.462667
/ ID = 36
point(select,location,window=1)
    0.343,    0.461333
/ ID = 10
curve(split)
curve(select,location,window=1)
    0.294,    0.462667
/ ID = 32
curve(select,next=1)
/ ID = 40
curve(delete)
WINDOW(CHANGE= 1, MATRIX )
    1.000000  0.000000  0.000000  0.000000
    0.000000  1.000000  0.000000  0.000000
    0.000000  0.000000  1.000000  0.000000
    0.000000  0.000000  0.000000  1.000000
    -0.02082  0.85382 -19.40274 -18.74676  -0.87465  0.87465
curve(select,location,window=1)
    0.033,    0.5
/ ID = 21
    0.025,    0.505333
/ ID = 29
    0.063,    0.529333
/ ID = 34
    0.411,    0.502667
/ ID = 32
curve(select,next=1)
/ ID = 35
curve(select,next=1)
/ ID = 38
mface(wireframe,edg1cnt=1,edg2cnt=1,edg3cnt=1,edg4cnt=1)
curve(select,location,window=1)
    0.41,    0.486667
/ ID = 21
curve(select,next=1)
/ ID = 32
curve(select,next=1)
/ ID = 38
curve(select,location,window=1)
    0.617,    0.54

```

```
/ ID = 35
utility(unselect,all)
curve(select,location,window=1)
    0.76,    0.552
/ ID = 35
point(select,location,window=1)
    0.656,    0.542667
/ ID = 11
curve(split)
curve(select,location,window=1)
    0.408,    0.524
/ ID = 34
curve(select,next=1)
/ ID = 38
curve(select,location,window=1)
    0.619,    0.541333
/ ID = 42
    0.656,    0.505333
/ ID = 32
curve(select,next=1)
/ ID = 39
curve(select,location,window=1)
    0.582,    0.410667
/ ID = 32
mface(wireframe,edg1cnt=1,edg2cnt=1,edg3cnt=1,edg4cnt=1)
curve(select,location,window=1)
    0.659,    0.513333
/ ID = 32
curve(select,next=1)
/ ID = 39
curve(select,location,window=1)
    0.846,    0.556
/ ID = 43
    0.989,    0.510667
/ ID = 37
    0.957,    0.484
/ ID = 41
mface(wireframe,edg1cnt=1,edg2cnt=1,edg3cnt=1,edg4cnt=1)
medge(setdefaults,intervals=3)
medge(setdefaults,intervals=10)
curve(select,location,window=1)
```

```
    0.028,    0.485333
/ ID = 21
curve(select,next=1)
/ ID = 29
curve(select,location>window=1)
    0.41,    0.52
/ ID = 34
curve(select,next=1)
/ ID = 38
curve(select,location>window=1)
    0.655,    0.494667
/ ID = 32
curve(select,next=1)
/ ID = 39
curve(select,location>window=1)
    0.985,    0.512
/ ID = 37
medge(add,intervals=10)
medge(setdefaults,intervals=30)
curve(select,location>window=1)
    0.285,    0.450667
/ ID = 21
    0.286,    0.529333
/ ID = 34
    0.501,    0.538667
/ ID = 42
    0.519,    0.426667
/ ID = 32
    0.762,    0.550667
/ ID = 43
    0.759,    0.46
/ ID = 41
medge(add,intervals=30)
mface(select,all)
mface(mesh,map,entity="glycerine")
medge(setdefaults,intervals=30)
medge(select,location>window=1)
    0.313,    0.46
/ ID = 5
    0.434,    0.44
/ ID = 8
```

```

    0.736,    0.464
/ ID = 10
element(setdefaults,edge,nodes=2)
medge(mesh,map,entity="free")
medge(select,location>window=1)
    0.292,    0.54
/ ID = 6
    0.506,    0.544
/ ID = 7
    0.76,    0.556
/ ID = 9
medge(mesh,map,entity="disk-slip")
medge(select,location>window=1)
    0.027,    0.482667
/ ID = 1
medge(mesh,map,entity="inlet")
bgadd(add,edge,entity="outlet")
WINDOW(CHANGE= 1, MATRIX )
    1.000000  0.000000  0.000000  0.000000
    0.000000  1.000000  0.000000  0.000000
    0.000000  0.000000  1.000000  0.000000
    0.000000  0.000000  0.000000  1.000000
    -0.02082  0.85382 -19.40273 -18.74675  -0.87465  0.87465
medge(setdefaults,intervals=3)
element(setdefaults,edge,nodes=2)
medge(mesh,map,group=5,entity="outlet")
END

```

FIPREP

PROBLEM(ADD, NONLINEAR, FREE)

PRESSURE(ADD, MIXED, DISC)

EXCUTATION(NEWJOB)

SOLUTION(ADD, Q.N. = 15, VELCONV = 0.1, RESCONV = 0.1)

DATAPRINT(ADD, CONTROL)

PRINTOUT(ADD, NONE, BOUNDARY)

TIMEINTEGRATION(ADD, BACKWARD, NSTEPS = 500, TSTART=0.0E+00,
DT = 0.050000000000000E-04, FIXED, WINDOW)

SURFACETENSION(ADD, SET=1, CONSTANT = 62.3, PRESSURE=981000)
DENSITY(ADD, SET=1, CONSTANT=1.26)

VISCOSITY(ADD, SET=1, CONSTANT=6.29)

ENTITY(ADD, NAME="glycerine", FLUID)

ENTITY(ADD, NAME="outlet", PLOT)

ENTITY(ADD, NAME="inlet", PLOT)

ENTITY(ADD, NAME="free", SURFACE, DEPTH= 10, CONTINUE, SPINES,
STRAIGHT, ANG1= 180.0, ANG2= 5.0)

ENTITY(ADD, NAME="disk-slip",slip)

ICNODE(ADD, UX, CONSTANT=518.68, ENTITY="glycerine")

BCNODE(ADD, COORDINATE, NODES=1)

BCNODE(ADD, COORDINATE, NODES=2)

BCNODE(ADD, COORDINATE, NODES=35)

BCNODE(ADD, COORDINATE, NODES=34)

BCNODE(ADD, UX, ENTITY="inlet", CONSTANT= 518.68)

BCNODE(ADD, UX, ENTITY="outlet", CONSTANT= 518.68)

BCNODE(ADD, UX, NODES=1, CONSTANT= 518.68)

BCNODE(ADD, UX, NODES=34, CONSTANT= 518.68)

BCNODE(ADD, UN, ENTITY="disk-slip", ZERO)

BCNODE(ADD, UT, ENTITY="disk-slip", CONSTANT= -518.68)